A generalized interpolation material point method and anisotropic creep damage model for shallow ice shelves

Alexander Huth

A dissertation

submitted in partial fulfillment of the

requirements for the degree of

Doctor of Philosophy

University of Washington

2020

Reading Committee:

Benjamin Smith, Chair

Ian Joughin

Dale Winebrenner

Ravi Duddu

Program Authorized to Offer Degree:

Earth and Space Sciences

University of Washington

Abstract

A generalized interpolation material point method and anisotropic creep damage model for shallow ice shelves

Alexander Huth

Chair of the Supervisory Committee:

Dr. Benjamin E. Smith

Department of Earth and Space Sciences

Ice mass loss from Antarctica is the main source uncertainty in projections of sea level rise. In Antarctica, the rate at which grounded ice discharges into the ocean and raises sea level is largely controlled by ice shelves, the floating extensions of the ice sheet. Ice shelves provide resistance to upstream grounded ice flow in a process known as buttressing, and reductions in buttressing are responsible for the majority of Antarctic ice mass loss and sea level contribution. Current reductions in buttressing are largely associated with ice shelf thinning from basal melt. However, ice shelf fracture processes such as mechanical weakening and tabular calving also decrease buttressing, and ice shelves become more prone to fracture as they thin. These fracture processes are poorly understood and parameterized in projections of ice sheet evolution. In this

dissertation, I present a new modeling framework for large-scale shallow shelf ice flow and damage that can be used to better project ice sheet evolution and study these ice shelf fracture processes.

In the first of the three studies that comprise this dissertation, I introduce a generalized interpolation material point method (GIMPM) for the shallow shelf approximation (SSA) of ice flow and thickness evolution. The GIMPM is a hybrid Eulerian-Lagrangian framework for large-deformation simulations that is well suited for coupling with the damage model that is employed in the subsequent studies, and can be viewed as a particle variation of the finite element method. The primary advantages of the GIMPM-SSA framework are computationally efficient advection of history or internal state variables without artificial diffusion errors and automated tracking of the ice front and grounding line at sub-element scales. By avoiding artificial diffusion errors, the GIMPM-SSA framework is ideal for capturing sharp features such as rifts in damage studies. I demonstrate the accuracy and stability of the GIMPM-SSA framework using 1-D and 2-D benchmark examples.

In the second study, I develop an anisotropic nonlocal creep damage model for large-scale ice shelf flow and demonstrate that the damage model can simulate the full evolution of fracture from initiation of crevassing to rifting and tabular calving. The damage variable is tensorial and represented in 3-D, and computational efficiency and accuracy is prioritized because the damage model is implemented within the GIMPM-SSA framework. I test the GIMPM-SSA-damage model on an idealized marine ice sheet geometry in comparison to two previously proposed damage models that parameterize crevasse depths, and demonstrate that the creep damage model is best suited for capturing weakening and rifting. Furthermore, I show how using an anisotropic damage variable reproduces typically observed fracture patterns better than

isotropic damage. I then discuss possibilities for incorporating the effects of necking and mass balance on creep damage evolution, which will ultimately allow a more accurate damage response on decadal timescales.

In the final study, I verify and tune the GIMPM-SSA-damage model on a real ice shelf by simulating the final two years of rifting on the Larsen C Ice Shelf that resulted in the tabular calving of iceberg A-68 in 2017. The tuning simulations are initialized from a diagnostic model, which is developed using a data assimilation procedure that includes a novel scheme for inferring initial fields for the basal friction parameter, damage, and an enhancement factor related to fabric orientation. During the tuning simulations, most damage parameters are found to only influence the rate of rift propagation rather than the rift path. However, the rift path is sensitive to the amount of residual strength allowed between rift flanks and the rotation of the nascent iceberg. To better represent the stresses associated with rifting, I also introduce a technique that accounts for the boundary forces on rift flank walls from seawater, contact between flanks, and ice mélange at runtime.

TABLE OF CONTENTS

LIST OF FIGURES

LIST OF TABLES

ACKNOWLEDGEMENTS

First, I want to thank my advisor, Ben Smith, for his guidance over the past six years. When I first entered graduate school, Ben suggested that I investigate the hypothesis that an ice shelf will collapse if its "compressive arch", the point at which flow transitions from uniaxial to biaxial extension, is breached. I found this question difficult to answer with the tools for modeling fracture available at the time, and I subsequently ended up spending nearly my entire PhD developing the damage framework presented in this dissertation (now that the model is working, maybe I can finally complete the compressive arch project…). I am extremely grateful for the freedom that Ben gave me to follow my own research path, and also for getting me involved with working with satellite data on the side, which has helped me find my way to the intersection of data and modeling. The data research also led to some rewarding trips to Goddard, Banff, and the ICESat-2 launch.

I owe much thanks to Ravi Duddu, who effectively served as co-advisor in the second half of my PhD. I certainly would not understand mechanics or modeling to the extent I do now had I not met Ravi at a workshop several years ago. Ravi helped me think about my work from an engineering perspective and helped guide me though unfamiliar literature that often had nothing to do with ice. He made me a better mathematician. Ben, Ravi, and I have forged a collaboration that is lasting past my time in graduate school.

I also want to thank the rest of my committee members: Ian Joughin, Dale Winebrenner, Bonnie Light, Knut Christianson, and Michelle Koutnik. Ian in particular, has always been a role model, and I have learned a great amount from him about science and how to be a scientist. I appreciate all the feedback and encouragement that Dale, Bonnie, Knut, and Michelle gave me.

The last faculty members I want to acknowledge are Ed Waddington and Steve Warren, who taught me all the fundamentals of glaciology.

Finally, I want to thank everyone that kept me sane in grad school. First, I thank my UW friends – Nick, Ben, John, Mike, Tina, Sean, and Maddie – who always distracted me from my work and with whom I made great memories skiing, jamming, and throwing really awful grad student parties. I also thank my "real world" friends, my bandmates – Tom, Steve, Ben, and William – who provided me the expressive outlet I needed, and with whom I made great memories touring around the Northwest rocking out. Of course, I thank my family for their unconditional support through all of my education. Most of all, I thank my fiancé Sarah, for inspiring me and taking care of me, and for her humor and unconditional love.

Chapter 1. Introduction

1.1 Motivation

The primary uncertainty in projections of sea level change are the dynamic contributions (i.e. the contribution related to flow processes) from the Antarctic Ice Sheet. The dynamic response of the ice sheet to climate variations is largely governed by ice shelves, the floating extensions of the ice sheet (*IPCC*, 2014). Ice shelves are typically constrained within embayments and act to buttress, or inhibit, the flow of upstream grounded ice into to the ocean. Nearly all ice mass loss in Antarctica occurs at ice shelves due to roughly equal contributions from basal melting and tabular calving (Depoorter et al., 2013; Rignot et al., 2013; Paolo et al., 2015). The melting and calving of shelf ice does not directly contribute to sea level rise because ice shelves are already floating. However, these processes — as well thermomechanical weakening (e.g. Borstad et al., 2013; Sun et al., 2017), surface hydrofracture (e.g. DeConto & Pollard, 2016), changes in contact with bay walls/pinning points, and the response of upstream grounded ice that feeds the shelf — can decrease ice shelf buttressing. Decreased buttressing allows an increased flux of grounded ice into the ocean, resulting in sea level rise (Dupont & Alley, 2005).

In some cases, ice shelf weakening or collapse may trigger instabilities associated with exceptionally rapid and widespread losses of grounded ice. Projecting the onset and evolution of these instabilities therefore depends in part on how well models can represent the processes associated with ice shelf weakening or collapse. One instability may occur when the grounding line, the location at which a grounded ice sheet transitions to a floating ice shelf, lies on bedrock that deepens towards the interior (retrograde slope). This grounding line configuration can result

in a positive feedback of continued grounding line retreat. In the theoretical case of a 1-D flow-line ice sheet with no buttressing, this retreat continues until the grounding line reaches a prograde slope (e.g. Weertman, 1974; Schoof, 2007). This phenomenon is known as the marine ice sheet instability (MISI). When considering complex, 3-D ice sheet geometries, the extent and rate at which a MISI-like retreat dictates ice sheet evolution depends not only on bed geometry, but on processes such as the buttressing strength of the ice shelf, lateral shear, and isostatic adjustment of the bedrock (*IPCC*, 2019). Pine Island Glacier and Thwaites Glacier in West Antarctica are known to have retreating grounding lines on retrograde bedrock, and these glaciers are responsible for a large percentage of current ice mass loss. Collapse of Thwaites Glacier may already be underway due to MISI processes, and could ultimately lead to complete destabilization of the West Antarctic Ice Sheet (Joughin et al., 2014; Rignot et at., 2014), which would raise global mean sea level by ~3.4 m (Fretwell, et al., 2013). There is geologic evidence that WAIS collapse may have occurred in previous warm periods (Scherer et al., 1998; Dutton et al., 2015).

In addition to MISI, a second potential instability may occur when ice shelves fully collapse, likely due to hydrofracture. In this case, tall ice cliffs may form that are innately unstable so that they repeatedly calve, and the ice sheet retreats. This process, known as marine ice cliff instability (MICI), could cause rapid collapse of the West Antarctic Ice Sheet in several centuries (Pollard et al., 2015; DeConto & Pollard, 2016). The actual existence of MICI, or the extent of its role in the collapse of ice sheets, is controversial. For example, a recent study argues that the longer it takes for an ice shelf to collapse, the taller the ice cliffs must be to initiate MICI, so that the instability is likely mitigated in many cases (Clerc et al., 2019).

A recent report from the Intergovernmental Panel on Climate Change (IPCC) stated that recent contributions to global mean sea level have been dominated by the Greenland Ice Sheet, at ~0.77 mm/yr from 2006-2015 versus ~0.43 mm/yr from Antarctic Ice Sheet over the same time period; however, Antarctic sea level contributions will likely exceed those from Greenland by 2100 (*IPCC*, 2019). The report projected that if greenhouse gas emissions remain high (RCP 8.5), Antarctica will likely contribute ~28 cm to global mean sea level by the end of the century largely due to dynamic effects while Greenland would likely contribute ~20 cm, largely due to mass loss from surface melt. However, the Antarctic projections were noted to be much less certain that the Greenland projections, especially beyond 2050, due to uncertainty related to several dynamic processes that remain poorly understood and challenging to model realistically. The largest uncertainties are associated with ice-ocean interaction related to basal melt, calving and fracture processes, basal sliding, and glacial isostatic adjustment (Pattyn & Morlighem, 2020). Without a better representation of these processes, accurate projection of the timing and extent of future ice shelf loss and instabilities is unlikely, especially on century timescales. Therefore, the IPCC estimate for global sea level rise by 2300 is given with low confidence and spans a large range of 2.3-5.4 m for the high emissions scenario (RCP 8.5).

The overarching motivation for my research is to reduce those uncertainties that affect dynamic response of the Antarctic Ice Sheet forced by climate variability. Specifically, this dissertation primarily focuses on modeling and better understanding large-scale ice shelf fracture processes. The effects of ice shelf fracture have been shown in previous modeling studies to exert a strong influence on the evolution of the Antarctic Ice Sheet, including the initiation and evolution of ice sheet instabilities; however, the fracture effects have only been implemented in a completely ad hoc manner (e.g. Joughin et al., 2014) or with rough parameterizations (e.g.

Pollard et al., 2015; DeConto and Pollard, 2016) because they are poorly understood. For example, a combination of fracture-induced (Borstad et al., 2013) and rheological (Larour et al., 2005) weakening is a commonly observed feature at ice shelf margins, and a modeling study that projected the MISI-type evolution of Thwaites glacier showed that the rate of collapse could be accelerated by decades to centuries depending on the amount of marginal weakening applied (Joughin et al., 2014). However, this weakening was assigned with an ad hoc parameterization. Some damage models were later proposed (e.g. Borstad et al., 2016; Sun et al., 2017) that account for fracture-induced weakening and its feedback on glacial stresses, but these models are heavily parameterized. Furthermore, they do not appear to be capable of properly capturing sharp fracture processes such as the initiation and propagation of rifts (see Chapter 3). In this dissertation, I develop a creep damage mechanics framework for modeling large-scale ice shelf fracture that can capture widespread fracture-induced weakening, as well as rifting and tabular calving. I verify and tune the model by simulating an observed calving event, and I use the model to investigate the processes that affect the path and rate of rift propagation. This damage framework could be used to develop better fracture parameterizations for models of ice sheet response to climate, or the damage framework could even be eventually adapted for direct implementation into such models.

1.2 Research Approach

Implementing damage mechanics at the scale of entire ice shelves presents two major challenges. The first challenge is associated with the highly nonlocal stress regime of ice shelves, where a change in stress in one part of the shelf can affect stresses throughout the shelf (Cuffey & Patterson, 2010). Because damage evolves according to stress or strain, all other major processes

that impact ice shelf stress (e.g. fluctuations in contact with bay walls/pinning points, advection of the ice front, evolution of upstream grounded ice, changes in ice thickness or rheological properties, and grounding line migration) must therefore also be accounted for accurately within the same model, and in a computationally efficient manner. The second major challenge is that ice shelves are associated with extreme deformations. Only specialized numerical methods can model damage within large-deformation flow without degrading the damage field with artificial diffusion errors during advection schemes. Therefore this thesis begins by developing a generalized interpolation material point method (GIMPM) for the shallow shelf approximation (SSA) of ice flow, which addresses both of these major challenges.

Using the GIMPM-SSA framework, I then incorporate a 3-D nonlocal anisotropic creep damage model for glacier ice (Pralong & Funk, 2005), which represents the first implementation of this damage model for large-scale ice flow, and the first application of the damage model in anisotropic form within any ice flow model. Using an idealized marine ice sheet geometry, I demonstrate that the model captures the full evolution of ice shelf fracture from initiation of crevasses to rifting and tabular calving. I also compare the creep damage model to previously proposed damage models that parameterize crevasse depths, and demonstrate the numerical and physical advantages of the creep damage model for capturing rifting. I further verify and tune the model by simulating the 2017 calving of iceberg A-68 on the Larsen C ice shelf, and use the model to investigate the processes that affect the rate and path of rift propagation. The combined GIMPM-SSA-damage framework is a potentially powerful model for determining ice shelf response to climate variations because it can capture a wide range of important physical processes within a single model, including mechanical weakening, calving, thickness evolution, ice front advection, and grounding line migration. Furthermore, the GIMPM-SSA framework is

well suited for incorporating other important processes within future studies, and these processes may be represented in 3-D with minimal additional computational cost. Possible future additions to the modeling framework include the evolution of temperature, density, and fabric anisotropy.

1.3 Organization of the dissertation

This thesis consists of four chapters, including this introduction. Chapters 2 and 3 are scientific papers that will be submitted to the *Journal of Advances in Modeling Earth Systems*. The final chapter is a paper that will be submitted to a glaciology journal in fall 2020. All three papers are co-authored by Benjamin Smith (Applied Physics Laboratory, Polar Science Center, University of Washington, Seattle, WA, USA) and Ravindra Duddu (Department of Civil and Environmental Engineering/Department of Earth and Atmospheric Sciences, Vanderbilt University, Nashville, TN, USA).

Chapter 2 is a manuscript entitled **A generalized interpolation material point method for shallow ice shelves. Part I: shallow shelf approximation and ice thickness evolution**. This paper details the development of the GIMPM-SSA framework as a flow model without the damage component, and demonstrates the numerical accuracy of the framework regarding 1-D and 2-D front advection, evolution of stress and thickness, and avoidance of artificial diffusion errors during advection of history variables. The supplement for this paper can be found in Appendix A.

Chapter 3 is a manuscript entitled **A generalized interpolation material point method for shallow ice shelves. Part II: anisotropic nonlocal damage mechanics and rift propagation**. This paper details the incorporation of the nonlocal anisotropic creep damage model into the GIMPM-SSA framework. The test cases of the model on the idealized marine ice

sheet are presented, as well as similar test cases for the previously proposed damage models that parameterize crevasse depths. Future modifications to account for the impact of necking and mass balance on creep damage are discussed. The supplement for this paper can be found in Appendix B.

Chapter 4 is a manuscript entitled **Application of shallow shelf creep damage to the 2017 calving of iceberg A-68 on Larsen C Ice Shelf**. This paper presents the Larsen C tuning and rift propagation experiments. In addition, the data assimilation scheme to develop the initial state of the Larsen C model is detailed, which involves a dual inversion for the viscosity and friction parameters and provides the initial state of the system for the forward experiments. Notably, this scheme also consists of a procedure for extracting three separate fields comprised within the inferred viscosity parameter: damage, viscosity effects from temperature, and an enhancement factor that parameterizes variations in fabric orientation. Furthermore, a new technique is tested that incorporates at runtime the boundary forces on rift flank walls from seawater, contact between flanks, and ice mélange.

Chapter 2. A generalized interpolation material point method for shallow ice shelves. Part I: shallow shelf approximation and ice thickness evolution

Abstract

We develop a generalized interpolation material point method (GIMPM) for the shallow shelf approximation (SSA) of ice flow. The GIMPM, which can be viewed as a particle version of the finite element method, is used here to solve the shallow shelf approximations of the momentum balance and ice thickness evolution equations. We introduce novel numerical schemes for particle splitting and integration at domain boundaries to accurately simulate the spreading of an ice shelf. The advantages of the proposed GIMPM-SSA framework include efficient advection of history or internal state variables without diffusion, automated tracking of the ice front and grounding line at sub-element scales, and a weak formulation based on well-established conventions of the finite element method with minimal additional computational cost. We demonstrate the numerical accuracy and stability of the GIMPM using 1-D and 2-D benchmark examples. We also compare the accuracy of the GIMPM with the standard material point method (sMPM) and a reweighted form of the sMPM. We find that the grid-crossing error is very severe for SSA simulations with the sMPM, whereas the GIMPM successfully mitigates this error. While the grid-crossing error can be reasonably reduced in the sMPM by implementing a simple material point reweighting scheme, this approach it not as accurate as the GIMPM. Thus, we illustrate that the GIMPM-SSA model is viable for the simulation of ice sheet-shelf evolution and enables boundary tracking and error-free advection of history or state variables, such as ice thickness or damage.

2.1 Introduction

The fate of the entire Antarctic Ice Sheet is largely controlled by ice shelf dynamics. Over 80% of the Antarctic Ice Sheet drains into the ocean through floating ice shelves (Pritchard et al., 2012), where nearly all mass loss of the ice sheet occurs due to roughly equal contributions from basal melting and tabular calving (Depoorter et al., 2013; Rignot et al., 2013; Paolo et al., 2015). However, ice shelves also provide resistance to the flow of upstream grounded ice into the ocean, which primarily arises from contact with the walls of the bays in which they typically reside and localized grounding at pinning points such ice rises and ice rumples. Any loss of this resistance, or buttressing, results in an increased flux of grounded ice flow into the ocean, thereby contributing to sea level rise (Dupont & Alley, 2005).

On decade to century timescales, the magnitude of ice shelf buttressing is controlled by ice front evolution (i.e. fluctuations in contact with bay walls/pinning points), fracture or thermomechanical weakening (e.g. Borstad et al., 2013; Sun et al., 2017), changes in ice thickness such as thinning from ocean-driven basal melt (Pritchard et al., 2012; Cook et al., 2016), and response of the upstream grounded ice that feeds the shelf. Ideally, these four processes should be represented in a fully coupled manner that accounts for the complex feedbacks between them. For example, ice shelf thinning from basal melt has been associated with increased fracture (Shepherd et al., 2003; Liu et al., 2015), and fracture determines the ice front position through tabular calving. Calved icebergs can then alter local ocean properties and circulation within the ice shelf cavity and wherever they drift, which in turn, may affect basal melting rates (e.g. Robinson et al., 2010; Stern et al., 2015, 2016; Cougnon et al., 2017). Further, a more general motivation for developing an integrated representation of these processes stems from the lack of basal friction in ice shelves, which causes a highly nonlocal stress regime where

altering stress in one part of the shelf can affect stresses throughout the shelf (Cuffey & Paterson, 2013). Therefore, it is important that we develop advanced numerical models and methods to enable realistic simulation of these processes controlling large-scale ice shelf evolution, and thus gain a better understanding of Antarctic Ice Sheet dynamics and improve projections of sea level rise.

Current large-scale ice flow models have difficulty in capturing the simultaneous processes of front evolution, fracture, and thinning owing to the differences in the modeling frameworks that are effective at describing each process separately. Because large-scale ice flow is associated with extreme deformations, it is typically modeled within an Eulerian framework, where velocity is calculated as the ice flows through a fixed region in space. Typically, Eulerian models calculate flow velocity on a fixed mesh over time. However, some processes such as ice mass transport or fracture (represented by damage), are not well-suited to the Eulerian approach due to the artificial diffusion or dispersion inherent to Eulerian advection schemes. For example, this artificial or numerical diffusion smears sharp edges and therefore compromises the accuracy of damage advection and evolution. Furthermore, Eulerian approaches require separate schemes to approximate ice front evolution, such as level-set (Bondzio et al., 2016) or volume of fluid methods (Jouvet et al., 2008; Albrecht et al., 2011). In contrast, a Lagrangian approach, where the position of mesh nodes update with flow, avoids numerical diffusion and naturally tracks ice front evolution. However, Lagrangian or updated Lagrangian methods are only well-suited for small deformation ice flow, such as within 2-D flow-band models for the propagation of individual crevasses over short timescales (Duddu et al., 2013; Duddu & Waisman, 2013; Jiménez et al., 2017). Use of Lagrangian methods to model entire ice shelf-sheet systems could

result in mesh degradation or tangling owing to the large deformations. Simple remeshing schemes are not ideal because they also introduce artificial diffusion.

These limitations of traditional Eulerian and Lagrangian schemes may be overcome using material point methods, which are formulated in a hybrid Eulerian-Lagrangian framework that simultaneously allows large deformation flow, error-free advection of history variables, and boundary tracking. The material point method (MPM) was originally introduced by Sulky et al. (1994, 1995) for solid mechanics, as an adaptation of the particle-in-cell (PIC) (Evans et al., 1957) and fluid-implicit-particle (FLIP) (Brackbill et al., 1988) methods. Henceforth, we will refer to this original version as the standard MPM (sMPM). In the sMPM, the material domain is discretized into a set of material points, or particles, that provide a Lagrangian description. Each material point has a mass, volume, position, velocity, stress, and any history variables or other material properties of the constitutive model. A background Eulerian mesh/grid is also defined, which extends beyond the initial domain defined by the material points, and typically remains fixed throughout the simulation. Grid cells containing material points constitute the "active" mesh on which the equations of motion are solved in a similar manner as the finite element method (FEM), but with material points serving as moving integration points. The mesh solution is then used to update material point variables and positions.

Many variants of the sMPM have been formulated that retain the basic procedure, but exhibit higher accuracy. These variants are largely motivated by the need to mitigate the well-known "cell-crossing error" in sMPM. This error arises from mapping between the material point and the background grid using linear shape functions, which have discontinuous gradients between grid cells so that abrupt transfers of stiffness occur as material points cross cell boundaries or become unevenly distributed between neighboring cells. The first sMPM variant to

mitigate this error was the generalized interpolation material point method (GIMPM) developed by Bardenhagen and Kober (2004), which convolves the linear nodal shape functions with characteristic functions associated with each material point to result in continuous gradients between grid cells (see Figure A-1). Other common variants of sMPM that modify the shape functions to have continuous gradients include the convected particle domain interpolation (CPDI) methods (Sadeghirad et al., 2011, 2013) and dual-domain material point (DDMP) methods (Zhang et al., 2011). These variants of the sMPM have found diverse applications for modeling impact, fracture, and granular media behavior; for a more detailed literature review we refer the reader to Dunatunga and Kamrin (2015) and Coombs et al. (2020). Material point methods have also been used to model certain components of the cryosphere, including sea ice dynamics (Sulsky, 2007), snow (Stomakhin, 2013), and avalanches (Gaume et al., 2018).

Here, we develop an implementation of the GIMPM for simulating shallow-shelf ice flow. To our knowledge, this is the first ever implementation of MPMs for shallow ice flow. Our GIMPM formulation solves the momentum and mass balance equations for ice flow and thickness evolution, and enables natural tracking of the ice front and grounding line. In Chapter 3, we incorporate an anisotropic nonlocal creep damage model (Pralong & Funk, 2005; Duddu & Waisman, 2012) for fracture propagation. This chapter solely focuses on the description and verification of the GIMPM in simulating shallow ice flow, ice thickness evolution, and ice-ocean boundary treatment. We solve for ice flow velocities using the Shallow Shelf Approximation, or Shelfy-Stream Approximation (SSA), a 2-D vertically-integrated flow model that is appropriate for large-scale ice shelf and ice stream flow, where horizontal velocities can be considered vertically invariant (MacAyeal, 1989). The SSA constitutes the only equations solved using the background Eulerian mesh/grid, while history variables such as ice thickness and damage are

updated explicitly and efficiently on each material point directly. The primary advantage of our GIMPM formulation is that advection of all variables only involves updating the material point positions, thus our Lagrangian advection scheme is computationally inexpensive and avoids the artificial diffusion errors associated with Eulerian schemes. Furthermore, the positions of the material points allow us to establish and track the ice front and grounding line at sub-grid scales. We implemented our model within the open-source finite element ice flow model Elmer/Ice (Gagliardini et al., 2013), by modifying the Elmer SSA solver to implement GIMPM integration schemes and by introducing several modules for tracking and evolving the set of material points.

In the following sections, we will detail the derivation of our method and quantify its accuracy and stability for 1-D and 2-D ice flow simulations, including front advection. We will illustrate that the GIMPM-SSA formulation is effective for: advecting history or internal state variables without diffusion, maintaining the steady-state grounding lines of marine ice sheets, and tracking ice front evolution on century timescales. To ensure numerical accuracy, we formulate novel schemes for enforcing the conditions at the ice front and outflow boundaries, as well as for determining ice thickness at material points due to particle splitting. This chapter is organized as follows: in Section 2.2 we review the SSA equations and their numerical discretization using the FEM and the GIMPM; in Section 2.3 we provide the details of our numerical implementation related to grid and particle variable updates; in Section 2.4 we present schemes for boundary treatment and error control; in Section 2.5 we provide examples that test the accuracy and numerical performance of the GIMPM-SSA formulation; in Section 2.6 we provide a brief discussion on the pros and cons of the GIMPM, and finally, in Section 2.7 we make a few concluding remarks.

2.2 Governing Equations

In this section, we will briefly describe the governing equations of ice flow based on the Shallow Shelf Approximation (SSA), followed by the numerical discretization using the finite element and generalized material point methods. We will use indicial notation for vectors and tensors to describe the strong and weak forms of the governing equations and use matrix notation to present the corresponding discretized linear system. We will use Einstein's summation convention only for spatial indices, where repeated indices imply summation. For brevity, we occasionally avoid indicial notation, and use bold face letters to denote vectors, tensors and matrices.

2.2.1 *Shallow Shelf Approximation*

Ice shelves and ice streams can be modeled under the assumption of plug flow, where horizontal velocities and strain rates are constant over depth. Consequently, the incompressible Stokes equations are modified to exclude vertical shear and vertically integrated to derive the SSA that describes the horizontal force or momentum balance as

$$\frac{\partial T_{ij}}{\partial x_j} + (\tau_{\mathrm{b}})_i = \rho g H \frac{\partial s}{\partial x_i}, \tag{2.1}$$

where spatial indices $i, j \in \{1,2\}$ correspond to the horizontal plane, $\boldsymbol{x} = x_i \hat{e}_i$ denotes the in-plane spatial coordinates, $\hat{e}_i$ are the basis vectors for the Cartesian coordinate system, ρ is the ice density, g is the acceleration due to gravity, H is the ice thickness, s is the top surface elevation, $\bar{\eta}$ is the depth-averaged effective viscosity, and τ_{b} is the basal traction described by a friction law. For simplicity, here we assume the friction law as

$$(\tau_{\mathrm{b}})_i = \hat{\beta} v_i, \tag{2.2}$$

where $\hat{\beta}$ is a friction parameter and v_i are the horizontal velocities for which the SSA is solved. Note that the above equation can used to specify several friction laws currently available in Elmer/Ice (Gagliardini et al., 2013) by defining $\hat{\beta}$ to be dependent on velocity, and in some cases, pressure. In (2.1), the two-dimensional vertically-integrated stress tensor **T** is defined as (Bueler and Brown, 2009; Morland, 1987):

$$\mathbf{T} = 2\bar{\eta}H\begin{bmatrix} 2\dfrac{\partial v_1}{\partial x_1}+\dfrac{\partial v_2}{\partial x_2} & \dfrac{1}{2}\left(\dfrac{\partial v_1}{\partial x_2}+\dfrac{\partial v_2}{\partial x_1}\right) \\ \dfrac{1}{2}\left(\dfrac{\partial v_1}{\partial x_2}+\dfrac{\partial v_2}{\partial x_1}\right) & \dfrac{\partial v_1}{\partial x_1}+2\dfrac{\partial v_2}{\partial x_2} \end{bmatrix}, \tag{2.3}$$

which may alternatively be expressed in terms of strain rate $\dot{\varepsilon}_{ij} = \frac{1}{2}\left(\frac{\partial v_i}{\partial x_j}+\frac{\partial v_j}{\partial x_i}\right)$ as

$$\mathbf{T} = 2\bar{\eta}H\begin{bmatrix} 2\dot{\varepsilon}_{11}+\dot{\varepsilon}_{22} & \dot{\varepsilon}_{12} \\ \dot{\varepsilon}_{21} & \dot{\varepsilon}_{11}+2\dot{\varepsilon}_{22} \end{bmatrix}. \tag{2.4}$$

The constitutive relation for ice flow relates deviatoric stress, σ_{ij}^{D}, to strain rate as

$$\sigma_{ij}^{D} = 2\eta\dot{\varepsilon}_{ij}\,, \tag{2.5}$$

where the effective viscosity, η, follows the Norton-Hoff flow law (Glen, 1955; Nye, 1957):

$$\eta = \frac{1}{2}\,B\dot{\varepsilon}_{\mathrm{e}}^{(1-n)/n}\,. \tag{2.6}$$

In the above equation, n is the flow law exponent, $\dot{\varepsilon}_{\mathrm{e}}$ is the scalar second invariant or effective strain rate $\dot{\varepsilon}_{\mathrm{e}} = \sqrt{\dot{\varepsilon}_{ij}\dot{\varepsilon}_{ji}\,/\,2}$, and B is a flow rate factor dependent on temperature and ice fabric. The depth-averaged effective viscosity used in the SSA takes the same form as (2.6), but uses only in-plane strain components to determine $\dot{\varepsilon}_{\mathrm{e}}$ and a depth-averaged rate factor, $\bar{B} = \frac{1}{H}\int_b^s B\,dz$, where b is the vertical coordinate of the ice basal surface. We take z as positive in the upward direction, where $z = 0$ corresponds to sea level.

A boundary condition at the ice front is set according to the seawater pressure at the ice terminus opposing ice flow

$$\sigma_{ij}\hat{n}_j = \begin{cases} \rho_{\mathrm{w}} g z\, \hat{n}_i & \text{for } z < 0 \\ 0 & \text{for } z \geq 0 \end{cases}, \tag{2.7}$$

where $\sigma_{ij} = \sigma_{ij}^{D} - p\delta_{ij}$ is the Cauchy stress, p is the hydrostatic pressure, δ_{ij} is the Kronecker's delta, and $\hat{\boldsymbol{n}}$ is the unit (outward) normal to the ice front. Equation (2.7) is depth-integrated for implementation into the SSA as (Morland and Zainuddin, 1987):

$$\int_b^s \sigma_{ij}\hat{n}_j \, dz = -\frac{1}{2}\rho_{\mathrm{w}} g b^2 \hat{n}_i \, . \tag{2.8}$$

Appropriate Dirichlet conditions for velocity are set at all other boundaries.

2.2.2 *Weak form and discretization using the FEM*

The procedure for deriving the weak form of the SSA and discretization using the sMPM or the GIMPM is similar to that using the FEM, so we briefly review the procedure using the FEM first for clarity. Full details of this procedure can be found in the literature (e.g. Weis, 2001; Greve and Blatter, 2009; Lipscomb et al., 2019). The weak form of the SSA is derived using the Bubnov-Galerkin method of weighted residuals by multiplying (2.1) by an arbitrary smooth test function $\boldsymbol{w}(\boldsymbol{x})$ and integrating over the domain. After applying the divergence theorem and introducing the boundary conditions, we obtain:

$$\begin{aligned} &\int_\Omega T_{ij}\frac{\partial w_i}{\partial x_j} d\Omega + \int_\Omega w_i \rho g H \frac{\partial s}{\partial x_i} d\Omega - \int_\Omega w_i (\tau_{\mathrm{b}})_i d\Omega \\ &- \int_{\Gamma_k} w_i T_{ij}\hat{n}_j d\Gamma - \int_{\Gamma_{\mathrm{cf}}} \frac{1}{2} w_i (\rho g H^2 - \rho_w g b^2)\hat{n}_i d\Gamma = 0 \, , \end{aligned} \tag{2.9}$$

where Ω and Γ_{cf} represent the area of the ice domain and calving front boundary, respectively, and Γ_k represents the boundaries where Dirichlet conditions for velocity are applied.

All variables in (2.9), including the test function $\boldsymbol{w}$, are represented continuously on the mesh/grid using nodal shape functions. For example, velocity at a spatial location $\boldsymbol{x}$ and time t is defined as

$$\boldsymbol{v}(\boldsymbol{x}, t) = \sum_{I=1}^{N_n} \boldsymbol{v}_I(t)\phi_I(\boldsymbol{x}) \,, \tag{2.10}$$

where the nodes of the mesh are $\boldsymbol{x}_I, I = 1, \dots, N_n$, $\phi_I(\boldsymbol{x})$ is the nodal shape function associated with node I, and N_n is the number of nodes of the chosen finite element (here we use 4-noded quadrilateral elements, so $N_n = 4$). Substituting the continuous representations for $\boldsymbol{v}$ and $\boldsymbol{w}$ from (2.10) into (2.9), and noting that the test functions are arbitrary, a linear system can be assembled and solved for horizontal velocities $\boldsymbol{v}$. The element tangent stiffness matrix $\mathbf{K}$ and residual force vector $\boldsymbol{f}$ can be split into components and expressed as follows:

$$\begin{bmatrix} \mathbf{K}_{11} & \mathbf{K}_{12} \\ \mathbf{K}_{21} & \mathbf{K}_{22} \end{bmatrix} \begin{bmatrix} \boldsymbol{v}_1 \\ \boldsymbol{v}_2 \end{bmatrix} = \begin{bmatrix} \boldsymbol{f}_1 \\ \boldsymbol{f}_2 \end{bmatrix}, \tag{2.11}$$

where $\boldsymbol{v}_1$ and $\boldsymbol{v}_2$ are the vectors of nodal velocity components, the vectors $\boldsymbol{f}_1$ and $\boldsymbol{f}_2$ contain the gravitational forcing, and the element submatrices of the tangent matrix are given by

$$
\begin{aligned}
\mathrm{K}_{11\mathrm{IJ}} &:= \int_{\Omega^E} 2\overline{\eta}H\left(2\frac{\partial\phi_I(\boldsymbol{x})}{\partial x_1}\frac{\partial\phi_J(\boldsymbol{x})}{\partial x_1}+\frac{1}{2}\frac{\partial\phi_I(\boldsymbol{x})}{\partial x_2}\frac{\partial\phi_J(\boldsymbol{x})}{\partial x_2}\right)\mathrm{d}\Omega \\
&\quad+\int_{\Omega^E}\hat{\beta}\phi_I(\boldsymbol{x})\phi_J(\boldsymbol{x})\mathrm{d}\Omega\,, \\
\mathrm{K}_{22\mathrm{IJ}} &:= \int_{\Omega^E} 2\overline{\eta}H\left(2\frac{\partial\phi_I(\boldsymbol{x})}{\partial x_2}\frac{\partial\phi_J(\boldsymbol{x})}{\partial x_2}+\frac{1}{2}\frac{\partial\phi_I(\boldsymbol{x})}{\partial x_1}\frac{\partial\phi_J(\boldsymbol{x})}{\partial x_1}\right)\mathrm{d}\Omega \\
&\quad+\int_{\Omega^E}\hat{\beta}\phi_I(\boldsymbol{x})\phi_J(\boldsymbol{x})\mathrm{d}\Omega\,, \\
\mathrm{K}_{12\mathrm{IJ}} &:= \int_{\Omega^E} 2\overline{\eta}H\left(\frac{\partial\phi_I(\boldsymbol{x})}{\partial x_2}\frac{\partial\phi_J(\boldsymbol{x})}{\partial x_1}+\frac{1}{2}\frac{\partial\phi_I(\boldsymbol{x})}{\partial x_1}\frac{\partial\phi_J(\boldsymbol{x})}{\partial x_2}\right)\mathrm{d}\Omega\,, \\
\mathrm{K}_{21\mathrm{IJ}} &:= \int_{\Omega^E} 2\overline{\eta}H\left(\frac{\partial\phi_I(\boldsymbol{x})}{\partial x_1}\frac{\partial\phi_J(\boldsymbol{x})}{\partial x_2}+\frac{1}{2}\frac{\partial\phi_I(\boldsymbol{x})}{\partial x_2}\frac{\partial\phi_J(\boldsymbol{x})}{\partial x_1}\right)\mathrm{d}\Omega\,,
\end{aligned}
\tag{2.12}
$$

where I and J denote the nodal indices of the element and Ω^E is the domain of the element, as indicated by the superscript, 'E'. The right-hand size of (2.11) is given as

$$
\begin{aligned}
f_{1\mathrm{I}} &:= \int_{\Omega^E}\phi_I(\boldsymbol{x})\rho g H\frac{\partial s}{\partial x_1}d\Omega\,, \\
f_{2\mathrm{I}} &:= \int_{\Omega^E}\phi_I(\boldsymbol{x})\rho g H\frac{\partial s}{\partial x_2}d\Omega\,.
\end{aligned}
\tag{2.13}
$$

At boundary elements for the calving front,

$$
f_{iI} = \int_{\Gamma_{cf}^E}\frac{1}{2}\phi_I(\boldsymbol{x})(\rho g H^2-\rho_w g b^2)\hat{n}_i d\Gamma = 0\,. \tag{2.14}
$$

Following standard finite element procedure, the integrals in (2.12)-(2.14) are evaluated using Gaussian quadrature. Variables H, ρ, b, B, and $\nabla\boldsymbol{v}$ must be mapped to the Gauss points from the nodes, where B and $\nabla\boldsymbol{v}$ are used to calculate the depth-averaged effective viscosity $\overline{\eta}$.

2.2.3 *Weak form and discretization using the GIMPM*

The original formulation of the GIMPM (Bardenhagen and Kober, 2004) was derived using the Petrov-Galerkin method, wherein the test function $\boldsymbol{w}$ and the trial function $\boldsymbol{v}$ belong to different function spaces. In the GIMPM, each material point or particle is assigned with a particle characteristic function, χ_p, that must satisfy partition of unity in the reference or undeformed configuration

$$\sum_p \chi_p(\mathbf{x}, t = 0) = 1 \ \forall \ \mathbf{x}\,, \tag{2.15}$$

Note that partition of unity is also a requirement for the element shape functions. We choose χ_P to be the commonly used 'hat' function with value one within the material point domain Ω_p and zero outside as

$$\chi_p(\mathbf{x}) = \begin{cases} 1, & \text{if } \mathbf{x} \in \Omega_p\,, \\ 0, & \text{otherwise.} \end{cases} \tag{2.16}$$

Note that if $\chi_p(\boldsymbol{x})$ is chosen as a Dirac delta function, then the sMPM is retrieved. We assign a rectangular domain to each material point over which χ_p is defined, which we will refer to as the GIMPM domain of a material point. To satisfy (2.15) and (2.16), the initial material domain must be discretized into material points so that no gaps or overlapping with neighboring GIMPM domains occurs. The GIMPM requires using a regular background grid of rectangular elements. We perform the initial discretization by evenly subdividing the domain Ω into GIMPM domains Ω_p by introducing a specified number of material points for each active background grid cell. In this formulation, we will update the lengths of the GIMPM domains due to deformation (see Section 2.3), with the goal of maintaining partition of unity over time precisely, to the extent possible. The area associated with a material point, A_p, is then defined as

$$A_p = \int_{\Omega_p} \chi_p(\boldsymbol{x}) d\Omega\,, \tag{2.17}$$

where Ω_p is the support area of the particle characteristic function and Ω is the area of the overall ice domain. Most literature on material point methods generalizes the formulation to 3-D by using volume (V_p) rather than area (A_p), but we use A_p here because the SSA is inherently 2-D.

The values of material point variables may be initialized by integrating properties of the continuum body against the particle characteristic functions. For example, the initial value of material point property, h_p^0, may be expressed as an area-averaged form of the initial continuum field $h^0(x)$ as

$$h_p^0 = \frac{1}{A_p^0} \int_{\Omega^0} h^0(x) \chi_p(\boldsymbol{x}) d\Omega^0, \tag{2.18}$$

where superscript '0' indicates the initial time step. The validity of Equation (2.18) is a consequence of the partition of unity. Consistently, at any future time step m, the particle characteristic functions may be used as a basis to represent the material property throughout the computational domain

$$h^m(\boldsymbol{x}) = \sum_{p=1}^{N_p} h_p^m \chi_p(\boldsymbol{x}), \tag{2.19}$$

where N_p is the number of material points in the domain. We use (2.19) to formulate continuous representations of vertically-integrated stress (T_{ij}), gravitational driving force ($\rho g H \frac{\partial s}{\partial x_i}$), and basal traction $(\tau_b)_i$, which we substitute into (2.9) so that the integrals over the area of the entire ice domain become sums of integrals over material points. Further substituting in the C^0 continuous representations for $\boldsymbol{w}$ using (2.10), and utilizing that the test functions are arbitrary, we obtain the weak form as

$$\sum_{p=1}^{N_p}\left(T_{ij}\right)_p\frac{\partial S_{Ip}}{\partial x_j}A_p+\sum_{p=1}^{N_p}S_{Ip}\rho_p g H_p\left(\frac{\partial s}{\partial x_i}\right)_p A_p-\sum_{p=1}^{N_p}S_{Ip}[(\tau_b)_i]_p A_p$$
$$-\int_{\Gamma_k}\phi_I T_{ij}\hat{n}_j d\Gamma-\int_{\Gamma_{\mathrm{cf}}}\frac{1}{2}\phi_I(\rho g H^2-\rho_w g b^2)\hat{n}_j d\Gamma=0\,, \tag{2.20}$$

where S_{Ip} are the GIMPM weighting functions corresponding to node I (of the fixed background Eulerian mesh) evaluated at a material point location as

$$S_{Ip}=S_I(\boldsymbol{x}_p)=\frac{1}{A_p}\int_{\Omega_p}\chi_p(\boldsymbol{x})\phi_I(\boldsymbol{x})\,d\Omega\,, \tag{2.21}$$

and with the gradient defined as

$$\frac{\partial S_{Ip}}{\partial x_i}=\frac{1}{A_p}\int_{\Omega_p}\chi_p(\boldsymbol{x})\frac{\partial\phi_I(\boldsymbol{x})}{\partial x_i}d\Omega\,. \tag{2.22}$$

We take the nodal shape functions ϕ_I to be element-wise linear Lagrange interpolants. These shape functions at the two nodes of the linear element can be defined as

$$\phi_1=\phi_1(\boldsymbol{x})=\frac{1-\xi}{2},$$
$$\phi_2=\phi_2(\boldsymbol{x})=\frac{1+\xi}{2}, \tag{2.23}$$

where ξ is the local (or isoparametric) coordinate (between -1 and $+1$) of any material or integration point within the parent element. For illustration, we plot the both the linear and GIMPM shape functions in 1-D in Figure A-1. The GIMPM shape function exceeds the boundaries of a single element and is C^1 continuous by smoothing the discontinuous gradient observed in the linear shape functions, which mitigates cell-crossing error. Material points influence all elements that their GIMPM domains overlap. Note that in practice, we evaluate the convolutions in (2.21) and (2.22) as the overlap of χ_p and the linear shape functions within each element rather than for each node individually, which allows us to assemble stiffness matrices is

a similar manner to the FEM (see, e.g., Charlton et al., 2017). Additionally, we note that replacing the linear shape functions with higher order interpolants would be problematic as the latter are not positive throughout the element. Further substituting into (2.20) the C^0 continuous representations for $\boldsymbol{v}$ using (2.10) yields element sub-matrices that are computed by summing over material points:

$$
\begin{aligned}
\mathrm{K}_{11IJ} &:= \sum_{p=1}^{n_p} A_p\, 2\bar{\eta}_p H_p \left(2\frac{\partial \phi_{Ip}}{\partial x_1}\frac{\partial S_{Jp}}{\partial x_1} + \frac{1}{2}\frac{\partial \phi_{Ip}}{\partial x_2}\frac{\partial S_{Jp}}{\partial x_2} \right) + \sum_{p=1}^{n_p} A_p \hat{\beta}_p \phi_{Ip} S_{Jp}\,, \\
\mathrm{K}_{22IJ} &:= \sum_{p=1}^{n_p} A_p\, 2\bar{\eta}_p H_p \left(2\frac{\partial \phi_{Ip}}{\partial x_2}\frac{\partial S_{Jp}}{\partial x_2} + \frac{1}{2}\frac{\partial \phi_{Ip}}{\partial x_1}\frac{\partial S_{Jp}}{\partial x_1} \right) + \sum_{p=1}^{n_p} A_p \hat{\beta}_p \phi_{Ip} S_{Jp}\,, \\
\mathrm{K}_{12IJ} &:= \sum_{p=1}^{n_p} A_p\, 2\bar{\eta}_p H_p \left(\frac{\partial \phi_{Ip}}{\partial x_2}\frac{\partial S_{Jp}}{\partial x_1} + \frac{1}{2}\frac{\partial \phi_{Ip}}{\partial x_1}\frac{\partial S_{Jp}}{\partial x_2} \right), \\
\mathrm{K}_{21IJ} &:= \sum_{p=1}^{n_p} A_p\, 2\bar{\eta}_p H_p \left(\frac{\partial \phi_{Ip}}{\partial x_1}\frac{\partial S_{Jp}}{\partial x_2} + \frac{1}{2}\frac{\partial \phi_{Ip}}{\partial x_2}\frac{\partial S_{Jp}}{\partial x_1} \right),
\end{aligned}
\tag{2.24}
$$

where n_p is the number of material points in the element and we use the same shorthand for the linear shape functions evaluated at a material point location, $\phi_{Ip}=\phi_I(\boldsymbol{x}_p)$, as defined for the GIMPM functions in (2.21). Similarly, the components of the body force vector are computed as

$$
\begin{aligned}
\boldsymbol{f}_1 &:= \sum_{p=1}^{n_p} S_{Ip} \rho_p g H_p \left(\frac{\partial s}{\partial x_1} \right)_p A_p\,, \\
\boldsymbol{f}_2 &:= \sum_{p=1}^{n_p} S_{Ip} \rho_p g H_p \left(\frac{\partial s}{\partial x_2} \right)_p A_p\,.
\end{aligned}
\tag{2.25}
$$

Comparing Equations (2.24) and (2.25) with (2.12) and (2.13),we can notice the subtle differences between the GIMPM and the standard FEM. We address the numerical treatment of the ice front boundary for GIMPM/sMPM in Section 2.4.1.

By replacing S_{Jp} and $\frac{\partial S_{Jp}}{\partial x_i}$ with ϕ_{Jp} and $\frac{\partial \phi_{Jp}}{\partial x_i}$, respectively, in (2.24) – (2.25) we can obtain the sMPM. However, errors in the sMPM can accumulate if the sum of material point area (weights) within an element significantly varies from the element area or if the distribution of material points within the element becomes irregular. In Section 2.5, we show how increasing the number of material points can mitigate this error to a certain extent, but ultimately, an alternative material point weighting is required to more evenly distribute material point weights between elements and maintain accuracy (Gonzalez Acosta et al., 2017). The new weight, W_p, is a function of both the element area, A_{E}, and material point areas, A_p, as given by

$$W_p = \frac{A_{\mathrm{E}}}{\sum_{p=1}^{n_p} A_p}. \tag{2.26}$$

Thus, in the reweighted sMPM, W_p replaces A_p as the integration weights in (2.24) and (2.25). This reweighting can also be used with the GIMPM, where A_p becomes the area of overlap between a GIMPM domain and the element. However, reweighted GIMPM is mostly unnecessary because material point weight is already smoothly distributed between neighboring elements unless severe overlaps or gaps develop between neighboring GIMPM domains. We largely avoid these errors in our simulation studies, and therefore do not apply the reweighting to our GIMPM simulations here.

2.3 Numerical Implementation

At time $t = 0$, the ice domain is discretized into a specified number of material points per grid cell as described in Section 2.2. The unknown variables, namely ice flow velocity and ice thickness, are defined directly on the material points; whereas, the external parameters such as bedrock elevation, the basal friction parameter, and accumulation/ablation rates are defined on the background fixed mesh. For simplicity, each simulation presented here uses a constant flow rate factor B and density ρ for all material points. However, these quantities can be treated as spatially-varying and history-dependent.

In this section, we detail the numerical procedure for a typical computational cycle, according to the simplified representation given in Figure 2-1. The cycle begins with a series of parameter mappings between the material points and the grid (Figure 2-1a and 2-1b), which are needed in preparation for solving the SSA. The mappings are used to initialize the SSA grid velocity and to determine all parameters at the material point level needed to compute (2.24) and (2.25). The SSA is solved using an iterative routine (Figure 2-1c), where material point viscosity is updated alongside grid velocity until convergence. Subsequently, the grid solution is used to update material point positions, velocities, and geometric parameters (Figure 2-1d). Finally, material point history variables are updated (Figure 2-1e), which only includes ice thickness in this study. To improve readability, we will use matrix notation for vectors and tensors to avoid showing spatial indices and show only node and particles indices to explain the mapping between nodes and particles.

2.3.1 *SSA Initialization: Grid parameters*

To allow a solution of the SSA, the velocity field and thickness are initialized on the grid by mapping from the material points (Figure 2-1a), where the thickness on the grid is subsequently converted to surface elevation. The gradients of surface elevation and velocity are mapped to material points for the SSA matrix assembly. The initialized grid velocity is further required as part of the update routine for material point velocity (Section 2.3.4). The velocity mapping from particles to nodes is performed using a formula that enforces momentum conservation:

$$\boldsymbol{v}_I = \frac{\sum_p^{N_p} m_p \boldsymbol{v}_p S_{Ip}}{\sum_p^{N_p} m_p S_{Ip}}, \tag{2.27}$$

where m_p is the material point mass

$$m_p = \rho_p H_p A_p \, . \tag{2.28}$$

Ice thickness is mapped to the grid from material points as

$$H_I = \frac{\sum_p^{N_p} H_p S_{Ip} A_p}{\sum_p^{N_p} S_{Ip} \, A_p}, \tag{2.29}$$

where the denominator is necessary to normalize the interpolation. After each mapping, nodal values of velocity or thickness at Dirichlet boundaries are overwritten with the values specified by the essential boundary condition. Nodal surface elevations are calculated from the nodal ice thicknesses as

$$s_I = b_I + H_I \, , \tag{2.30}$$

where the nodal elevation of the ice base, b_I, is computed as the maximum value of the bedrock elevation (z_{bed}) or the ice base elevation according to hydrostatic equilibrium as

$$b_I = \max\left\{(z_{\text{bed}})_I, z_{\text{sea}} - H_I\left(\frac{\rho}{\rho_{\text{w}}}\right)\right\}, \tag{2.31}$$

and $z_{\text{sea}} = 0$ is the sea level.

2.3.2 *SSA Initialization: Material point parameters*

The second half of the SSA initialization procedure is focused on updating material point variables (Figure 2-1b). Surface height and velocity gradients are determined at any material point p by mapping from the nodes. The friction parameter ($\hat{\beta}_p$), bedrock elevation (z_{bed_p}), and rate factor (B_p) must also be defined at the material point level, which may require mapping from the nodes as well. Any scalar grid property, h_I, may be interpolated to the material points as

$$h_p = \sum_{I}^{N_n} h_I S_{Ip} \, . \tag{2.32}$$

Similarly, for gradients, the mapping is

$$\nabla h_p = \sum_{I}^{N_n} h_I \nabla S_{Ip} \, . \tag{2.33}$$

Lastly, material points are marked as grounded or floating. Defining grounding status at material points (or at Gauss points in the FEM) rather than at nodes during the SSA solution has been shown to provide a more accurate estimate of grounding line dynamics during the SSA solution (Seroussi et al., 2014). However, to be consistent with Elmer/Ice conventions, we also define grounding status at the nodal level as part of the procedure to define the sub-element scale grounding line. If node I has $b_I = (z_{\text{bed}})_I$, it is marked as grounded; otherwise, it is floating. If a material point belongs to an element whose surrounding elements have a mix of grounded and floating nodes, then that it is clear that material point is near the grounding line, and its

grounding status is determined using the same procedure used for the nodes. Otherwise, it inherits the grounding status of its surrounding nodes.

2.3.3 *SSA Solution*

The SSA is solved implicitly using an "iteration on viscosity" scheme where we update material point viscosity, $\bar{\eta}_p$, each iteration until convergence (MacAyeal, 1989) (Figure 2-1c). This is done by mapping the gradients of nodal velocity solution from the previous iteration to material points using (2.33), which are converted to strain-rates to calculate $\bar{\eta}_p$ using (2.6). We achieve quick convergence of the SSA solution using the Biconjugate Gradient Stabilized (BiCGSTAB) method, Incomplete LU preconditioning, and a combination of Picard and Newton iterations.

2.3.4 *Material Point Updates*

Upon completion of the SSA, grid velocities are used to update material point velocities, position, and geometric properties (Figure 2-1d).

Velocities and position: To update velocity and position, material point methods typically adopt the approach of the FLuid Implicit Particle (FLIP) method. For velocity, this update is given as

$$\boldsymbol{v}_p^{m+1} = \boldsymbol{v}_p^m + \Delta t \sum_I^{N_n} \boldsymbol{a}_I^m S_{Ip} = \boldsymbol{v}_p^m + \sum_I^{N_n} (\boldsymbol{v}_I^{m+1} - \boldsymbol{v}_I^m) S_{Ip}\,, \tag{2.34}$$

where a_I^m is the acceleration at time step m at node I, and $\boldsymbol{v}_I^m$ is the nodal velocity previously interpolated to the grid from the material points before the SSA solution in Equation (2.27). This material point position update is

$$\boldsymbol{x}_p^{m+1} = \boldsymbol{x}_p^m + \Delta t \sum_I^{N_n} \boldsymbol{v}_I^{m+1} S_{Ip} \,. \tag{2.35}$$

In practice, the FLIP update scheme can introduce noise that results from the mismatch between the number of material points and grid nodes, so our code also includes the update scheme XPIC(k), an algorithm that can remove FLIP noise using a set of k additional projections (Hammerquist and Nairn, 2017). Lower orders of k may introduce undesired damping, while higher orders of k are computationally expensive. Note that the additional projections required for XPIC(k) can accumulate a small amount of error in conjunction with our boundary treatment at the ice front (Section 2.4.1), but this error can be avoided by always using FLIP updates within k elements of the ice front. While the simulations in this chapter are relatively insensitive to the update scheme chosen, Nairn et al. (2017) demonstrated that XPIC(5) yields sharp and stable crack propagation in damage simulations.

Geometric properties: All updates to material point geometric properties, which include area and the lengths defining the GIMPM domain, depend on the deformation gradient, a fundamental kinematic quantity that characterizes the deformation at a material point based on its current (deformed) and reference (undeformed) spatial coordinates. The material point deformation gradients ($\mathbf{F}_\mathrm{p}$) are tracked over time, and are updated as

$$\boldsymbol{F}_p{}^{m+1} = \left(\boldsymbol{I} + \Delta t \nabla \boldsymbol{v}_p^{m+1}\right) \boldsymbol{F}_p{}^{m} \,. \tag{2.36}$$

where $\boldsymbol{I}$ is the second-order identity tensor. In the sMPM, the determinant of $\boldsymbol{F}_p$ is used to update the material point area as

$$A_p{}^{m+1} = \det(\boldsymbol{F}_p{}^{m+1}) A_p^0 \,. \tag{2.37}$$

In the GIMPM, material point area is calculated as the product of the lengths defining the rectangular GIMPM domain.

Our implementation currently includes two schemes to update GIMPM domain lengths. The lengths should be updated carefully in order to minimize overlap or separation of GIMPM domains over time, and thus maintain partition of unity as precisely as possible throughout the domain. The first scheme updates the lengths of a GIMPM domain such that the resulting rectangular domain approximates the quadrilateral domain that would be obtained if the position of each corner of the GIMPM domain was updated individually (Coombs et al., 2020). In practice, this "corner-tracking" update scheme may be simplified to tracking the midpoints $\hat{\boldsymbol{x}}_p$ of the GIMPM domain edges as

$$\hat{\boldsymbol{x}}_p = \hat{\boldsymbol{x}}_p^m + \Delta t \sum_I \boldsymbol{v}_I^{m+1} \phi_I(\hat{\boldsymbol{x}}_p^m) \,. \tag{2.38}$$

The GIMPM domain lengths can be obtained using the maximum and minimum extents of $\hat{\boldsymbol{x}}_p$ as

$$\left(l_p^{m+1}\right)_i = \frac{1}{2}\left[\max\left(\hat{\boldsymbol{x}}_p\right)_i - \min\left(\hat{\boldsymbol{x}}_p\right)_i\right], \tag{2.39}$$

followed by a correction that guarantees proper volume (area in 2-D) as

$$\left(l_p^{m+1}\right)_i = \left(l_p^{m+1}\right)_i \left[\frac{\det(F_{kl}^{m+1}) \Pi_{j=1}^{n_D} \left(l_p^0\right)_j}{\Pi_{j=1}^{n_D} \left(l_p^{m+1}\right)_j}\right]^{1/n_D} . \tag{2.40}$$

where n_D is the dimension of the problem ($n_D = 2$ in our case). More detailed derivations of the above scheme can be found in Coombs and others (2020). This corner-tracking scheme performs well in minimizing overlap or separation of GIMPM domains over time in any flow regime, but cannot be used at outflow boundaries where a GIMPM domain may only partially overlap the

active background grid, assuming velocities beyond the active grid are unknown (see Section 2.4.1). For these material points, we instead use the second update scheme, given by

$$\left(l_p^{m+1}\right)_i = \left(l_p^0\right)_i {U_{ii}}^{m+1} \text{ (no implied sum on i)}, \tag{2.41}$$

where $\left(l_p^0\right)_i$ are the original domain lengths and $U_{ij} = \sqrt{{F_{ki}}^T F_{kj}}$ is the symmetric material stretch tensor, so that the deformation gradient rotated into the original Cartesian reference frame (Charlton et al., 2017). Although the "stretch-tensor" update scheme can be used instead of the "corner-tracking" scheme in the entire domain, we caution that it is less capable of minimizing overlap or separation of GIMPM domains under large shearing deformation. Because the "stretch-tensor" scheme is sufficiently accurate under stretching and rotation and is computationally more efficient than the "corner-tracking" scheme, the former scheme is suitable for simulations without large shearing deformations. Here, we only use the stretch-tensor scheme for the 1-D flow-band simulations, noting that the corner-tracking scheme gives identical results. In all the 2-D simulations, we employ the corner-tracking scheme.

2.3.5 *History Variable Updates*

The computational cycle finishes by updating the history variables on the material points (Figure 2-1e). Here, we only consider ice thickness (H_p), which is updated explicitly according to the Lagrangian description of surface mass conservation for a column of ice at time step m + 1 as

$$H_p^{m+1} = H_p^m + (\dot{b}_p^m - \nabla \cdot \boldsymbol{v}_p^m H_p^m)\Delta t\,, \tag{2.42}$$

where $\dot{b}_p^m$ (m a^{-1}) is the sum of the basal and surface accumulation rates. We add damage as a history variable in Chapter 3.

2.4 Boundary treatment and splitting

Boundary conditions in MPMs may be applied at the edges of the active computational grid as in the FEM. However, special treatment is required at inflow boundaries to properly introduce new material points to the domain, and at outflow boundaries where material points must be eliminated or GIMPM domains may partially overlap the boundary. Further treatment is also needed at the moving ice front boundary to avoid integration errors, as this boundary may not align with element edges. We detail our boundary treatment in this section. In addition, we detail our material point splitting scheme, which mitigates additional integration errors that may arise under tension, where the resolution of material points per grid cell decreases over time as the area of the material points grows.

2.4.1 *Boundary treatment*

Inflow boundaries: Since material points at inflow boundaries advect downstream, a scheme is needed to ensure that that they are replaced by inflow of new material points. For the simple simulations in this chapter, we incorporate inflow boundaries by seeding additional material points on a domain that extends beyond the boundaries. Velocities on the extra domain and inflow boundary are set so that the additional material points flow smoothly into the primary domain at the velocity specified by the boundary condition. This scheme is illustrated in Figure 2-2a, where the material point GIMPM domains are dotted grey, the inflow boundary is indicated by the dotted red line, and elements belonging to the additional inflow domain are highlighted in blue. We note that a more efficient, but complicated, scheme may be implemented, where in the "inflow elements" refill with material points automatically as they become empty (Zhao et al., 2019).

Outflow boundaries: At outflow boundaries, material points exit the domain and are removed from the simulation. In the GIMPM, material points with GIMPM domains that overlap an outflow boundary will not receive a full interpolation during grid to material point mappings by default, assuming parameter values are unknown beyond the active portion of the background grid. In Figure 2-2b (left side), a material point GIMPM domain is shown overlapping an outflow boundary (red). For each active element that the GIMPM domain overlaps, our treatment is to temporarily introduce a sub-particle with a GIMPM domain matching the area of overlap between the original material point domain and the element (Figure 2-2b, right side). The sub-particles receive the interpolation, with the original material point then receiving the average of sub-particle values weighted by the area of their subdomains.

Ice front boundary: While the position of the ice front is naturally tracked by material points positions, it will rarely align with element edges. Applying the ice front stress boundary condition along element edges results in large integration errors if the element is not sufficiently full of material points. To mitigate this issue, we forgo material point integration for elements containing the ice front. Instead, we employ Gauss quadrature (i.e. the finite element method) within the element, which allows us to enforce the boundary condition at the element edge that divides active and inactive elements. An illustration of this treatment is shown in Figure 2-2c, where inactive elements are shaded with grey stripes, partially-full ice front elements being approximated with the FEM are shaded with yellow, and the ice front boundary is indicated by the dashed red line. Note that using FEM at the ice front requires mapping the material point history variables used in the SSA solution to the element nodes in the same manner as (2.29). We show in Section 2.5 that using the FEM at the ice front is sufficiently accurate; however, alternative solutions exist if desired. One approach would be to apply the boundary condition

along line segments or B-splines that approximate the sub-element scale location of the ice front (Bing et al., 2019). If using the sMPM, an additional option would be to adjust or replace the mesh to always align with the position of the ice front, and maintain sMPM integration within the element and FEM boundary conventions. This treatment would be possible because sMPM is not restricted to a rectilinear grid.

2.4.2 *Material Point Splitting*

The highly tensile regime of ice shelves tends to cause material points to elongate or grow over time. Material points can be split as necessary to maintain a desired resolution of material points per grid cell. For the GIMPM, we initiate splitting when the domain length l_p exceeds a given threshold. We implement a similar procedure for the sMPM, where a pseudo-domain length is tracked using the accumulated strain of a material point in Cartesian directions (Ma et al., 2009). The splitting threshold cannot exceed the length of a grid cell, and can vary across the domain if, for example, greater material point resolution is desired near the grounding line. For splitting in direction i, the two split material point coordinates, ${}^{s_1}(x_p)_i$ and ${}^{s_2}(x_p)_i$ are set to

$$
\begin{aligned}
{}^{s_1}(x_p)_i &= (x_p)_i + \frac{1}{4}(l_p)_i\,, \\
{}^{s_2}(x_p)_i &= (x_p)_i - \frac{1}{4}(l_p)_i\,.
\end{aligned}
\tag{2.43}
$$

Each new material point is then assigned half the current $\left(l_p^{m+1}\right)_i$ and initial $\left(l_p^0\right)_i$ domain length corresponding to the splitting direction i, from the parent material point being split. For a unidirectional split, the non-split current and initial domain lengths are inherited from the parent material point without modification. The deformation gradient and velocities of the parent

$$ {}^{s}H_p = H_p + \frac{\partial H_p}{\partial x_i}\left[{}^{s}\left(x_p\right)_i - \left(x_p\right)_i\right]. \tag{2.44} $$

material point are transferred directly to the new material points, but direct transfer of thickness may cause visible thickness oscillations in areas of steep thickness gradients. We propose to mitigate these oscillations by instead reassigning thickness to each split material point as

where the thickness gradient, $\frac{\partial H_p}{\partial x}$, must be interpolated from the grid. Figure 2-3 gives the thicknesses for a subset of material points at the end of the steady state flow-band test described in Section 2.5 (GIMPM at 5 km grid resolution and 4 material points per cell), both with and without adjusting thickness according to (2.44). By using (2.44), the thickness oscillations from splitting are almost fully eliminated.

2.5 Examples

In this section, we consider several examples using the GIMPM and sMPM for SSA simulations to validate and test the methods. We quantify error in modeled stress and front propagation versus analytical solutions in 1-D, and further demonstrate front propagation in 2-D. We then test the methods on an idealized marine ice sheet to show that they can maintain steady state grounding line positions over time and can advect passive scalar fields without artificial diffusion.

2.5.1 *Flow-band test case: steady state*

We test our GIMPM-SSA framework against a flow-band model that gives the analytical steady state for a longitudinally unconfined ice shelf with a constant flux at the upstream inflow boundary. The flow-band model is formulated under the assumption of unidirectional flow, and is therefore inherently 1-D. In practice, we model the flow-band in 2-D, where the domain is 1 element wide, but unidirectional flow is still enforced (i.e. $(v_2)_p = 0$). This experiment was previously used to verify a finite-difference front-tracking scheme (Albrecht et al., 2011), and we use the same values for ice density ($\rho = 910$ kg m-3), seawater density ($\rho_w = 1028$ kg m^{-3}), and the flow rate factor ($B = 1.9 \times 10^8$ Pa s$^{1/3}$). The flux at the upstream boundary is given as $Q_0 = v_0 H_0$, where we take the velocity, $v_0 = 300$ m a^{-1} and the thickness, $H_0 = 600$ m. The solution for the spreading rate is given as

$$\frac{\partial v_1}{\partial x_1} = \left(\frac{\rho g}{4B}\left(1 - \frac{\rho}{\rho_w}\right)H\right)^3 = CH^3\,, \tag{2.45}$$

where all flow is along the x_1-axis (Weertman, 1957). The analytical deviatoric stress can be calculated using (2.5) and (2.6). The thickness and velocity profiles are obtained from conservation of mass and momentum are given by $H(x_1) = \left(\frac{4C}{Q_o}x_1 + \frac{1}{H_0^4}\right)^{\frac{1}{4}}$ and $v_1(x_1) = \frac{Q_0}{H(x_1)}$, respectively (van der Veen, 2013).

We first test the ability of the GIMPM-SSA model to maintain the given steady state. We consider a domain that spans from the inflow boundary at $x_1 = 0$ to a fixed ice front $x_1 = 250$ km. The two-dimensional steady-state geometry corresponding to this configuration is shown in Figure 2-4. The initial material point locations fully cover this domain, as well an additional

domain beyond the inflow boundary that must be included to enforce the inflow boundary condition. Note that the analytical solution does not include an ice front, as $H(x_1) = 0$, but including an ice front at any location on the domain will not change the steady-state upstream provided the ice front boundary conditions (2.8) are assigned. Setting the ice front at $x_1 = 250$ km gives a realistic thickness at the ice front of ~219 m. We test the sMPM and the GIMPM at varying material point and grid resolutions, and with and without the reweighting given by (2.26). Each trial is initialized with the analytical solutions for thickness and velocity, and run forward for 300 years using one-month time steps. The threshold material point length at which splitting is initiated is set to 1.5 times the original length. The length after splitting is then 0.75 times the original length, which due to the purely tensile flow regime, therefore constitutes the lower bound on potential lengths that will develop throughout the simulation.

Figure 2-5 shows the deviatoric stress and velocities for the material point initially located closest to $x_1 = 0$ km as it advects to its final location of ~177 km over 300 years. These figures use a 2.5 km mesh, which unless otherwise indicated, are initialized with 9 material points per cell (3×3 in 2-D). Figure 2-5a compares the result that does not use the reweighting scheme from (2.26) with the analytical result. Stresses fluctuate widely due to uneven material point weighting between elements, which results in inaccurate velocities, positions, and thicknesses. Figure 5b gives the velocities from the sMPM when using 9 and 16 material points per cell and the reweighted sMPM when using 4 material points per cell. It is evident that increasing the material point resolution in the sMPM may slightly mitigate the error, but it increases the computational expense and is not nearly as accurate as reweighted sMPM. The reweighted sMPM ensures a smoother transition of the stiffness matrix between elements and even with just 4 material points per cell, and yields results that almost exactly match the

analytical solution. The severity of the error without the reweighting scheme is not common to all MPM simulations, and is likely due to the highly nonlocal stress regime of the SSA. As there appears to be very little tolerance for this type of error, the reweighting scheme from (2.26) appears to be essential for accurate SSA simulations using the sMPM.

The stress response using the reweighted sMPM and the GIMPM are given in Figure 2-5c, and show significant improvement over the sMPM in Figure 2-5a. Note that the reweighting scheme has no effect when implemented with the GIMPM, as no gaps or overlaps of the GIMPM domains develop in the test case. The fit with the analytical solution is less accurate where $x_1 < \sim 40$ km, as ice shelf surface slopes are high and therefore finer mesh resolution is needed for improved accuracy. In generally, the GIMPM is more accurate than the reweighted sMPM, as the latter still does not fully alleviate cell crossing errors. This is evident in Figure 2-5d, which shows the zoom of the region within the grey box from Figure 2-5c. The GIMPM alleviates, but still cannot entirely eliminate the sharp stress discontinuities or oscillations as the material crosses cell boundaries.

We next perform a mesh convergence study to investigate the performance of the reweighted sMPM and the GIMPM, using error measures common to material point methods (e.g. Bing et al., 2019, Wang et al., 2019, Charlton et al., 2017). We evaluate the relative error in deviatoric stress between the modeled and analytical results for a material point at a time step as

$$R_p = \frac{\left|(\sigma_{11}^D)_p^{\mathrm{n}} - (\sigma_{11}^D)_p^{\mathrm{a}}\right|}{\left|(\sigma_{11}^D)_p^{\mathrm{a}}\right|}, \tag{2.46}$$

where superscripts ‘n’ and ‘a’ indicate the numerical and analytical values, respectively. Global error (R_G) at a time step is then computed by summing over all material points as

$$R^{G} = \frac{\sum_p R_p A_p}{\sum_p A_p}, \tag{2.47}$$

Figure 2-6 gives the global error averaged over time for the steady state flow-band test for all combinations of material point and grid resolutions for the reweighted sMPM and the GIMPM. We find that the GIMPM is generally more accurate than the reweighted sMPM. While both methods show a reduction of error with increased grid refinement, the reweighted sMPM is less accurate with fewer material points per element (i.e. 4MPs vs. 9MPs or 16 MPs); whereas, with the GIMPM accuracy is effectively independent of number material points, because the grid-crossing error is adequately alleviated.

2.5.2 *Flow-band test case: front propagation*

We also use the flow-band model to test the ability of our scheme to track the calving front. The analytical position of the ice front, xc, at time t can be found from the relation $Q_0 t = \int_0^{x_c} H(x')dx'$ (Albrecht et al., 2011), and is given by

$$x_c(t) = \frac{Q_0}{4C}\left[\left(3Ct + \frac{1}{H_0^3}\right)^{\frac{4}{3}} - \frac{1}{H_0^4}\right]. \tag{2.48}$$

We track the ice front over 300 years, setting the initial position of the ice front at $x_1 = 0$. Analytical versus modeled front position is plotted in Figure 2-7. The modeled front position is evaluated using the GIMPM with a 2.5 km grid and 9 material points per grid cell. The fit is nearly perfect, with a maximum deviation from the analytical position of only 26 meters. Both the reweighted sMPM and the GIMPM for all grid and material point resolutions achieve results nearly indistinguishable from the analytical front position over time, with none of the simulations deviating from the analytical front position by more than 10% of a single grid cell length. Thus,

this study demonstrates that the GIMPM can accurately simulate the stresses, geometry, and ice front position of an evolving ice shelf.

2.5.3 *Front advection in 2-D*

To test our front propagation scheme in 2-D, we simulate the radial spread of an unconstrained floating ice tongue. This benchmark example was considered under steady-state conditions in previous studies (e.g. Morland and Zainuddin, 1987; Pegler and Worster 2012, 2013; Wearing et al., 2020). Our aim here is to achieve only qualitatively consistent results, because there is no analytical solution for 2-D diverging ice flow. The setup of this the simulation follows Example 1 in Wearing et al. (2020). We use sMPM rather than GIMPM, as this simulation is best performed on a grid without perfectly rectilinear elements. However, recall that sMPM is a special case of GIMPM that uses the Dirac delta function instead of the hat function for χ_p, the particle characteristic function. The grid is shown in Figure 2-8a. The curved upstream boundary (red) corresponds to an arc extracted from a circle with 70 km radius with a central angle of 10˚. Flow is axisymmetric with respect to the vertical axis defined at the center of the circle, and we set free slip conditions at the lateral boundaries by enforcing that the normal component of velocity is zero. At the upstream boundary, a constant thickness of 400 m and an inflow velocity of 500 m a^{-1} is enforced. We evenly initialize 9 material points per cell on an inflow domain beyond the upstream boundary (not shown), and allow the system to evolve until the ice front reaches the downstream edge of the computational grid, which occurs after 86.6 years.

The corresponding final thicknesses and positions of all material points are plotted in Figure 2-8b. The thicknesses of all material points at any radial distance match very closely regardless of their azimuthal position, reflecting that the simulation has achieved the expected

axisymmetric flow regime. Also plotted is the steady-state thickness profile as calculated using the FEM under the assumption that the calving front is fixed at the downstream edge. While it is encouraging that the two thickness profiles show similar trends, we emphasize that unlike in the 1-D case, we do not expect a simulation with a moving ice front to replicate the steady state flow exactly. Some mismatch is expected because an unconstrained ice tongue experiences buttressing that increases proportionately with ice tongue length (Wearing et al., 2010). This buttressing is related to "hoop" stresses that must be overcome for flow to diverge laterally. In Figure 2-8b, the material points towards the ice front are relatively thin compared to the steady state because they endured larger rates of spreading earlier in the simulation when the ice tongue was short and buttressing was lesser. This example demonstrates that material point methods can be used for 2-D ice front tracking in a physically-consistent manner.

2.5.4 *Marine Ice Sheet Model Intercomparison Project (MISMIP+)*

Our final experiment tests the ability of our model to maintain the steady state from the idealized, but more realistic, geometry detailed in the MISMIP+ (Asay-Davis et al., 2016). This geometry is a 640 km × 80 km marine ice sheet, spanning an ice divide at $x_1 = 0$ km to a calving front at 640 km. At steady state, the grounding line is centered at $x_1 \sim 450$ km and $x_2 = 40$ km. At the lateral boundaries, $v_2 = 0$. The steady state grounding configuration where $x_1 > 350$ km is shown in Figure 2-9a. The grounding line lies on a retrograde slope, and is therefore very sensitive to perturbations or error, so that the configuration is ideal for testing the accuracy of the GIMPM. Furthermore, this is a very high shear regime, which is often problematic for the MPMs. Therefore, we update GIMPM domains with the corner-tracking scheme from (2.38)–(2.40).

We initially determine the steady state using the FEM according to the recommended values for the friction parameter, the viscosity parameter, the rate factor, densities, and surface accumulation given for the MISMIP+. Afterwards, we continue the simulation using both the GIMPM and the reweighted sMPM. We use a 0.5 km grid and initialize the simulation with 9 material points per cell. After 100 years, both the GIMPM (Figure 2-9b) and the reweighted sMPM (Figure 2-9c) are able to maintain the sensitive initial grounding line position (Figure 2-9a). The reweighted sMPM grounding line region, however, is slightly noisier than GIMPM that is only visible in a close-up view of the image in Figure 2-9c (zoom not shown).

During the simulation, we also advect a passive scalar field to demonstrate how when using the GIMPM, this field can be advected without artificial diffusion. This field is initially assigned a value of unity along a series of 0.5 km vertical strips, which are each separated by 50 km in the x_1-direction, and a value of zero elsewhere (Figure 2-10a). We chose the width of the strips to roughly correspond to the width of an ice shelf rift, which can range from zero to several kilometers wide. The field was initially assigned on the grid, and interpolated to the material points before the simulation. For comparison, we ran the same simulation using the Discontinuous Galerkin (DG) method, the least-diffusive Eulerian advection method already available in Elmer/Ice. The advected profiles of the scalar field obtained from the GIMPM are shown in Fig. 10b after 5 years and Fig. 10c after 100 years. The scalar field does not experience artificial diffusion, and takes an arcuate shape over time that reflects the high shear experienced from the lateral grounded margins. The results from the DG method are shown in Fig. 10d after 5 years and in Fig. 10e after 100 years. Although the DG method produces a similar arcuate profile for the scalar field as the GIMPM, the value of the scalar field is diminished due to numerical diffusion over time. We initially set the maximum value of the scalar as 1.0 in the rift regions.

With the DG method, the furthest downstream values of the scalar near the centerline of the y-domain (y=40 km) quickly diminish to ~0.7 over 5 years, and the originally sharp vertical strip diffuses over a width about three times its initial width. By 100 years, the diffusion increases in severity, and the values of the scalar near the centerline diminished to ~0.2. With the GIMPM, the maximum values of the scalar field are maintained at 1.0. Thus, this simulation study illustrates the superior performance of the GIMPM, based on a hybrid Lagrangian-Eulerian framework, in alleviating numerical diffusion issues persistent with the DG method in a purely Eulerian framework.

Figure 2-11 shows the maximum principal deviatoric stress, $\sigma_{\max}^{\mathrm{D}}$, for the MISMIP+ test obtained using the GIMPM and the reweighted sMPM after t = 100 years. The initial $\sigma_{\max}^{\mathrm{D}}$ is given in Figure 2-11a, where the largest stresses are concentrated near the lateral grounding line. The GIMPM field after 50 years (Figure 2-11b) is almost identical to the initial field. The reweighted sMPM field at 50 years (Figure 2-11d) while mostly identical to the initial field, however, is characterized by oscillations due to grid-crossing error, which also cause the noise in the grounding line configuration in Figure 2-9c. By 100 years, both the GIMPM (Figure 2-11c) and the reweighted sMPM (Figure 2-11e) stress fields develop some artifacts in the stress field near the grounding line, as material points tend to become poorly distributed under extreme shear (Figure 2-12). This type of error is a limitation of our current GIMPM implementation; we discuss potential approaches to alleviate it in Section 2.6.

2.6 Discussion

Our current GIMPM or reweighted sMPM formulations should be sufficiently accurate for many applications in which it is essential to accurately track the ice front or history variables, such as

damage (Chapter 3). However, additional developments are needed to mitigate the artifacts introduced due to intense distortion of material point domains in high shear regimes over long timescales (Section 2.5.4). One approach is to reinitialize the material points periodically, which in the simplest case would involve interpolating all material point properties to a new set of material points. Although this approach risks some artificial diffusion, it may be negligible if reinitialization is infrequent. However, more sophisticated schemes are also available that reinitialize material points locally as needed, while minimizing artificial diffusion (e.g., Yue et al., 2015).

Further development of our method will likely include implementing more robust shape functions. For example, Convected Particle Domain Interpolation (CPDI) methods assemble shape functions according to the shapes of the material point domains, and alleviate cell-crossing error. Unlike the GIMPM, CPDI methods are not restricted to tracking rectangular domains, and instead may track parallelograms (CPDI1; Sadeghirad et al., 2011) or the corners of the domains individually (CPDI2; Sadeghirad et al., 2013). The CDPI1 method has been shown to perform especially well under intense shearing (Wang et al., 2019), and may be appropriate for avoiding the errors related to high-shear observed in our GIMPM simulations over long timescales. However, we note that our current GIMPM formulation is computationally less expensive and easier to implement into existing finite element codes. Implementing CPDI methods will require substantial modifications to our current discretization scheme and boundary treatment.

As an alternative to using material point domain-tracking shape functions, it may also be advantageous to consider techniques that eliminate cell-crossing error through other means, such as the dual domain material point (DDMP) method (Zhang et al., 2011) or the use of spline-based shape functions (e.g. Stomakhin et al., 2013). All of these techniques, including CPDI,

share an additional advantage over the GIMPM in that they may be employed using non-uniform meshes of varying element types, such as triangular meshes commonly used in major ice flow codes (e.g. ISSM and Elmer/Ice). Analyzing the error, convergence qualities, and speed of these methods in the context of ice shelf flow and fracture will constitute future research.

Although not illustrated in this chapter, an additional advantage of our GIMPM-SSA model is that complex 3-D multiphysics can be represented while still being efficient enough to couple with Earth system models. Because horizontal velocities are vertically-invariant within the SSA framework, 3-D processes can be approximated locally with each material point using a series of vertical layers, and subsequently vertically integrated if needed for implementation into the next SSA solution. While the same can be applied to mesh-based Eulerian methods, the associated advection schemes are not only dissipative, but scale in computational expense with the number of layers used. However, as for 2-D variables, advection of a 3-D field for material point methods within a shallow shelf framework avoids artificial diffusion and only requires updating material point locations. We employ this 3-D approach to model damage evolution in ice shelves in Chapter 3; however, other potential applications of the approach include modeling coupled processes such as temperature evolution, firn compaction, fabric anisotropy, and marine ice formation. We also note that a full 3-D implementation of material point methods for full-Stokes models is also possible for studying individual glaciers, but it would be prohibitively expensive for continental-scale ice sheets.

2.7 Conclusion

We presented the generalized interpolation material point method for shallow shelf ice flow, and verified that this formulation can reproduce and maintain analytical solutions for steady state ice flow and ice front advection. The advantages of this formulation include:

1. Error-free Lagrangian advection or transport without numerical diffusion or dispersion
2. Computationally inexpensive, explicit time updates for ice thickness and history variables, such as damage
3. Natural tracking of the ice front and grounding line at sub-element scale
4. Accurate schemes for boundary treatment and redistribution of thickness during particle splitting that facilitate simulations over long timescales.
5. Consistent with the well-established conventions of the finite element method for shallow shelf ice flow

By choosing the particle characteristic functions to be either the Dirac delta or the 'hat' functions, the present formulation can reproduce the existing implementations of sMPM and the GIMPM. We demonstrated that the sMPM shape functions are very sensitive to cell-crossing errors and uneven distributions of material points, likely due to the quasi-static and highly nonlocal stress regime of the SSA. By simply modifying the shape functions with a reweighting scheme in the sMPM, we can significantly decrease this sensitivity to cell-crossing errors. This numerical error is almost entirely alleviated using the GIMPM without the reweighting scheme, so it is more appropriate for many applications on timescales of decades to centuries. A major advantage of the reweighted sMPM over the GIMPM is that it is applicable with adaptive and non-uniform quadrilateral and triangular mesh discretization, which is ideal for accurately resolving grounding line dynamics. Future work is necessary to mitigate errors in the GIMPM

associated with the intense distortion and gaps in the material point distribution observed in high shear regimes over long timescales. Potential solutions for this error involve developing material point reinitialization schemes, improving GIMPM domain updating schemes, and/or implementing different shape functions. In addition, future developments should focus on implementing additional physics to fully take advantage of the GIMPM-SSA treatment of history variables; this could be particularly beneficial when parameterizing complex 3-D processes using a series of vertical layers assigned to each material point. Thus, the GIMPM-SSA model can potentially develop into a powerful tool for studying large-scale, coupled ice sheet processes simultaneously, thus enabling the accurate prediction of ice sheet response to climate change and eventually global sea level rise.

Acknowledgements

Huth was funded by NASA Earth and Space Sciences fellowship under grant no. NNX15AN99H. Duddu gratefully acknowledges the funding support provided by the National Science Foundation's Office of Polar Programs via CAREER grant \#PLR-1847173. Smith was funded under the NASA grant no. NNX13AP6.

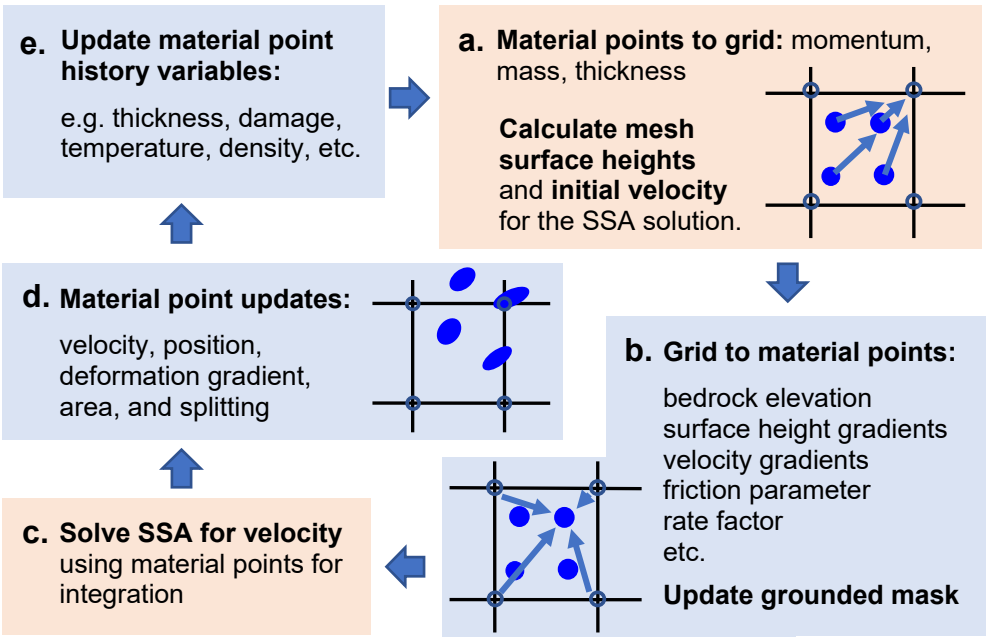

Figure 2-1. MPM-SSA numerical procedure

Grid processes (Eulerian) are highlighted in red and material point processes (Lagrangian) are highlighted in blue.

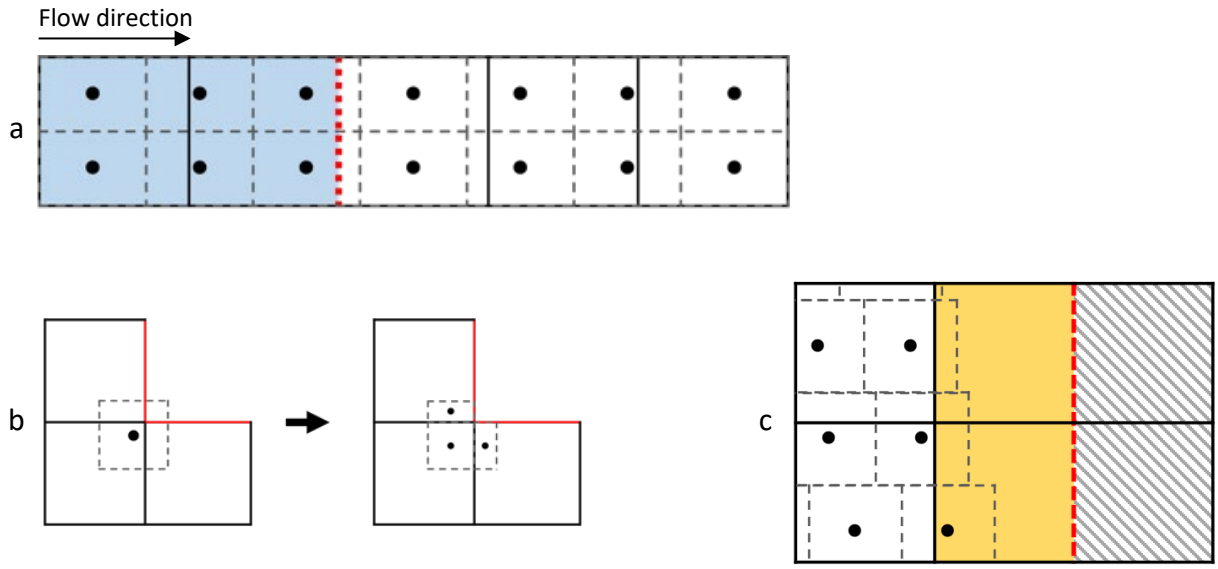

Figure 2-2. MPM-SSA boundary treatment

(a) At inflow boundaries (dotted red), an additional domain (shaded blue) is specified upstream and seeded with extra material points. Velocities are specified throughout the additional domain so that the extra material points advect into the primary domain at the correct velocity. **(b)** A material point with a GIMPM domain overlapping an outflow boundary (red) is split into sub-particles during grid-to-material point mappings. The sub-particles separately receive the interpolation, which is subsequently consolidated back to the original material point. **(c)** At the ice front, grid cells partially full with material points (yellow) are integrated using the FEM, where the boundary condition is assigned at the element edges (dashed red) that mark the transition between active and inactive (grey-striped) grid cells.

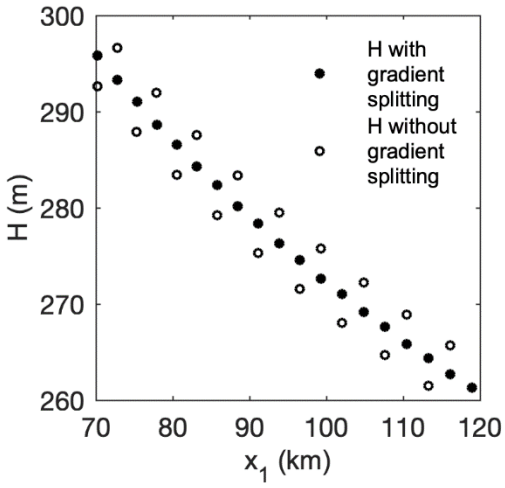

Figure 2-3. Thickness adjustment during material point splitting

Thickness for a subset of material points at the end of the steady state flow-band test with and without adjusting thickness according to its gradient during splitting. This simulation used the GIMPM at 5 km grid resolution and 4 material points per cell.

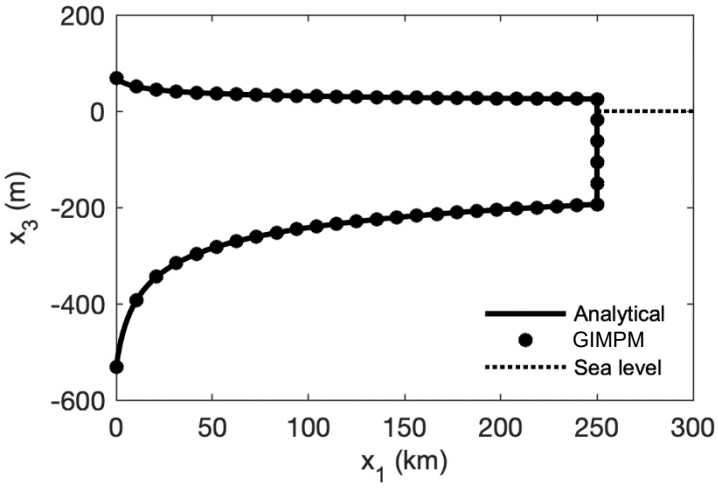

Figure 2-4. Flow-band test: geometry

Analytical steady state ice geometry for the flow-band test and the GIMPM solution at 300 years using a 2.5 km resolution grid and 9 material points per cell.

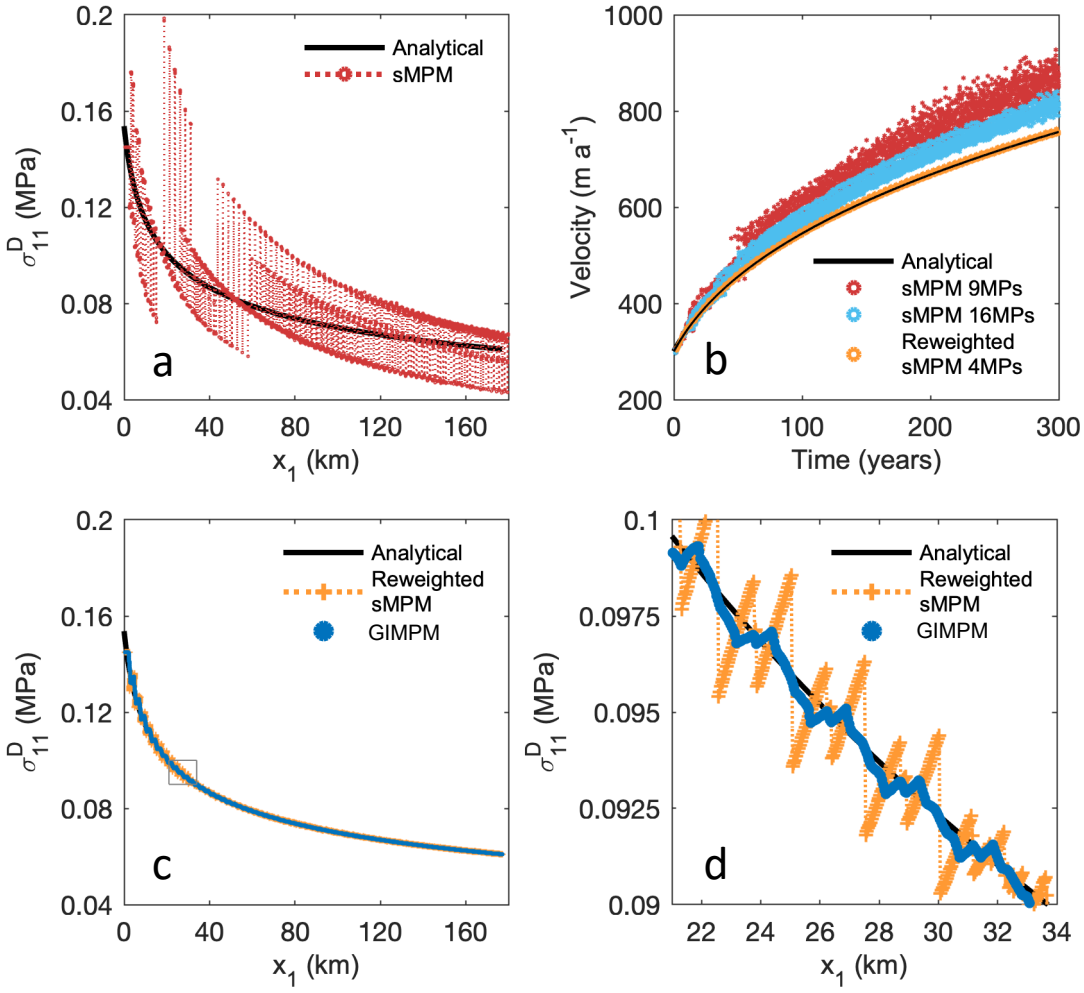

Figure 2-5. Flow-band test: stress and velocity

Results from the steady state flow-band test for the material point initially located closest to 0 km, where 9 material points are initialized per 2.5 km grid cell. **(a)** Deviatoric stress using the unweighted sMPM. **(b)** Velocities corresponding to **(a)** compared to the velocities obtained using 16 material points per cell, as well as the velocities using the reweighted sMPM with only 4 material points per cell. **(c)** Deviatoric stress using the reweighted sMPM and the GIMPM, which closely match the analytical result. **(d)** Detail of the boxed region in **(c)**. The discontinuities for the reweighted sMPM are caused by the grid-crossing error, and are largely alleviated using the GIMPM.

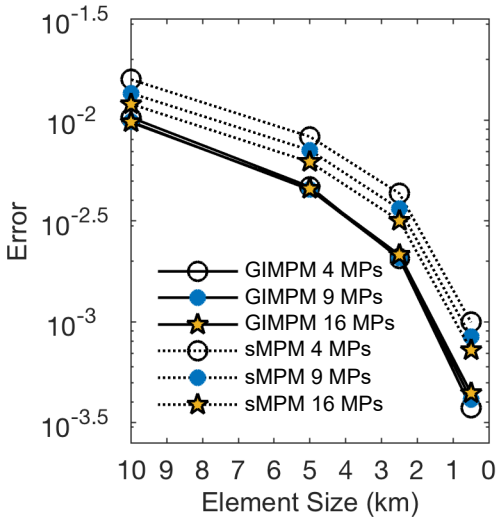

Figure 2-6. Flow-band test: stress error

Deviatoric stress error from the steady state flow-band test for the GIMPM and the reweighted sMPM.

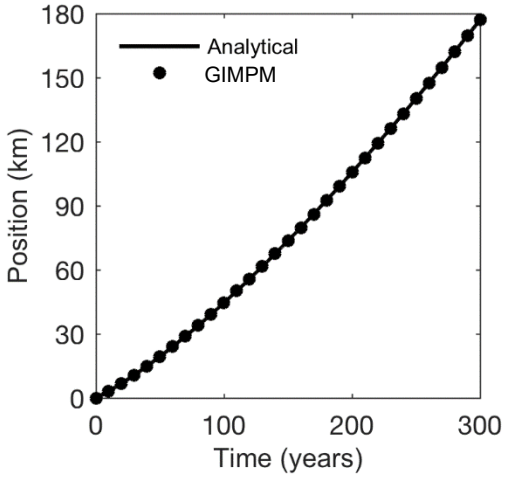

Figure 2-7. Flow-band test: ice front position

Ice front position using the GIMPM plotted against the analytical solution using 9 material points per 2.5 km grid cell.

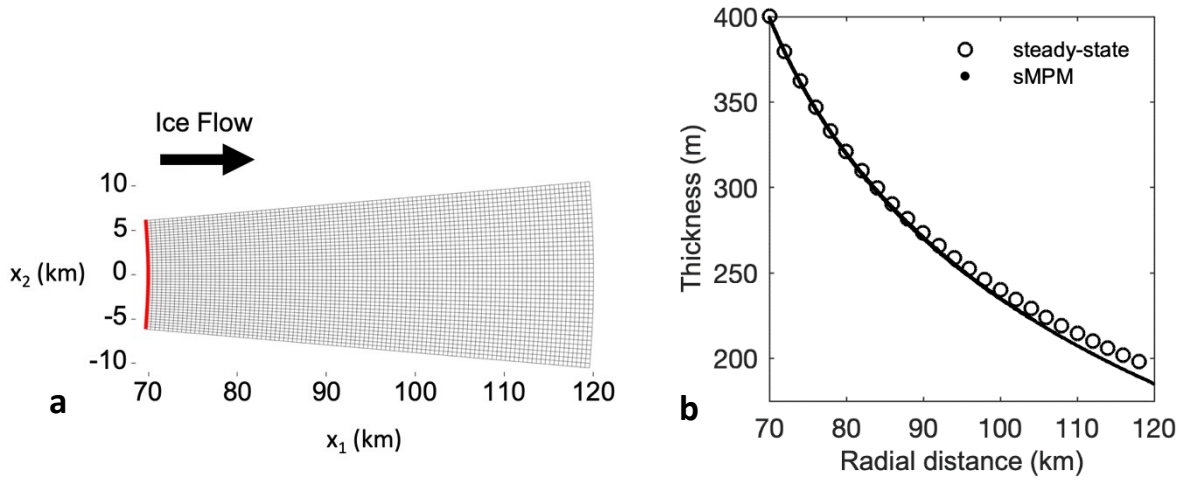

Figure 2-8. Unconstrained 2-D spreading of an ice tongue

(a) Background grid used to simulate the unconstrained 2-D spreading of an ice tongue from an upstream boundary (red) with a 70 km radius of curvature. **(b)** The ice thicknesses of all material points after growing the ice tongue from the upstream boundary for 86.6 years, and the steady-state thickness profile calculated from the FEM using the same ice front position. Material point thicknesses are slightly lesser towards the ice front due to the increased rate of spreading these material points experienced earlier in the simulation, when the ice tongue was shorter and buttressing was lesser.

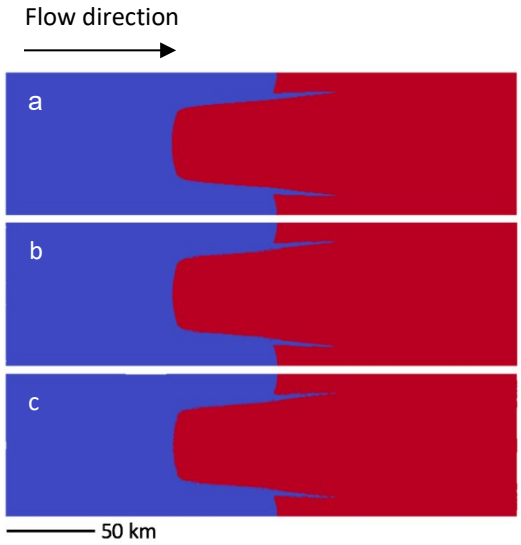

Figure 2-9. MISMIP+: grounding line over time

(a) Grounding line at 0 years after initiating the GIMPM/sMPM, where blue material points are grounded and red are floating. The configuration after 100 years is shown for **(b)** the GIMPM and **(c)** the sMPM

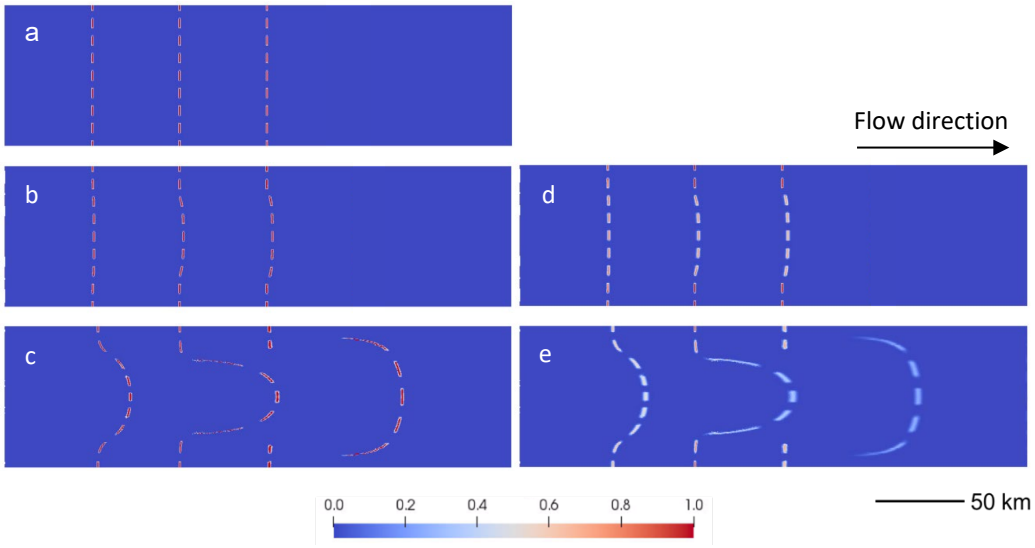

Figure 2-10. MISMIP+: advection of a passive scalar

Results shown for same area as Figure 2-9 around the grounding line for the GIMPM versus Discontinuous Galerkin (DG). The initial state is given in **(a)**. The field at 5 years is shown for **(b)** the GIMPM and **(d)** DG. The field at 100 years is shown for **(c)** the GIMPM and **(e)** DG.

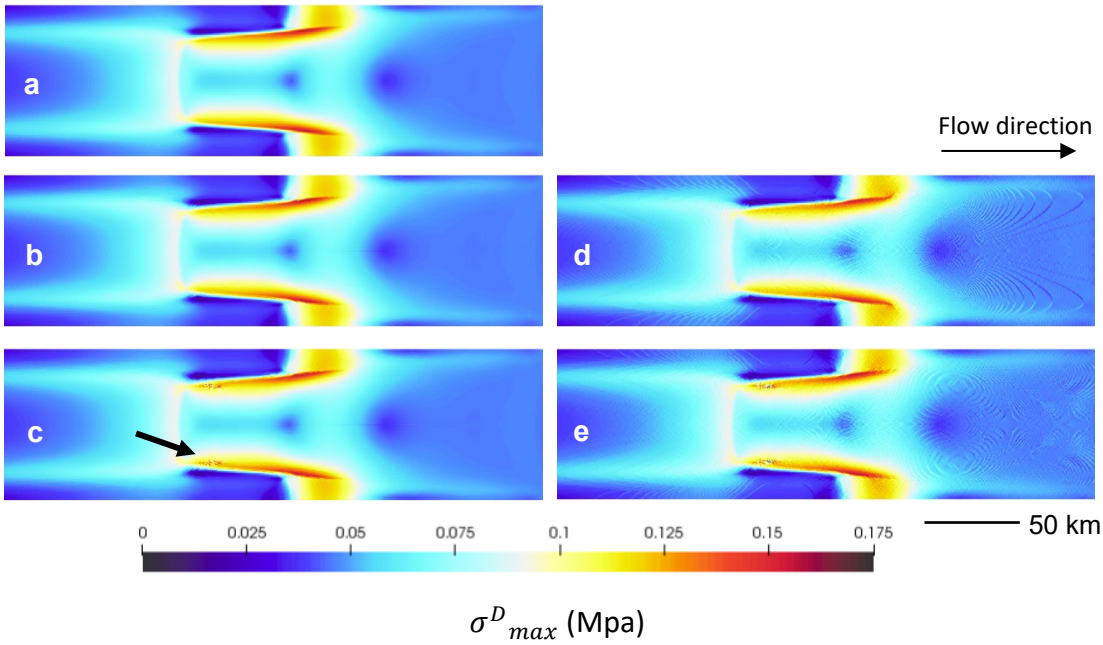

Figure 2-11. MISMIP+: stress over time

Maximum principal deviatoric stresses (Mpa) for the **(a)** initial state, **(b)** GIMPM at 50 years, **(c)** GIMPM at 100 years, **(d)** reweighted sMPM at 50 years, **(e)** reweighted sMPM at 100 years. The arrow in **(c)** indicates where continual heavy shear eventually causes poorly distributed material points, as shown in detail in Figure 2-12.

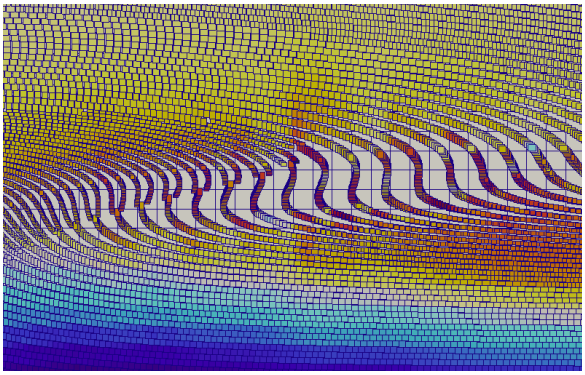

Figure 2-12. MISMIP+: GIMPM shear error

Poorly distributed material points develop in the GIMPM simulation after 100 years of heavy shear, where indicated by the arrow in Figure 2-11c. Underlying grid resolution is 0.5 km.

Chapter 3. A generalized interpolation material point method for shallow ice shelves. Part II: anisotropic nonlocal damage mechanics and rift propagation

Abstract

Ice shelf fracture is responsible for roughly half of Antarctic ice mass loss in the form of calving and can weaken buttressing of upstream ice flow. Large uncertainties associated with the ice sheet response to climate variations are due to a poor understanding of these fracture processes and how to model them. Here, we address these problems by developing an anisotropic, nonlocal, creep damage model for large-scale shallow-shelf ice flow. This model can be used to study the full evolution of fracture from initiation of crevassing to rifting that eventually leads to tabular calving. While previous ice shelf fracture models have largely relied on simple expressions to estimate crevasse depths, our model parameterizes fracture directly in 3-D. We also develop an efficient supporting numerical framework based on the material point method, which avoids advection errors. Using an idealized marine ice sheet, we test our methods in comparison to a damage model that parameterizes crevasse depths, as well as a modified version of the latter model that accounts for how necking and mass balance affect damage. We demonstrate that the creep damage model is best suited for capturing weakening and rifting, and that anisotropic damage reproduces typically observed fracture patterns better than isotropic damage. However, we also show how necking and mass balance can significantly influence damage on decadal timescales. Because these processes are currently absent from the creep damage parameterization, we discuss the possibly for a combined approach between models to best represent mechanical weakening and tabular calving within long-term simulations.

3.1 Introduction

Fracture of ice shelves strongly impacts the evolution of the Antarctic Ice Sheet and its interaction with climate. Approximately half of ice mass loss is attributed to fracture-induced calving, while the other half is attributed to ocean-driven basal melting (Depoorter et al., 2013; Rignot et al., 2013; Paolo et al., 2015). Furthermore, mechanical weakening associated with fracture processes can decrease ice shelf buttressing of upstream grounded ice flow into the ocean, leading to sea level rise (e.g. Borstad et al., 2013; MacGregor et al., 2012). For example, the Antarctic glaciers that will likely contribute the most to sea level rise in the next centuries, Pine Island and Thwaites, are buttressed by ice shelves that contain only a limited region of ice that can be lost or weakened without dynamic consequences that would lead to increased mass loss from the grounded ice sheet (Fürst et al., 2016). In extreme cases, fracture can eliminate buttressing entirely if full ice shelf collapse occurs, as it did when the Larsen B Ice Shelf collapsed over a period of just 6 weeks in 2002, likely due to hydrofracture (Scambos et al., 2004) related to surface meltwater ponding enabled by rising surface air temperatures. Fracture is also interconnected with climate through ocean processes. Ocean driven basal-melting of ice shelves can cause thinning that makes ice shelves more vulnerable to fracture (Shepherd et al., 2003; Liu et al., 2015). In turn, calved tabular icebergs can alter ocean circulation (e.g. Robinson et al., 2020; Stern et al., 2015, 2016; Cougnon et al., 2017).

The importance of ice shelf fracture processes to ice sheet and climate dynamics motivates their incorporation into prognostic flow models of ice sheet-ice shelf systems to better assess ice shelf stability and project ice sheet response to climate change. An efficient, accurate, and commonly-used ice flow model for these systems is the Shallow Shelf Approximation (SSA), a 2-D vertically-integrated form of the incompressible Stokes equations. Prognostic

representation of fracture in SSA models has ranged from simple calving parameterizations to explicitly modeling fracture evolution and its feedback on flow using damage variables. For calving alone, reasonable ice front positions have been obtained by parameterizing smooth calving rates (e.g. Alley et al., 2008; Levermann et al., 2012) or attempting to track crevasse depths over time, where crevasses are assumed to propagate to the depth where the horizontal Cauchy stress equals zero (e.g. Nye, 1957; Nick et al., 2010; Nick et al. 2013; Pollard et al., 2015). This "zero-stress" approach assumes crevasse depths are in equilibrium with the stress field, and has been further developed into damage models that may be used with the SSA (Sun et al., 2017; Bassis & Ma, 2015). Other SSA damage models do not explicitly track crevasse depths. For example, an SSA damage model was formulated by fitting a relationship between stress and damage fields inferred from observations of Larsen B Ice Shelf, but was mostly successful near the ice margins only and did not capture rifting (Borstad et al., 2016). Another SSA damage model tested a variety of *ad hoc* measures for initiating fracture, but the approach was only sufficient for broadly capturing the feedback between flow dynamics and fracture-induced weakening (Albrecht & Levermann, 2012; Albrecht et al., 2014).

An alternative approach to the above models for parameterizing ice shelf fracture is to implement traditional creep damage mechanics, where damage generalizes the nucleation and accumulation of microcracks and their influence on flow (Lemaitre, 1992). A creep damage model of this type (Murakami and Ohno, 1980; Murakami, 1983; Murakami et al., 1988) has already been calibrated for ice flow according to laboratory data (Pralong & Funk, 2005; Pralong et al., 2006; Duddu & Waisman, 2012). This damage model is time-dependent, which allows better calibration to observed, dynamic fracture. Furthermore, the model may be implemented in isotropic or anisotropic form, where anisotropic damage is likely more consistent with the

heavily-patterned fractures observed on ice shelves. While it has only been tested at the scale of individual crevasses and in isotropic form, this creep damage model has proved to be accurate enough to reasonably simulate two calving events in the Swiss Alps within a 2-D full-Stokes study (Pralong & Funk, 2005). Further progress with the isotropic creep damage model at similar spatial scales has included additional calibration for temperature dependence (Duddu & Waisman, 2012), nonlocal formulations (Duddu & Waisman, 2013; Duddu et al., 2013; Londono et al., 2017; Jimenez et al., 2017), and a modification to incorporate the effects of water pressure (Mobasher et al., 2016; Duddu et al., 2020). To our knowledge, only one study has considered parameterizing this damage model for application into SSA simulations of large-scale ice flow (Keller & Hutter, 2014). This study proposed updating the isotropic creep damage field in 3-D using parameterized Cauchy stresses, and vertically-averaging a 3-D damage-modified viscosity parameter for implementation into the 2-D SSA solution. However, this parameterization remains untested, potentially due to the inhibiting computational expense and complexity of actually implementing such a parameterization within existing ice flow models.

The overarching goal of this chapter is to develop an SSA creep damage parameterization and modeling framework that can be used to represent the entire progression of ice shelf fracture, from initiation and evolution of subcritical damage to propagation of sharp rifts and calving of tabular icebergs. Our approach builds on the SSA parameterization proposed by Keller and Hutter (2014). We modify the model for an anisotropic creep damage variable, and construct a supporting numerical framework that minimizes error and maximizes efficiency so that it may be applied effectively within large-scale ice flow simulations. We adapt several schemes for this framework that improve model performance and physical consistency, including extension of the damage variable to nonlocal form, adaptive time-stepping based on damage accumulation, brittle

rupture criteria, and numerical treatment once maximum damage is reached. The damage model is implemented within our generalized interpolation material point method (GIMPM) code, a hybrid Lagrangian-Eulerian particle variation of the finite element method (Chapter 2). Traditional Eulerian ice flow models are subject to artificial diffusion when advecting the damage field (e.g. Albrecht & Levermann, 2014; Borstad et al., 2016), whereas this error is avoided when using our GIMPM-SSA model, thereby allowing sharpness of cracks to be preserved regardless of flow. Additionally, the GIMPM-SSA model drastically increases the computational efficiency of advecting the 3-D damage field, or any other 3-D field such as temperature.

We test the SSA creep damage model on an idealized marine ice sheet system (Asay-Davis et al., 2016) to demonstrate that it can capture all damage growth from initial accumulation to sharp rifting and tabular calving, and to conduct parameter sensitivity tests. We show, for example, that high level of creep damage anisotropy results in rifting more consistent with the sharp, arcuate patterns observed on ice shelves. Furthermore, we compare the performance of our model with two previously-proposed crevasse-depth-based damage models (Sun et al., 2017; Bassis & Ma, 2015), which we also extend from isotropic to anisotropic form. These comparisons clarify the physical relationships between the damage models and the numerical advantages of our framework. We confirm that the creep damage model is better suited for capturing initiation of damage, rifting, and calving. However, only the Bassis and Ma (2015) damage model accounts for the impact of mass balance and necking processes, and we discuss how these processes may alter damage evolution significantly, especially regarding damage healing over decades. Thus, we conclude that a combined approach between the two models may be a viable approach for accurately simulating large-scale ice shelf fracture

processes on decadal timescales, which will be the focus of a future paper. The outline of this chapter is as follows: in section 3.2 we summarize the governing equations, including the SSA and damage parameterization; in section 3.3 we detail the implementation of the damage model; in section 3.4 we present the idealized ice sheet experiments; in section 3.5 we discuss the results and potential future developments and applications; and in section 3.6 we offer concluding remarks.

3.2 Governing Equations

We begin this section by briefly reviewing the SSA equations. Then, we present the creep damage model and its parameterization for the SSA. We use a mix of tensorial and indicial notation as needed for conciseness or clarity. Vectors are donated as $\boldsymbol{a} = a_i \hat{e}_i$, where the indicial notation of the right-hand side is framed within a Cartesian coordinate system $(x_1, x_2, x_3) = (x, y, z)$, where i are the spatial indices and $\hat{e}_i$ are the orthonormal basis vectors. Second-order tensors are similarly denoted as $\boldsymbol{A} = A_{ij} \hat{e}_i \otimes \hat{e}_j$, where $\otimes$ is the dyadic product of two vectors. We assume Einstein's convention of summation that repeated indices imply summation. Principal values of $\boldsymbol{A}$ are written as $\langle A_i \rangle$, where in this case, index i indicates principal components rather than Cartesian directions. Variables at time step m are indicated using the superscript $\boldsymbol{A}^m$.

3.2.1 *Shallow Shelf Approximation*

Ice streams and ice shelves have little or no basal friction, so vertical shear is negligible. Consequently, horizontal velocities and the corresponding strain-rates can be assumed constant with depth. Excluding vertical shear components from the incompressible Stokes equations and

vertically integrating yields the 2-D shallow shelf approximation, or SSA (MacAyeal, 1989; Weis et al., 2001)

$$\frac{\partial T_{ij}}{\partial x_j} + (\tau_{\mathrm{b}})_i = \rho g H \frac{\partial s}{\partial x_i}, \tag{3.1}$$

where i ranges over {1,2} to indicate the horizontal $x_1 - x_2$ plane, ρ is ice density, g is acceleration due to gravity, H is ice thickness, s is surface height above sea level, $\tau_{\mathrm{b},i}$ are the components the shear stress vector tangential to the glacier base, and T_{ij} is the vertically-integrated stress tensor

$$T_{ij} = 2\bar{\eta} H\left(\dot{\varepsilon}_{ij} + (\dot{\varepsilon}_{11} + \dot{\varepsilon}_{22})\delta_{ij}\right). \tag{3.2}$$

In (3.2), $\dot{\varepsilon}_{ij}$ is the strain rate tensor and $\bar{\eta}$ is the depth-averaged viscosity

$$\bar{\eta} = \frac{1}{2}\bar{B}\dot{\varepsilon}_e^{\frac{1-n}{n}}, \tag{3.3}$$

where, $\dot{\varepsilon}_e$ is the scalar effective strain rate, n is Glen's Law exponent set to $n = 3$, and $\bar{B}$ is the depth-averaged flow rate factor. At the ice-ocean boundary (or ice front), the sea water pressure is applied using a depth-integrated Neumann boundary condition as

$$\int_b^s \sigma_{ij}\hat{n}_j \, \mathrm{d}z = -\frac{1}{2}\rho_{\mathrm{w}} g b^2 \hat{n}_i, \tag{3.4}$$

where $\boldsymbol{\sigma}$ is the Cauchy stress, $\hat{\boldsymbol{n}}$ is the unit (outward) normal to the ice front, ρ_w is sea water density, and b is the elevation of the ice shelf base below sea level (Morland & Zainuddin, 1987). The SSA is solved for the in-plane velocity components (v_1, v_2) of the ice shelf/stream by reformulating (3.1) and (3.2) in terms of the velocity gradients derived from the strain rate tensor $\dot{\varepsilon}_{ij} = \frac{1}{2}\left(\frac{\partial v_i}{\partial x_j} + \frac{\partial v_j}{\partial x_i}\right)$.

3.2.2 *Physical notion of continuum damage*

We implement the anisotropic creep damage model originally proposed by Murakami and Ohno, (1980) and Murakami (1983,1988) for polycrystalline metals. Pralong and Funk (2005) first calibrated this model for glacier ice and discussed the thermodynamic considerations in Pralong et al. (2006). Damage is represented as a real-valued, symmetric second-order 3-D tensor, **D**, so that anisotropy is restricted to an orthotropic description where damage is tracked on three mutually perpendicular planes. The damage tensor has three real principal values, $\langle D_i \rangle$, each representing the ratio of the area of cracks or voids to the originally undamaged area along the principal plane with a normal corresponding to principal direction *i* (Murakami, 1983; Duddu & Waisman, 2013). This physical or geometric interpretation is valid under isotropic ($\langle D_1 \rangle = \langle D_2 \rangle = \langle D_3 \rangle$) and orthotropic damage (Qi & Bertram, 1999). Each principal damage component is bounded by $0 \leq \langle D_i \rangle \leq D_{\max}$, where a material point is undamaged if all $\langle D_i \rangle = 0$ and fully damaged if any $\langle D_i \rangle = D_{\max}$. Setting $D_{\max}$ to the maximum possible value of unity corresponds to complete loss of strength, though numerically, $D_{\max}$ must be set less than unity to prevent the SSA from becoming an ill-posed problem. Given the plug-flow regime of the SSA, we assume that the damage tensor is oriented so that one principal component, which we denote as $\langle D_3 \rangle$, always aligns with the vertical x_3 axis ($\langle D_3 \rangle = D_{33}$). The other two principal axis lie in the horizontal $x_1 - x_2$ plane, where we always ensure $\langle D_1 \rangle \geq \langle D_2 \rangle$. Because vertical shear stress components are zero in the SSA, the orthotropic damage tensor has only four non-zero components D_{11}, D_{22}, D_{33}, and D_{12} that need to be determined.

The damage evolution function and incorporation of the damage tensor into the SSA rely on the principle of strain equivalence (Lemaitre, 1971; Lemaitre & Chaboche, 1978). This

principle states that strain is identical for a damaged state under the applied stress, σ_{ij} (force per area of ice, including voids), as for its undamaged state under the effective stress, $\tilde{\sigma}_{ij}$ (force per ice area, ignoring any voids). A linear transformation between the two stress spaces that ensures the symmetry of the effective stress tensor can be written as

$$\tilde{\boldsymbol{\sigma}} = \frac{1}{2}[(\mathbf{I}-\mathbf{D})^{-1}\boldsymbol{\sigma} + \boldsymbol{\sigma}(\mathbf{I}-\mathbf{D})^{-1}], \tag{3.5}$$

where **I** is the second-order identity tensor. The effective deviatoric stress may be defined as (Pralong and Funk, 2005; Pralong et al., 2006)

$$\tilde{\boldsymbol{\sigma}}^{\mathrm{D}} = \frac{1}{2}[(\mathbf{I}-\mathbf{D})^{-1}\boldsymbol{\sigma}^{\mathbf{D}} + \boldsymbol{\sigma}^{\mathbf{D}}(\mathbf{I}-\mathbf{D})^{-1}]^{\mathrm{D}}. \tag{3.6}$$

An effective strain-rate is used to incorporate damage into the constitutive relation and calculate the applied stress, and takes the form

$$\tilde{\dot{\boldsymbol{\varepsilon}}} = \frac{1}{2}[(\mathbf{I}-\mathbf{D})\dot{\boldsymbol{\varepsilon}} + \dot{\boldsymbol{\varepsilon}}(\mathbf{I}-\mathbf{D})]^{\mathrm{D}}. \tag{3.7}$$

3.2.3 *Damage evolution function*

The creep damage evolution function is expressed in rate form. While some SSA damage models assume damage updates instantaneously with the stress field in a brittle manner (e.g. Sun et al., 2017), a rate form is consistent with laboratory experiments on ice (Duddu &Waisman, 2012). Moreover, the creep damage model can be tuned to capture the time-dependent propagation of rifts in ice shelves based on satellite observations, and has numerical advantages related to adaptive time-stepping and extending the damage model to nonlocal form (Section 3). In the Lagrangian framework, we express the material derivative of the second-order creep damage tensor as the Jaumann derivative (Pralong & Funk, 2005)

$$\dot{\mathbf{D}} = \frac{\partial \mathbf{D}}{\partial \mathrm{t}} = \mathbf{f} + \mathbf{WD} - \mathbf{DW}\,, \tag{3.8}$$

where t is time, $\mathbf{W}$ is the spin tensor $W_{ij} = \frac{1}{2}\left(\frac{\partial v_i}{\partial x_j} - \frac{\partial v_j}{\partial x_i}\right)$, and $\mathbf{f}$ is the dynamic damage evolution function as (Murakami, 1988)

$$\mathbf{f} = B^*\langle\langle \chi - \sigma_{\mathrm{th}} \rangle\rangle^r \left\{ \mathrm{Tr}\left[(\mathbf{I} - \mathbf{D})^{-1} \cdot \left(\boldsymbol{\nu}^{(1)} \otimes \boldsymbol{\nu}^{(1)} \right) \right] \right\}^k \left[(1-\gamma)\mathbf{I} + \gamma \boldsymbol{\nu}^{(1)} \otimes \boldsymbol{\nu}^{(1)} \right], \tag{3.9}$$

$$\chi = \alpha \langle \tilde{\sigma}_1 \rangle + \beta \sqrt{3\mathbf{II}_{\tilde{\boldsymbol{\sigma}}^{\mathrm{D}}}} + (1 - \alpha - \beta)\mathbf{I}_{\tilde{\boldsymbol{\sigma}}}\,. \tag{3.10}$$

In (3.9), B^*, r, k are creep damage parameters (listed in Table 3-1) and χ is the Hayhurst stress, which is an equivalent stress measure defined in (3.10) (Hayhurst, 1972). The Hayhurst stress is a weighted combination of the maximum effective principal stress (weighted by α), the effective von Mises stress (weighted by β), and the effective hydrostatic stress (weighted by $\lambda = 1 - \alpha - \beta$). The terms $\mathbf{I}_{\tilde{\boldsymbol{\sigma}}}$ and $\mathbf{II}_{\tilde{\boldsymbol{\sigma}}^{\mathrm{D}}}$ denote the first invariant of the effective Cauchy stress and the second invariant of the effective deviatoric stress, respectively. The Hayhurst weights must fulfill

$$0 \le \alpha, \beta, \lambda \le 1\,, \tag{3.11}$$

which we take as $\alpha = 0.21$, $\beta = 0.63$, and $\lambda = 0.16$ as previously calibrated from laboratory data (Pralong and Funk, 2005). The first term in (3.9) determines the damage evolution rate based on the Hayhurst criterion and σ_{th}, an assumed stress threshold that restricts damage evolution to where $\chi > \sigma_{\mathrm{th}}$. The Macaulay brackets $\langle\langle \cdot \rangle\rangle$ are defined as

$$\langle\langle x \rangle\rangle = \begin{cases} x, & \text{if } x \ge 0 \\ 0, & \text{if } x < 0 \end{cases}. \tag{3.12}$$

In the second and third terms of (3.9), $\boldsymbol{\nu}^{(1)}$ is the eigenvector corresponding to the maximum effective principal stress, $\langle \tilde{\sigma}_1 \rangle$, which we always assume lies within the horizontal $x_1 - x_2$ plane to be consistent with crevasse formation along vertical planes. Operator $\mathrm{Tr}[\cdot]$ denotes the trace.

Parameter k has been calibrated based on laboratory experimental data to be a function of the Cauchy stress (e.g. Pralong & Funk, 2005; Duddu & Waisman, 2012), but we set it to a constant here for simplicity. The second term of (3.9) accounts for the increase in the damage rate at a spatial location based on any pre-existing damage on the principal plane normal to the $\mathbf{v}^{(1)}$ direction. The third term sets the level of anisotropy in damage accumulation according to the anisotropy weighting parameter γ, which can be set between zero (purely isotropic with damage accumulating on all principal planes equally) and one (purely anisotropic with damage accumulating only on the principal plane normal to the $\mathbf{v}^{(1)}$ direction). If $\mathbf{D}$ and $\widetilde{\boldsymbol{\sigma}}$ are always coaxial, the relationship between the principal components of the damage rate is controlled by the anisotropy parameter as

$$\langle \dot{D}_2 \rangle = \langle \dot{D}_3 \rangle = (1-\gamma)\langle \dot{D}_1 \rangle \,. \tag{3.13}$$

Any misalignment between $\mathbf{D}$ and $\widetilde{\boldsymbol{\sigma}}$ will cause damage accumulation to become more weighted towards $\langle D_2 \rangle$ at the expense of $\langle D_1 \rangle$. Misalignment can occur, for example, as a rift develops and causes the orientations of principal stresses to change downstream. Note that in the case of full anisotropy (γ=1), Equation (3.9) will never produce damage on $\langle D_3 \rangle$, because we always assume the maximum effective principal stress lies within the horizontal $x_1 - x_2$ plane. We test sensitivity to γ in Section 3.4.2.

3.2.4 *Parameterization of creep damage for the SSA*

While the SSA is 2-D, creep damage evolution requires the evaluation of the full Cauchy stress tensor in 3-D. Damage can then be vertically averaged for incorporation into the next SSA solution step (Section 3.3.3). The 3-D deviatoric stress tensor from the 2-D velocity field defined

by the SSA with damage can be obtained at vertical coordinate z using the nonlinearly viscous constitutive relation for ice flow (Glen, 1955)

$$\boldsymbol{\sigma}^{\mathbf{D}}(z) = 2\eta(\dot{\varepsilon}_e)\tilde{\boldsymbol{\varepsilon}}(z)\,, \tag{3.14}$$

where $\tilde{\boldsymbol{\varepsilon}}$ is determined according to (3.7) using the 2-D strain-rates from the SSA solution and the local 3-D damage. Subtracting the pressure, p, from the deviatoric stresses yields the needed Cauchy stresses ($\sigma_{ij} = \sigma_{ij}^{\mathrm{D}} - p_{\mathrm{i}}\delta_{ij}$), but pressure is unknown in the SSA. Keller and Hutter (2014) therefore proposed parameterizing an effective pressure, given as

$$p_{\mathrm{eff}} = p_{\mathrm{i}} - p_{\mathrm{w}}\,, \tag{3.15}$$

where p_{i} is the ice pressure according to the hydrostatic approximation

$$p_{\mathrm{i}}(z) = \rho g(s - z) - \sigma_{11}^{\mathrm{D}}(z) - \sigma_{22}^{\mathrm{D}}(z)\,, \tag{3.16}$$

and p_{w} is the basal water pressure

$$p_{\mathrm{w}}(z) = \begin{cases} 0, & \text{if } z \geq z_{\mathrm{sl}} \\ \rho_{\mathrm{w}} g(z_{\mathrm{sl}} - z), & \text{if } z < z_{\mathrm{sl}} \end{cases}, \tag{3.17}$$

where z_{sl} is sea level elevation, which we set to zero. Furthermore, these authors proposed that pressure should be unaffected by damage, with the justification that volumetric effects oppose crack formation because they are largely dominated by the compressive ice overburden. Consequently, the effective stress is calculated as $\tilde{\sigma}_{ij} = \tilde{\sigma}_{ij}^{\mathrm{D}} - p_{\mathrm{eff}}\delta_{ij}$ rather than as given in Equation (3.5), and the Hayhurst criterion (3.10) is re-expressed as

$$\chi_{\mathrm{SSA}} = \alpha(\langle\tilde{\sigma}_1^{\mathrm{D}}\rangle - p_{\mathrm{eff}}) + \beta\sqrt{3\mathbf{II}_{\tilde{\boldsymbol{\sigma}}^D}} + \lambda(-3p_{\mathrm{eff}})\,. \tag{3.18}$$

We test this scheme as given, but acknowledge that improvements to this parameterization are possible, especially regarding the basal water pressure term in (3.17). This term is overly

simplistic for grounded ice; for example, Equation (3.17) assumes basal water pressure is zero for ice grounded above sea level, which may not be true in all cases. However, our focus here is largely on shelf ice, so we implement the parameterization as given. We also note that within a full-Stokes setting, water pressure has been incorporated into damaged ice using a poromechanics approach (Mobasher, et al., 2016; Duddu et al., 2020). A similar approach could potentially be adapted for the SSA parameterization.

3.3 Implementation

We start this section by discussing the GIMPM-SSA framework, including how damage is implemented within it and its advantages concerning accuracy and efficiency of the ice flow and damage solutions. We then present the solution for the local 3-D damage increment, and explain how it can be used to set an adaptive time step and diffused over a characteristic length scale to calculate a nonlocal damage increment. Furthermore, we describe a brittle rupture criterion, the depth-averaging of the 3-D damage field, and our current treatment of fully-damaged material points (rifts). Lastly, we detail incorporation of the depth-averaged damage variable into the SSA solution.

3.3.1 *Generalized interpolation material point method (GIMPM)*

If using mesh-based numerical methods, then artificial diffusion errors may arise during advection of the damage variable, which smear sharp edges and makes critical features such as rifts difficult to capture. This diffusion is inherent to purely Eulerian advection schemes, where the mesh is not moved with the computed velocity field, and can also arise when working in a Lagrangian frame (moving-mesh) due to frequent remeshing that may be required when

modeling large-deformation materials like large-scale ice flow. While our creep damage model may be adopted for any flow-modeling framework, we implement it here within our GIMPM-SSA code to avoid these diffusion errors (Chapter 2). The GIMPM (Bardenhagen & Kober, 2004) is one of several material point methods, which all share the same basic procedure. In the GIMPM, a set of material points (or particles) provides a Lagrangian description of the material domain and holds all dynamic variables. The momentum equations are solved on a background grid in a similar manner to the finite element method, but with the material points serving as moving integration points. The grid solution is then used to update material point quantities such as position, velocity, and area, as well as material point history variables. Here, the history variables are ice thickness and damage. These updates are performed in a Lagrangian frame, which ensures that all fields advect without diffusion errors and enables tracking of the ice front and grounding line at sub-grid accuracy. The primary difference between the various material point methods concerns the shape functions used to map between material points and the grid. The most accurate variants use C^1 continuous shape functions to ensure smooth transfers of stiffness as material points move between grid cells, and in the GIMPM, such shape functions are assembled by convolving linear grid functions with characteristic functions associated with each material point.

Within the GIMPM-SSA framework, we track damage and any other 3-D fields, such as temperature, upon a series of vertical layers assigned to each material point. For mesh-based methods, the vertical layers could be assigned to nodes or quadrature points instead. For the simulations in this chapter, we always maintain an even distribution of layers between the local ice base and surface elevations, which is possible because we do not incorporate mass balance processes such as surface and basal melt, or infill of crevasses with snow at the surface or marine

ice at the base. Furthermore, we do not account for necking processes (Bassis & Ma, 2015), and do not implement healing because the simulations here are largely tensile, though healing models have been proposed (Pralong & Funk, 2005; Pralong et al., 2006). Modifying the creep damage model to account for the impacts of mass balance, necking, and healing is beyond the scope of this chapter. However, in Section 3.4.4, we test a damage model for comparison that does account for some of these processes (Bassis & Ma, 2015), and we discuss the potential for a combined approach between the models in Section 3.5.

3.3.2 *Local 3-D damage increment*

The 3-D damage updates take the form

$$\mathbf{D}^{m+1} = \mathbf{D}^{m} + \Delta\mathbf{D}^{m}\,, \tag{3.19}$$

where $\Delta\mathbf{D}^{m}$ is the damage increment over a time step and may be expressed in local or nonlocal form. For each material point layer, the local damage increment, ${}^{\mathrm{loc}}\Delta\mathbf{D}^{m}$, is found by integrating the damage evolution rate, $\dot{\mathbf{D}}^{m}$**,** over the length of the time step Δt using the Runge-Kutta-Merson (RKM) method as detailed in Zolochevsky et al., 2009 and Ling et al., 2000. The RKM update allows higher accuracy and larger time steps than a forward Euler update. During the RKM scheme, an internal damage variable is continuously updated over a series of sub-steps, whose sizes are optimized for speed and accuracy. The strain-rate determined from the preceding SSA solution is unchanged during the RKM update. The damage rate is calculated by solving Equations (3.7),(3.14),(3.6),(3.16),(3.17),(3.15),(3.9),(3.10), and (3.8). At completion, the RKM routine returns the local damage, ${}^{\mathrm{loc}}\mathbf{D}^{m+1}$, from which ${}^{\mathrm{loc}}\Delta\mathbf{D}^{m}$ can be calculated as ${}^{\mathrm{loc}}\Delta\mathbf{D}^{m} = {}^{\mathrm{loc}}\mathbf{D}^{m+1} - \mathbf{D}^{m}$.

We stop damage accumulation on a layer once the maximum principal damage component reaches $D_{\max}$, though further evolution via the spin terms in (3.8) is allowed. A damage component that reaches $D_{\max}$ is considered ruptured, and can roughly be associated with the formation of macrocracks or crevasses, though we currently make no explicit assumptions concerning their width, spatial distribution, or potential influence on driving stress. However, our parameterization is probably most consistent with widely-spaced crevassing, given that we do not modify stresses at depth to account for stress shielding from damaged layers of neighboring material points. Stopping damage accumulation once $\langle D_1 \rangle = D_{\max}$ is a requirement of the current formulation of the damage model, which does not currently account for multi-axial damage accumulation after rupture. Therefore, our model does not currently allow development of cross-cutting crevasses, though we estimate their occurrence and influence on flow is typically minimal for ice shelves. However, multi-axial damage accumulation before rupture, which may occur under biaxial tension, could possibly be accounted for by modifying the anisotropy parameter according to the relative magnitude of the two tensile principal effective stresses (Ganczarski & Skryzypek, 2001). This multi-axial modification has yet to be verified for ice, and has minimal impact on the experiments presented here. Therefore, we present the results that did not use this modification.

We split the above solution for the 3-D damage increments into 2 loops over the layers of a material point. The first loop is run from the bottom layer towards the top layer, and is exited if a layer is encountered with ${}^{\mathrm{loc}}\boldsymbol{\Delta}\mathbf{D}^m = 0$ and $\mathbf{D}^m = 0$ for all components. If the first loop does not process all layers, a second loop from the surface towards the base is initiated with the same exit criterion. During the second loop, we assume damage is associated with surface crevassing and ignore the sea water pressure term in the effective pressure. A surface meltwater pressure term

could be added, instead. This two-loop scheme assumes cracks will not initiate in the middle of the shelf, and consequently, we achieve a faster solution by avoiding processing layers that will remain undamaged.

3.3.3 *Adaptive time stepping*

The maximum change in vertically-averaged local damage, $\overline{\mathrm{dD}}_{\max}$, of all material points is used to adjust the time step as needed for both the current and next computational cycle, with the goal of limiting the amount of damage allowed to accumulate each cycle to ensure accuracy, stability, and efficiency. Because the damage update can affect the current time step, it must begin each computational cycle. We define $\overline{\mathrm{dD}}_{\max}$ as

$$\overline{\mathrm{dD}}_{\max} = \max\left(\langle {}^{\mathrm{loc}}\overline{\mathbf{D}}^{m+1} \rangle - \langle \overline{\mathbf{D}}^{m} \rangle \right), \tag{3.20}$$

where 'max' on the right hand side indicates the maximum value of all principal components, and vertical averaging of the damage variables takes the form

$$\overline{\boldsymbol{D}} = \frac{\int_b^s \boldsymbol{D}(z) B(z, T^*) dz}{H \int_b^s B(z, T^*) dz}, \tag{3.21}$$

where T^* is temperature, on which the 3-D flow-rate factor, $B(z, T^*)$, is dependent. The integrals are evaluated using the trapezoid rule. Note that since $B(z, T^*)$ can vary with depth, it must be included in (3.21) alongside $\boldsymbol{D}(z)$ to properly capture the combined effect of damage and thermal softening on the depth-averaged viscosity of ice (Keller & Hutter, 2014).

If $\overline{\mathrm{dD}}_{\max} \geq 0.075$, we decrease the current time step as $\Delta t^m = \Delta t^m / 1.5$ and recalculate the local damage increments. This situation rarely occurs, but serves as a safeguard against rapidly increasing damage. If $\overline{\mathrm{dD}}_{max} < 0.075$, the time step for the next computational cycle is

set as $\Delta t^{m+1} = \min\left(\delta_1 \Delta t^m\ ,\ \frac{\delta_2 \Delta t^m}{\overline{\mathrm{dD}}_{\max}}, \mathrm{CFL}\right)$, where we take $\delta_1 = 1.8$ and a δ_2 of 0.05 (Ling et al., 2000), and $\mathrm{CFL} = \delta_3 / \max\left(\left|\frac{v_1}{\Delta x_1}\right| + \left|\frac{v_2}{\Delta x_2}\right|\right)$ indicates the maximum timestep that satisfies the Courant-Friedrichs-Lewy condition with constant $\delta_3 \leq 1$. Here, the time step is almost always restricted by damage rather than the CFL condition, and consequently, $\overline{\mathrm{dD}}_{\max} \approx \delta_2$ each computational cycle. The typical time increment varies based on the chosen damage parameters, but in all the simulations in this chapter, it is on the order of days for sub-critical damage accumulation to hours during rapid rift propagation.

3.3.4 *Nonlocal 3-D damage increment*

Implementing nonlocal damage is motivated by both physical and numerical considerations. Physically, the progressive accumulation of microcracks that damage mechanics describes is distributed over a characteristic length scale in quasi-brittle materials like glacier ice (Bazant, 1986; Hall & Hayhurst, 1991). Numerically, local damage models suffer from directional mesh bias and mesh size sensitivity as damage localizes to single elements. We implement a nonlocal integral scheme (Duddu & Waisman, 2013), which diffuses the local damage increment between neighboring material points over the characteristic length scale. Note the difference between this intentional diffusion and the artificial diffusion that may arise using mesh-based advection schemes: the nonlocal damage diffusion is physically-based on observations of fracture in quasi-brittle materials, whereas artificial diffusion is a numerical error causes ice to lose damage unphysically over time.

Here, we apply the nonlocal scheme within each layer of neighboring material points. For example, local damage of the second layer of a material point is only reweighted according to the

local damage of the second layer from surrounding material points, but not the layer above or below it. The nonlocal damage increment, $\Delta\mathbf{D}^m(\boldsymbol{x}^m)$, is calculated as

$$\Delta\mathbf{D}^m(\boldsymbol{x}^m) = \frac{\sum_{j=1}^{N} \phi\left(\boldsymbol{x}^m - \widehat{\boldsymbol{x}}_j{}^m\right)\, {}^{\text{loc}}\boldsymbol{\Delta D}^m\left(\widehat{\boldsymbol{x}}_j{}^m\right)}{\sum_{j=1}^{N} \phi\left(\boldsymbol{x}^m - \widehat{\boldsymbol{x}}_j{}^m\right)}, \tag{3.22}$$

where N is the number of material points, $\widehat{\boldsymbol{x}}_j{}^m$, positioned within a characteristic length, l_c, of $\boldsymbol{x}^m$ at timestep m. The weight function, ϕ is a Gaussian curve given as

$$\phi\left(\boldsymbol{x}^m - \widehat{\boldsymbol{x}}_j{}^m\right) = \exp\left(-\left(\frac{\kappa\left\|\boldsymbol{x}^m - \widehat{\boldsymbol{x}}_j{}^m\right\|}{l_c}\right)^2\right), \tag{3.23}$$

where constant κ controls the rate of decay of the weight function. We use $\kappa = 2$. The nonlocal length, l_c, should reflect the size of the fracture process zone and should be set so that the number of neighboring material points, j, is large enough to alleviate grid dependence (Duddu & Waisman, 2013). We note that as an alternative to the nonlocal integral scheme presented here, an implicit-gradient nonlocal scheme could be implemented, instead (Jimenez et al., 2017). However, the gradient approach requires solving an equation on the mesh for each layer, and is therefore more computationally expensive.

3.3.5 *3-D damage update*

On each material point layer, the 3-D damage tensor is updated from the damage increment according to (3.19). Afterwards, a brittle rupture or failure criterion is enforced, where if the principal value $\langle D_1^{m+1}\rangle$ for a layer reaches a specified critical damage, D_{cr}, then it set to $D_{\max}$. The other two principal values $\langle D_2^{m+1}\rangle$ and $\langle D_3^{m+1}\rangle$ are also updated in a similar manner to

Equation (3.13) as $\langle D_2^{m+1} \rangle = \langle D_3^{m+1} \rangle = (1-\gamma)\langle D_{\max} \rangle$, unless this update reduces their values. Previously, published values of D_{cr} for ice range from $D_{\mathrm{cr}} = 0.45$ (Duddu & Waisman, 2012) to 0.6 (Duddu & Waisman, 2013), and we set D_{cr} to 0.6 throughout this chapter. Note that not all damage tensors on all layers of a material point are guaranteed to have the same orientation. Misalignments with depth can occur as damage initiates at different times and accumulates under varying stress fields over time. However, misalignment is minimal in the simulations presented here.

3.3.6 *2-D damage update and rift treatment*

After the 3-D damage update, the vertically-averaged damage that will be implemented into the SSA, $\overline{\mathbf{D}}^{m+1}$, is calculated according to (3.21). As was done for 3-D damage, a 2-D brittle rupture condition can be set by defining a vertically-averaged critical damage, $\overline{D}_{\mathrm{cr}}$, and maximum damage, $\overline{D}_{\max}$. However, upon brittle rupture in 2-D, we set all components of $\overline{\boldsymbol{D}}$ to $\overline{D}_{\max}$ rather than only the maximum principal component as in the 3-D case. This 2-D treatment is consistent with complete failure of the material point, or the formation of a rift. Larger values of $\overline{D}_{\max}$ are associated with a faster rate of rift widening and greater downstream velocities, and we find values for $\overline{D}_{\max}$ of approximately 0.85—0.9 produce well-controlled and distinct rifts for the simulations presented here. Physically, setting a value of $\overline{D}_{\max}$ less than unity can be interpreted as allowing some residual strength between the flanks of the rift, which can occur when rifts contain ice mélange that is structurally coherent enough to transmit stresses (Rignot & MacAyeal, 1998; Larour et al., 2004; Borstad et al., 2013). A complete description of rift forces should include a boundary condition on the rift flank walls similar to at the ice front (3.4), but which can also account for the pressure of ice mélange (Larour et al., 2014). This boundary

condition acts to oppose rift opening. For simplicity, we do not explicitly implement such a boundary condition here; rather, its effect on the rift opening rate is implicitly accounted for by setting the value of $\overline{D}_{\max}$ lower than unity. We discuss the potential for implementing more complex rift dynamics, including a rift wall boundary scheme, within the damage and GIMPM-SSA framework in Section 3.5. We also test such a scheme in Chapter 4.

3.3.7 *SSA solution and material point updates*

Damage is incorporated into the SSA solution by replacing $\dot{\boldsymbol{\varepsilon}}$ in (3.2) with $\widetilde{\dot{\boldsymbol{\varepsilon}}}$, which is calculated from (3.7) using $\overline{\mathbf{D}}$ as the damage variable. This substitution modifies the original SSA-GIMPM discretization (see Chapter 2), yielding the following element sub-matrices of the tangent matrix, **K**, that are computed by summing over material points:

$$
\begin{aligned}
\mathrm{K}_{11IJ} :=& \sum_{p=1}^{n_p} A_p \bar{\eta}_p H_p \left\{ \frac{\partial S_{Jp}}{\partial x_1} \left[2 \frac{\partial \phi_{Ip}}{\partial x_1} (2 - D_{11} - D_{33}) - \frac{\partial \phi_{Ip}}{\partial x_2} D_{12} \right] \right. \\
&\left. + \frac{\partial S_{Jp}}{\partial x_2} \left[\frac{1}{2} \frac{\partial \phi_{Ip}}{\partial x_2} (2 - D_{11} - D_{22}) - \frac{\partial \phi_{Ip}}{\partial x_1} D_{12} \right] \right\} + \sum_{p=1}^{n_p} A_p \hat{\beta}_p \phi_{Ip} S_{Jp}\,, \\
\mathrm{K}_{22IJ} :=& \sum_{p=1}^{n_p} A_p \bar{\eta}_p H_p \left\{ \frac{\partial S_{Jp}}{\partial x_2} \left[2 \frac{\partial \phi_{Ip}}{\partial x_2} (2 - D_{11} - D_{33}) - \frac{\partial \phi_{Ip}}{\partial x_1} D_{12} \right] \right. \\
&\left. + \frac{\partial S_{Jp}}{\partial x_1} \left[\frac{1}{2} \frac{\partial \phi_{Ip}}{\partial x_1} (2 - D_{11} - D_{22}) - \frac{\partial \phi_{Ip}}{\partial x_2} D_{12} \right] \right\} + \sum_{p=1}^{n_p} A_p \hat{\beta}_p \phi_{Ip} S_{Jp}\,, \\
\mathrm{K}_{12IJ} :=& \sum_{p=1}^{n_p} A_p \bar{\eta}_p H_p \left\{ \frac{\partial S_{Jp}}{\partial x_1} \left[2 \frac{\partial \phi_{Ip}}{\partial x_2} (1 - D_{33}) - \frac{\partial \phi_{Ip}}{\partial x_1} D_{12} \right] \right. \\
&\left. + \frac{\partial S_{Jp}}{\partial x_2} \left[\frac{1}{2} \frac{\partial \phi_{Ip}}{\partial x_1} (2 - D_{11} - D_{22}) - \frac{\partial \phi_{Ip}}{\partial x_2} D_{12} \right] \right\}, \\
\mathrm{K}_{21IJ} :=& \sum_{p=1}^{n_p} A_p \bar{\eta}_p H_p \left\{ \frac{\partial S_{Jp}}{\partial x_2} \left[2 \frac{\partial \phi_{Ip}}{\partial x_1} (1 - D_{33}) - \frac{\partial \phi_{Ip}}{\partial x_2} D_{12} \right] \right. \\
&\left. + \frac{\partial S_{Jp}}{\partial x_1} \left[\frac{1}{2} \frac{\partial \phi_{Ip}}{\partial x_2} (2 - D_{11} - D_{22}) - \frac{\partial \phi_{Ip}}{\partial x_1} D_{12} \right] \right\},
\end{aligned}
\tag{3.24}
$$

In (3.24), material point parameters are indicated with the subscript p, where A_p is the material point area, $\hat{\beta}_p$ is the friction parameter, and n_p is the number of material points in the element. Nodal indices are indicated with I and J. We adopt the same shorthand from Chapter 2 to notate the evaluation of the linear (ϕ_{Ip}) and GIMPM (S_{Jp}) shape functions at a material point, where $\phi_{Ip} = \phi_I(\boldsymbol{x}_p)$ and $S_{Jp} = S_J(\boldsymbol{x}_p)$. After the SSA is solved, the computational cycle for the GIMPM then continues as described in Chapter 2, where the grid solution is used to update material point velocity, 2-D position, areal domain, and thickness. We use the algorithm XPIC(k) (eXtended Particle In Cell of order k) to perform the velocity and position updates, an algorithm that eliminates potential noise or overdamping associated with simpler update schemes

(Hammerquist & Nairn, 2017). In agreement with a previous damage study (Nairn et al., 2017), we find that taking $k = 5$ yields sharp and stable crack propagation. Because each layer of a material point has the same horizontal velocity, updating the 2-D position of the material points automatically accounts for advection of any 3-D field, such as damage. Therefore, 3-D advection is essentially computationally free in the GIMPM-SSA framework. Conversely, using mesh-based Eulerian methods for advection would require solving a 2-D equation for each layer, or a single 3-D equation for the whole system. These Eulerian approaches would be much more expensive than the GIMPM-SSA framework, especially given our use of a tensorial damage variable; in addition, Eulerian advection schemes would suffer from artificial numerical diffusion.

3.4 Idealized test case: MISMIP+

We carry out three experiments to test the SSA creep damage model under different tunings and compare its performance to previously-published SSA damage models. We begin each experiment from the undamaged steady state configuration from the Marine Ice Sheet Model Intercomparison Project (MISMIP+, Asay-Davis et al., 2016), and allow damage and ice flow to evolve over time. In Section 3.4.1, we describe the MISMIP+ model setup. In Section 3.4.2, we show how the creep damage model can initiate a realistic damage field, which subsequently evolves to propagate rifts resulting in tabular calving. We perform sensitivity tests for the anisotropy parameter, mesh resolution, the nonlocal length scale, and the impact of an isothermal versus linear temperature profile. The creep damage model ultimately captures physically-consistent and numerically-stable rifting that previous crevasse-tracking SSA damage approaches are not well suited for replicating. For comparison, we test a crevasse-tracking

damage model (Sun et al., 2017) in Section 3.4.3. where crevasse depths are calculated using the "zero-stress" criterion (Nye, 1957). We conduct further tests with the zero-stress damage model in Section 3.4.4, but where we modify the model to also account for the effects on damage from necking and mass balance (Bassis & Ma, 2015).

3.4.1 *MISMIP+*

The MISMIP+ geometry is rectangular. In the longitudinal direction, the domain spans from an ice divide at $x_1 = 0$ km to an ice front at $x_1 = 640$ km. We do not allow the position of this ice front to evolve over time. The lateral boundaries span from $x_2 = 0$ km to $x_2 = 80$ km, and the entire system has a plane of symmetry about $x_2 = 40$ km. Normal velocities are set to zero (i.e. zero inflow) at all boundaries except at the ice front, where the Neumann boundary condition (3.4) is applied. The bedrock topography is a U-shaped submarine trough. Detail of the steady-state grounding configuration is shown in the grey shading of Figure 3-1. At the most retreated section of the steady-state grounding line ($x_1 \sim 450$ km), the bed has a retrograde slope. The higher sidewalls of the bedrock trough result in thin protrusions of laterally grounded ice that define the maximum longitudinal extent of the grounding line at $x_1 \sim 537$ km. All floating ice upstream of this point constitutes a laterally-supported shelf ice, whereas all ice downstream constitutes an unsupported floating ice tongue. The trajectories overlaying Figure 3-1 correspond to the 2nd principal component of anisotropic damage at the first time step, which may be interpreted as the initial development of crevasse patterns, or the plane along which $\langle \overline{D}_1 \rangle$ accumulates.

Starting from a thin slab of ice defined over the domain, we grew the system to steady state using the given MISMIP+ ice flow parameters and accumulation rate and a modified

Coulomb law for friction (Schoof, 2005; Gagliardini et al., 2007; Leguy et al., 2014). For this spin-up procedure, we use the SSA and thickness evolution solvers in the finite element software Elmer/Ice (Gagliardini et al., 2013). Without the damage model, the GIMPM-SSA model can hold the grounding line at its steady-state position for at least 100 years if no melt rate is assigned, satisfying the MISMIP+ Ice0 control experiment (Chapter 2). Unless otherwise specified, we use a structured rectangular mesh/grid with a resolution of 0.5 km and initiate 9 regularly-spaced material points within each grid cell.

3.4.2 *SSA creep damage simulations*

We test our SSA creep damage model using the nonlocal integral formulation with the parameters given in Table 3-1, where α, β, and r, assume the values calibrated by Pralong and Funk (2005). We initially specify that the ice shelf is isothermal, so that the 3-D flow rate factor, B, does not vary with depth, and we set a stress threshold of $\sigma_{\mathrm{th}} = 0.12$ MPa. We set a nonlocal length scale of $l_{\mathrm{c}} = 1$ km, which roughly corresponds to the horizontal length of the fracture process zone, which we estimate from clusters of seismicity detected around a propagating rift on Amery Ice Shelf (Bassis et al., 2007). For our initial creep damage experiment, we test three different levels of damage anisotropy: $\gamma = 0$, $\gamma = 0.5$, and $\gamma = 1$, which correspond to fully isotropic, evenly mixed isotropic/anisotropic, and fully anisotropic damage, respectively. Each simulation eventually results in tabular calving, at which point we end the simulation. We report results for the 2-D vertically-integrated maximum principal damage.

Initial damage accumulation: For all simulations, damage accumulation is minimal for interior grounded ice, where velocities and stresses are low due to basal friction. Downstream portions of

the ice tongue also accumulate minimal damage, as strain-rates and stresses are low. Therefore, we only report results near the grounding line, where damage is greatest. Figure 3-2 shows the early evolution of the principal damage field $\langle \overline{D}_1 \rangle$ for the fully anisotropic case at (a) 0.06 years and (b) 0.2 years. At 0.06 years, relatively strong damage accumulates along the ice shelf margins as expected, where stresses are large. However, the dominant damage accumulation occurs at $x_1 \sim 520$ km, where rifts initiate from the lateral boundaries of domain as indicated where $\langle \overline{D}_1 \rangle = \overline{D}_{max} = 0.9$. These rifts quickly propagate to the grounded lateral protrusions, where they are temporarily slowed. This rifting largely develops under strong uniaxial tension, and consequently, nearly identical damage patterns develop at similar rates for all values of γ tested (see Supplementary Figures B-1a and B-2a for the isotropic and mixed isotropic/anisotropic cases, respectively). Note that the lateral boundaries of the domain ($x_2 = 0$ km and $x_2 = 80$ km) can be considered symmetry boundaries because the normal velocities are set to zero, so that the rifts can be considered to have initiated from the center of small ice shelves. While rifts typically initiate at grounded margins, rift initiation from the center of ice shelves has occurred, for example, at Pine Island Glacier (Jeong et al., 2016).

The configuration in Figure 3-2a is maintained until the grounded lateral protrusions weaken and thin enough to allow the rifts to propagate through ~0.1 years later, at which point these regions also unground. The rifts propagate upstream following the elevated damage that previously developed along the ice shelf margins, as shown in Figure 3-2b at 0.2 years. As in Figure 3-2a, rifts for the lower-anisotropy cases also propagate into a similar configuration, but now the rates of propagation are faster for lesser anisotropy. A comparable rift configuration develops in the fully-isotropic case by ~0.12 years and in the mixed isotropic/anisotropic case by ~0.18 years (Figures B-1b and B-2b).

Tabular calving: The rifting pattern in Figure 3-2b represents the final configuration before rifts propagate laterally across the domain to result in tabular calving. It is also the last configuration in which the spatial distribution of damage is similar for all values of γ. Figure 3-3 gives the final depth-averaged principal damage field $\langle \overline{D}_1 \rangle$ at calving. For the isotropic case (Figure 3-3a), the original rifts branch so that two points of calving occur; one branch originating from the upstream point of rifting reached in Figure B-1b, and the other originating from a downstream position lateral to where the rift initiated at $x_1 \sim 520$ km. This second branch also partially develops for the $\gamma = 0.5$ case. However, for both the mixed isotropic/anisotropic (Figure 3-3b) and fully-anisotropic (Figure 3-3c) cases, calving ultimately stems from the further upstream location.

Higher levels of anisotropy yield sharper and more arcuate rifts that are more characteristic of real ice shelves, and qualitatively, appear more "brittle" than results under lower anisotropy, which appear more "ductile". Higher anisotropy is also associated with slower rates of rift propagation, where the fully-anisotropic case calves after 0.486 years versus 0.165 years for the isotropic case. However, we emphasize that it is the anisotropy, not the speed of propagation, that allows the sharper rift and additional features to be captured. Rerunning the isotropic damage simulation with the damage rate factor B^* that is 4 times smaller allows isotropic damage to evolve at a similar rate to the anisotropic case, but the damage pattern remains essentially unchanged. Similarly, lowering δ_2 so that less damage accumulates each time step has negligible effect. Lastly, we note that our choice of $\overline{D}_{cr} = 0.8$ was arbitrary, and effectively eliminating the rupture criterion by setting $\overline{D}_{cr} = \overline{D}_{max}$ still allows the same rift patterns to develop, but with a smoother transition in damage between ruptured and unruptured ice (not shown). However, the jump in damage induced by setting $\overline{D}_{cr}$ lower than $\overline{D}_{max}$ yields

more visually-distinct rifting, and is likely physically justified because highly-damaged shelf ice may experience vertical shear stresses not accounted for in the SSA (Bassis & Ma, 2015) that could contribute to full-thickness brittle rupture.

Interestingly, the anisotropy strongly impacted rift behavior despite our simple scheme of representing rifts by setting all damage components of failed material points to $\overline{D}_{max}$. As the rift is represented by isotropic damage under our current treatment, it is the sub-critical damage that is controlling the rift path. The damage trajectories in Figure 3-1 show a clear arcuate pattern on the ice shelf that spans the lateral grounded margins, where the commonly observed pattern of en-échelon crevassing is reproduced. Rift propagation more closely follows these trajectories with higher levels of damage anisotropy.

Sensitivity to nonlocal damage length scale: The choice of the nonlocal length, l_c, is important in determining the computational cost of simulations, because a larger l_c allows larger element sizes to be used without grid bias. Ideally, l_c should be three or four times the element size to guarantee that mesh dependence is alleviated. However, using l_c = 1km, which is twice the element size, appears to be sufficient in the above simulations; doubling l_c to 2 km and rerunning the fully-anisotropic case yields a similar rift path and time to calving (Figure 3-4a) as the 1 km case (Figure 3-3c). To further confirm that grid dependence is alleviated, we rerun this l_c = 2 km fully-anisotropic case with 1 km grid resolution. Again, a similar rift path and time to calving is realized (Figure 3-4b). The largest difference between simulations using l_c = 2 km and l_c = 1 km is that the latter produces rifts that penetrate slightly further upstream, as indicated by the stars in Figure 3-4. The insensitivity of the model response to the exact value of l_c is encouraging given our crude estimate of the size of the fracture process zone, which could theoretically vary in

shape and size according to stress and damage. Alternative nonlocal integral formulations are available modify the nonlocal zone according to these variables (e.g. Giry, 2011), but the observed insensitivity to l_c likely obviates the need for these more complex nonlocal schemes.

Effect of temperature gradient: Our final test with the creep damage model highlights how vertically-varying temperature can influence damage evolution. In this test, we assign a linear vertical temperature profile for each material point, where the ice base temperature is set to -2°C, and the surface temperature is set to the value that yields the same depth-averaged rate factor, $\bar{B}$, from the isothermal case (approximately $-16.7\ ^{\circ}$C). To allow direct comparison with Figure 3-3c, we set l_c=1 km. The maximum principal damage field at calving corresponding to this temperature profile is given in Figure 3-5. Due to the warmer basal temperature, basal crevasses only propagate in the most stressed regions and the overall damage field is reduced outside of the rift. This reduced basal calving is likely more consistent with reality, where basal crevasses should only initiate from the center of the shelf under very high stresses. More commonly, flexural stresses, such as those experienced at the grounding line, are required to initiate basal crevasses (Logan et al., 2013), which we discuss further in Section 3.5. The ease with which temperature effects can be accounted for is an advantage of the GIMPM-SSA creep damage model. Conversely, the zero-stress model employed in the next two sets of experiments is formulated under the assumption of an isothermal ice shelf, and therefore always overestimates the spatial extent of basal crevassing.

3.4.3 *Zero-stress damage simulations*

The zero-stress criterion (Nye, 1957), states that closely-spaced field of crevasses propagate to depths where the net longitudinal maximum principal Cauchy stress becomes zero. A previous study defined a zero-stress damage variable as the ratio of the combined depths of surface and basal crevasses to the ice thickness (Sun et al., 2017). This previous study only considered isotropic damage, but here, we extend the zero-stress damage variable to anisotropic form as a 2nd order tensor, $\widehat{\boldsymbol{D}}$. We detail the anisotropic zero-stress damage model and its implementation in Appendix B.2. To summarize, the zero-stress model calculates 3-D stresses using a similar effective pressure as Equations (3.15)-(3.17) used in the creep damage model, and ignoring the water pressure term for surface crevasses. However, the zero-stress damage model is formulated in terms of *applied* stress and under the assumption that crevasses are closely-spaced and in equilibrium with the stress field, where deviatoric stresses are considered depth-invariant here. Conversely, the creep damage model is updated in rate form according to depth-varying *effective* deviatoric stresses and a parameterized pressure, both of which are sensitive to depth-varying temperature and damage. Put simply, the zero-stress model parameterizes crevasse depths only, while the creep damage function is a dynamic parameterization of the actual fracture process at each depth. A vertical damage profile for a column of ice according to the zero-stress model resembles a step function, with maximum damage at depths where crevasses have propagated and zero damage elsewhere. Conversely, a typical vertical profile using creep damage exhibits sub-critical damage accumulation, because creep damage parameterizes the progressive accumulation of microcracks.

Here, we test the zero-stress damage model on the MISMIP+ domain to demonstrate the impact of these differences in comparison to the creep damage results from Section 3.4.2. We

run two experiments with the zero-stress damage model, where each experiment tests the model in both fully-isotropic and fully-anisotropic form. Note that we ignore mass balance entirely for both ice flow and its influence on damage until Section 3.4.4 when we test the modification proposed by Bassis and Ma (2015).

In the first experiment, we run the zero-stress damage model as given for 30 years to show that the zero-stress assumptions alone are insufficient to initiate rifting. No critical rupture scheme is enforced. Note that in isotropic form, this test has been performed previously on a longer timescale using the MISMIP+ geometry with the finite volume ice flow model BISICLES (Sun et al., 2017). The isotropic zero-stress damage results near the grounding line are shown in Figure 3-6 at (a) 0 years, (b) 16 years, and (c) 30 years. At the first time step, damage immediately grows to $\widehat{D} \sim 0.33$ near the grounding line and $\widehat{D} \sim 0.5$ at the center of the ice shelf. With the exception of rifting, the zero-stress and creep damage models generally agree concerning the spatial distribution of heavily versus weakly damaged areas. As was the case for creep damage, grounded ice experiences relatively little damage, as the effective pressure is dominated by the contribution from ice overburden pressure. Nearly ruptured ice immediately develops between the narrow strip of grounded ice at approximately $x_1 \sim 520$ km and the lateral boundaries ($x_2 = 0$ and $x_2 = 80$ km). However, this region does not develop into a sharp rift that propagates across the shelf to result in a calving event. Over time, the zero-stress damage field mostly evolves from its initial configuration through advection, as evident following the black tracer particle in Figures 3-6a and 3-6b, which advects beyond the domain in Figure 3-6c. As expected, the damage field has a strong impact on the grounding line position (white dotted line) by decreasing buttressing to initiate grounding line retreat. This grounding line migration is reflected in the damage field, as ice that is nearing floatation quickly accumulates relatively

heavy damage in comparison to upstream grounded ice. The corresponding anisotropic zero-stress damage results are given in Figure 3-7, which yield lesser damage values everywhere compared to the isotropic case given that damage accumulation is restricted to a single plane. Like the isotropic case, damage evolution is largely dictated by advection, though relatively less advection occurs over the 30-year simulation, as indicated by the black tracer particle, because the lesser damage results in smaller velocities. While some material points eventually rupture by the end of the simulation, they do not result in tabular calving, even if the simulation is continued for several more decades. In agreement with Sun et al. (2017) none of the above zero-stress simulations resulted in calving. We can conclude that the novelties of our approach, namely using a tensorial damage variable and implementing the model within the GIMPM-SSA framework, are simply not enough to cause calving with the zero-stress model in the MISMIP+ experiment.

In the second zero-stress damage experiment, we rerun the MISMIP+ experiment, but encourage rifting to initiate by setting critical damage values of $\widehat{D}_{\mathrm{cr}} = 0.7$ and $\widehat{D}_{\mathrm{cr}} = 0.6$ for isotropic and anisotropic damage, respectively. The critical rupture criterion is enforced after each combined zero-stress damage and SSA solution. At the first time step, rupture occurs near the shear margins where $\langle \widehat{D}_1 \rangle > \widehat{D}_{\mathrm{cr}}$, and the resulting high stresses allow rifts to propagate across the domain to calve tabular icebergs. The final maximum principal zero-stress damage fields are given in Figures 3-8 and 3-9 for the isotropic and anisotropic cases, respectively. While both cases produce rifts in the same general area as the creep damage experiments, this experiment exposes several numerical and physical issues associated with zero-stress models that limit their general applicability for representing tabular calving. The primary numerical difficulty with this approach is that the zero-stress model is inherently a local damage model, and is

therefore subject to grid dependence. Figures 3-8a and 3-9a use a 0.5 km grid resolution whereas Figure 3-8b and 3-9b use a 1 km grid resolution. Grid dependence in the isotropic case is only slightly apparent in the spatial damage field, but has a strong influence on the time to calving; the 0.5 km resolution grid results in calving in 0.553 years versus 1.607 years for the 1 km resolution grid. Stronger grid dependence is observed in the spatial damage field for the anisotropic case. The differing grid resolution results in different rift paths, where damage clearly localizes to single grid cells, as shown in detail for the 1 km resolution case in Figure 3-9c.

In general, using the zero-stress damage model to simulate rift propagation is problematic due to the assumption that crevasse depths are in equilibrium with the stress field instead of using a rate-based parameterization of fracture as in the creep damage model. The rate-based parameterization allows more precise tuning of the rates of damage accumulation and rift propagation by varying the parameter B^* in the creep damage evolution function (3.9). Furthermore, creep damage will preferentially accumulate faster wherever the magnitudes of the Hayhurst stress, χ, and previous damage are greatest. Conversely, the zero-stress damage rate cannot be controlled, which was particularly problematic during the anisotropic critical rupture test, where calving occurred in under 6 hours for both grid resolutions. The corresponding timestep sizes were as small as fractions of a second in an attempt to keep $\overline{\mathrm{dD}}_{\mathrm{max}}$ less than 0.075 according to the time-stepping scheme, a restriction that was not always satisfied. In practice, such miniscule time steps are only sustainable for modeling nearly-instantaneous calving. Therefore, a lack of tuning controls can be added to the many issues associated with using zero-stress damage for Antarctic ice shelves, along with the potential physical-inconsistencies concerning assumptions on crevasse spacing and vertically-invariant deviatoric stresses, as well as grid-dependence due to the local damage formulation. Based on these studies, we conclude

that the zero-stress damage model is not well suited for parametrizing ice shelf fracture, except where crevasses are closely spaced and damage is small enough that localization and full-thickness rifting do not occur. Under the assumption that vertical temperature profiles are isothermal, the zero-stress model will typically overestimate basal crevasses. Furthermore, rifts are poorly represented in the zero-stress model, if they are initiated at all.

3.4.4 *Simulations using the modification for necking and mass balance*

A drawback of both the creep and zero-stress damage models as tested above is that they do not account for the potential impact that processes associated with necking and mass balance may have on damage evolution. In Appendix B.3, we explain how these processes influence crevasse depths, and we describe an expression that modifies large-scale damage to account for these processes (Bassis & Ma, 2015). In this section, we implement this expression within the zero-stress damage model, noting that implementation within the creep damage model is much more complex and is beyond the scope of this chapter. By comparing the results from this modified zero-stress damage model to those of the previous unmodified version, we can analyze how necking and mass balance processes impact damage. Thus, we can determine the settings in which our creep damage model is applicable in its current form without accounting for these processes, and then propose how a combined approach between damage models may be formulated for more generalized applications.

We perform two experiments with the modified zero-stress model. Both experiments resemble the first experiment from the previous section, where the damage model is activated and the MISMIP+ model is run forward in isotropic and anisotropic form for 30 years. For the first experiment, we set mass balance to zero, so that when the modified and unmodified zero-

stress damage results are compared, the role of necking processes alone are revealed. The results for the necking-only experiment are shown in Figures 3-10 and 3-11 for the isotropic and anisotropic cases, respectively. The first timestep is not shown because it is the same as the unmodified case (Figure 3-6a). Like the unmodified case, the necking model gives high values of damage near the margins, where the greatest damage is concentrated at $x_1 \sim 520$ km. These areas are associated with high stresses and $S_0 < 1$, so that necking accelerates the rate of damage accumulation, though rifts still do not propagate across the center of the shelf. However, the rifting in the modified isotropic case develops into much sharper patterns than in the unmodified isotropic case, which is not only due to the accelerated damage accumulation in these areas, but also due to healing in the immediate surrounding areas ($S_0 > 1$). Elevated damage values in these areas are also observable in the anisotropic modified case, relative to the anisotropic unmodified case. As predicted in Bassis and Ma (2015), the necking expression only yields additional damage accumulation along these areas of elevated shear, with healing dominating the response elsewhere. However, upon healing, most regions of the domain quickly re-damage towards their previous values. For example, the ice tongue part of the domain is largely under uniaxial tension, which in the isotropic case, yields the expected values of $\widehat{D} \approx 0.5$ and $S_0 \approx 2$. Any healing from the necking model is immediately countered by new zero-stress damage accumulation during the next computational cycle. However, at the location where the ice tongue in the unmodified case inherits heavy damage from upstream along the lateral bounds (Figure 3-6b and 3-6c), healing is observed in the modified case that is maintained over time (Figure 3-10). In the anisotropic case (Figure 3-11), sustained healing is more apparent along the shear margins of the ice shelf.

For the modified zero-stress second experiment, we test the impact of assigning a basal melt rate. We rerun the first experiment with a basal melting rate of 5 m a^{-1}, which is taken as constant throughout the floating ice domain, for simplicity. The isotropic and anisotropic results are given in Figures 3-12 and 3-13, respectively, and we note that setting a greater or lesser basal melting rate yields similar patterns. For the isotropic case, the damage field at 16 years (Figure 3-12a) is very similar to the necking-only case (Figure 3-10b) everywhere except near the lateral bounds of the floating domain, because basal melting is not strong enough to offset the effect of healing. The opposite affect occurs near the lateral bounds of the floating domain, and maximum damage is quickly realized. By the end of the simulation (Figure 3-12b), the ice shelf has thinned enough that melting begins to dominate over healing for more interior sections of the ice tongue. The same response is observed in the anisotropic case (Figure 3-13), except that at the interior sections of the ice tongue, melt-induced damage slightly overtakes healing earlier in the simulation than the isotropic case. Healing is this area is lower for the anisotropic case than the isotropic case, because damage, and therefore strain-rates, are lower.

3.5 Discussion

The experiments from Section 3.4.4 indicate that necking and mass balance may play significant roles in modulating damage on decadal timescales, so that these processes should be implemented within the creep damage model if it is to be applied on long timescales. Such an approach will be the subject of future research, and would require carefully modifying the 3-D damage field to reflect the modified value of vertically-integrated damage calculated according to necking and mass balance. This process could include adjusting the vertical coordinates and local damage values of each layer, as well as the addition or subtraction of layers. Based on our

previous comparison between creep damage and zero-stress damage, we would expect a combined creep-damage/necking model to behave somewhat differently than the combined zero-stress damage/necking model. While incorporating necking effects simply sharpened the zero-stress damage field in regions of elevated stress, this sharpened damage could develop into rifting with the creep damage model that would otherwise not occur. Similarly, targeted basal melting could also trigger additional rifting. However, we emphasize that necking and mass balance effect should not be always be necessary to initiate rifts. Encouragingly, the creep damage model can initiate realistic rifting without these additional effects (Section 3.4.2), though we acknowledge that given the idealized setting, it is difficult to determine whether or not this rifting should actually occur. Nevertheless, we show in Chapter 4 that the creep damage model can reproduce observed rifting on an actual ice shelf as well. Potentially, necking could play a more apparent role in small scale calving at the ice front; qualitatively, the configuration of fully-damaged material points in the isotropic modified zero stress simulation (Figure 3-10b) resembles the sawtooth pattern of calving sometimes observed at the lateral sides of long ice tongues (e.g. Erebus ice tongue).

The major advantage of combining the Bassis and Ma (2005) model with creep damage concerns healing. Basal crevasses are typically initiated near the grounding line or perturbations such as ice rises, and can heal heavily as they advect downstream, due to both necking and marine ice formation. Healing of upstream damage has been inferred, for example, on Larsen C Ice Shelf (Borstad et al., 2013). Healing in the modified zero-stress experiments was probably underestimated; most healing was immediately offset by new damage because the zero-stress model assumes crevasse depths are in equilibrium with the stress field, and zero-stress deviatoric stresses were assumed depth-invariant here so that basal crevassing was likely overestimated.

However, creep damage is rate-based and can incorporate 3-D temperature and stresses. As seen in Figure 3-5, when lower basal temperatures are accounted for, basal crevasses do not spontaneously propagate in low stress regions at the interior of the ice shelf. Therefore, when using a combined creep-damage/necking model with mass balance effects, damage associated with deep basal crevasses that were initiated from high stress regions upstream could become completely healed in low stress regions downstream. However, the success of capturing this behavior is reliant on proper initiation of the damage field corresponding to upstream basal crevasses. In the case that basal crevasses initiate from flexural stresses at the grounding line, special treatment is required to initiate the corresponding damage because such stresses are not captured in the SSA. The simplest approach may be to assign a 3-D damage distribution according to crevasse depths calculated with the SSA zero-stress approximation. However, this approach would be strictly a rough approximation, as for example, the zero-stress model was found to significantly underestimate basal crevasse depths near the grounding line on Larsen C Ice Shelf where flexural stresses are large (Luckman et al., 2012). These authors found better agreement with observations (within 10-20%) when using a linear elastic fracture mechanics approach, though this approach also did not explicitly account for flexural stresses and may not be accurate in all cases. An approach for approximating basal crevasse depth at the grounding line that does account for flexure involves using a thin elastic beam approximation, combined with a mode I brittle failure criterion (Logan et al., 2012), but this model is only applicable where strain rates are low. The most accurate way of capturing flexural stresses may be to transition to a full-Stokes model near the grounding line, though this approach is extremely computationally expensive in 3-D. Linear elastic fracture mechanics has been used to obtain

reasonable basal crevasse heights in a 2-D full-Stokes setting (Yu et al., 2017), or the creep damage model could potentially be applied.

One of the most significant advancements made with the creep damage framework presented here is in modeling the initiation and propagation of rifts using damage. While it is encouraging that our simple isotropic rift treatment cleanly propagates rifts, our ongoing research efforts are aimed at enabling a more accurate physical depiction of rift dynamics. Ideally, wide rifts that open into the ocean should be implemented as a discontinuity, with a Neumann boundary condition assigned along the flanks similar to the ice front boundary condition, but which also includes the opposing pressure of ice mélange within the rift (Larour et al., 2014). Using material point methods, this boundary condition could potentially be applied directly on material points in a similar manner to how water pressure has been incorporated into full-Stokes creep damage simulations (Duddu et al., 2020). Alternatively, it could be applied along line segments that are introduced to track cracks, and which can advect with flow (Nairn, 2003). Once a discontinuous boundary treatment is implemented, behavior of ruptured material points can be further modified to account for the strength of mélange between flanks, tension/compression asymmetry, and lateral friction or faulting between flanks.

3.6 Conclusion

Mechanical weakening and fracture of large-scale ice shelves may be modeled using an SSA parameterization for nonlocal, anisotropic creep damage. Unlike previous crevasse depth-tracking damage approaches, creep damage parameterizes the fracture process itself, and is therefore better suited for capturing dynamic processes such as rifting. Furthermore, creep damage is treated in 3-D, which allows damage interaction with other 3-D variables, such as

temperature and density. The numerical framework that we built to support the creep damage model is formulated on the material point method, which allows accurate and efficient advection of the 3-D damage field. In contrast, if the model was implemented within a traditional Eulerian framework, advection algorithms would be computationally inefficient, and introduce numerical diffusion error that would compromise the accuracy of damage evolution. By testing the creep damage model on an idealized marine ice sheet, we conclude that large scale damage of ice should be treated as highly anisotropic. Anisotropic creep damage yields sharper, more arcuate rifting and crevasse patterns that are more consistent with observations. In addition, anisotropic nonlocal damage is more thermodynamically consistent with the fracture physics (Pralong et al., 2006). Our experiments further show that deep crevassing, rifting, and tabular calving may occur using creep damage without the inclusion of necking or mass-balance processes. Testing a modified form of the zero-stress damage model that include these processes (Bassis & Ma, 2015) does not capture rifting that results in calving. Therefore, we conclude that the failure of zero-stress damage approaches to capture rifting does not occur due to the absence of these processes, but because the zero-stress model does not properly parameterize the fracture process and suffers from numerical issues related to its local formulation and assumption of equilibrium with the stress field. Future research should consider combining the necking/mass-balance and creep damage models for an ideal representation of ice-shelf fracture on decadal timescales. Ongoing research will also focus on verification of the damage parameters, application to real ice shelves, and improved representation of rifting.

Acknowledgements

Huth was funded by NASA Earth and Space Sciences fellowship under grant no. NNX15AN99H. Duddu gratefully acknowledges the funding support provided by the National Science Foundation's Office of Polar Programs via CAREER grant \#PLR-1847173. Smith was funded under the NASA grant no. NNX13AP69G.

Table 3-1. Parameters used in the creep damage experiments

Parameter	Value	Units
B^*	5.23×10^{-7}	$\mathrm{MPa}^{-r}\,\mathrm{s}^{-1}$
r	0.43	–
α	0.21	–
β	0.63	–
λ	0.16	–
k	4	–
σ_{th}	0.12	MPa
D_{cr}	0.6	–
D_{max}	0.99	–
$\overline{D}_{\mathrm{cr}}$	0.8	–

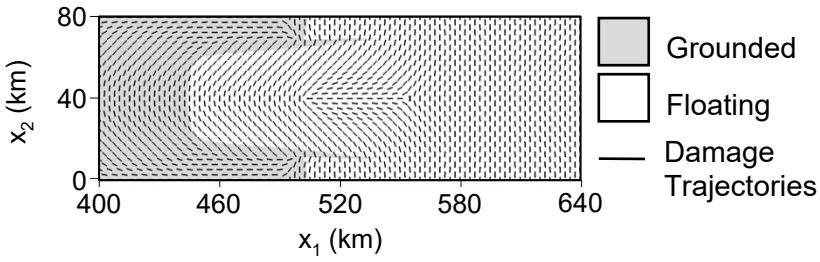

Figure 3-1. Initial grounding line configuration and damage trajectories

The MISMIP+ steady-state grounding line configuration and initial anisotropic damage trajectories. The trajectories correspond to the plane along which $\langle \overline{D}_1 \rangle$ accumulates, and can be interpreted as crevasse patterns.

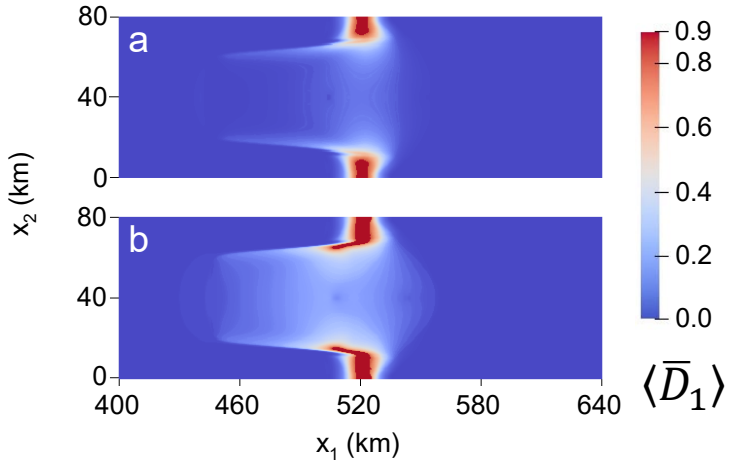

Figure 3-2. Initial damage accumulation for fully anisotropic creep damage

Maximum principal damage field for the fully anisotropic ($\gamma = 1$) creep damage simulation at **(a)** 0.06 years and **(b)** 0.2 years. Material points with $\langle \bar{D}_1 \rangle = \bar{D}_{\max} = 0.9$ correspond to rifts.

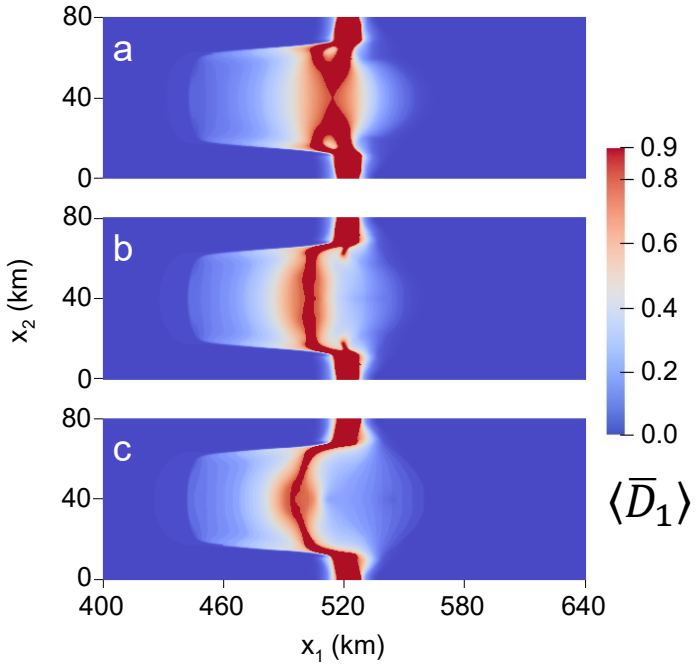

Figure 3-3. Damage field at calving for varying levels of creep damage anisotropy

Maximum principal creep damage field at calving for: **(a)** isotropic ($\gamma = 0$); **(b)** mixed isotropic-anisotropic ($\gamma = 0.5$); **(c)** fully anisotropic ($\gamma = 1$) damage. The corresponding times to calving are **(a)** 0.165 years; **(b)** 0.272 years; **(c)** 0.486 years.

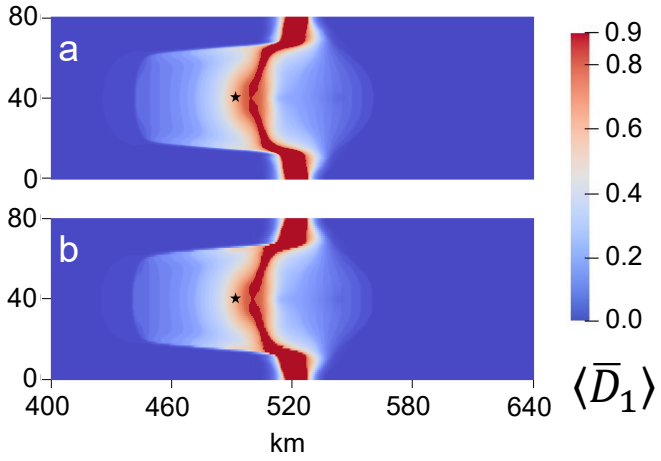

Figure 3-4. Alleviation of grid dependence using nonlocal creep damage

Maximum principal creep damage field at calving for fully anisotropic case ($\gamma = 1$) when using a nonlocal length scale l_c = 2 km and (**a)** 0.5 km versus **(b)** 1 km grid resolution. Alleviation of grid dependence is evident in the similarity of damage patterns between the two simulations, as well as the comparable times to calving of **(a)** 0.493 and **(b)** 0.510 years. These rift patterns and calving times are also similar to those in Figure 3-3c, which uses a 0.5 km grid and l_c = 1 km. The most apparent difference is that rifting in the the l_c = 1 km case penetrates slightly further upstream, as marked by the stars.

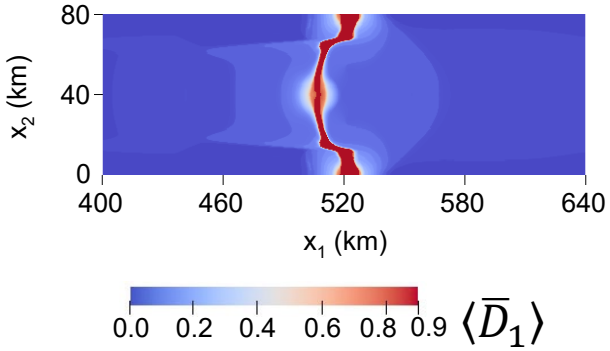

Figure 3-5. Anisotropic creep damage at calving with vertically-varying temperature

Maximum principal damage field at calving for fully anisotropic ($\gamma = 1$) creep damage when using the linear temperature profile and l_c = 1 km.

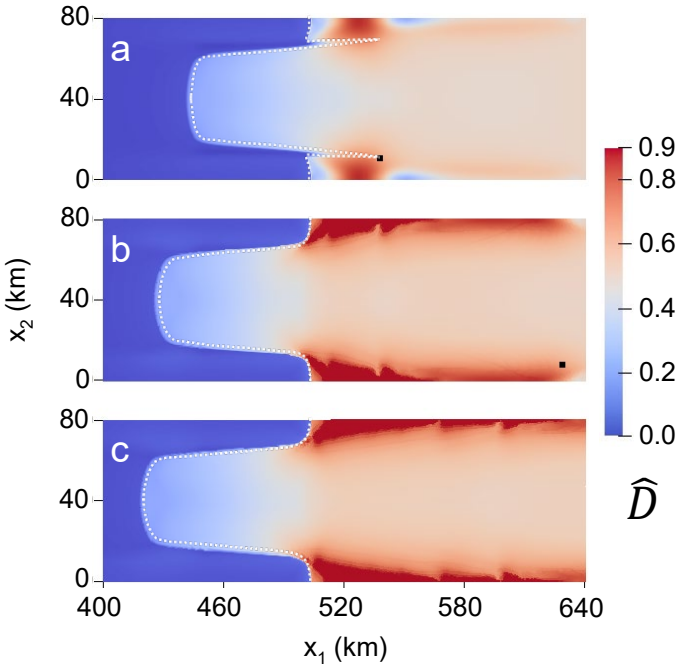

Figure 3-6. Isotropic zero-stress damage accumulation

Isotropic zero-stress damage field at **(a)** 0 years, **(b)** 16 years, and **(c)** 30 years. The black tracer particle highlights the highly-advective flow regime. The white dotted line indicates the grounding line.

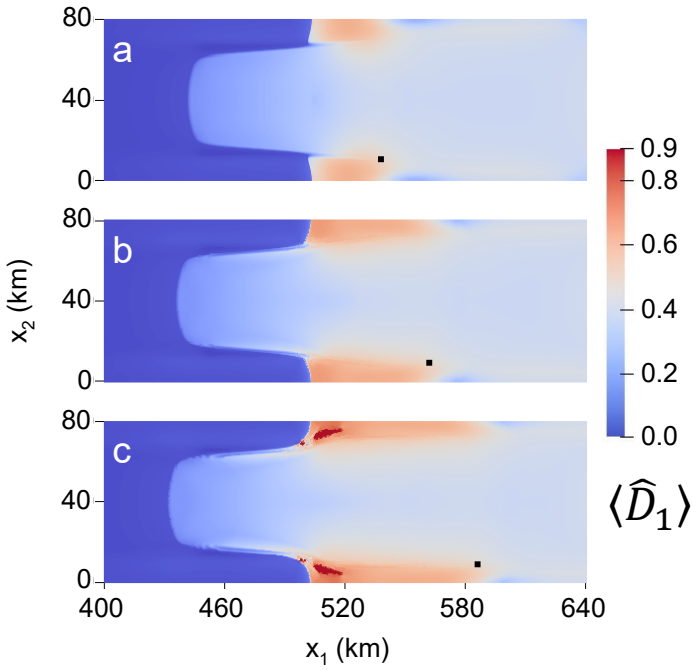

Figure 3-7. Anisotropic zero-stress damage accumulation

Fully anisotropic zero-stress maximum principal damage field at **(a)** 0 years, **(b)** 16 years, and **(c)** 30 years. The black tracer particle highlights the highly-advective flow regime.

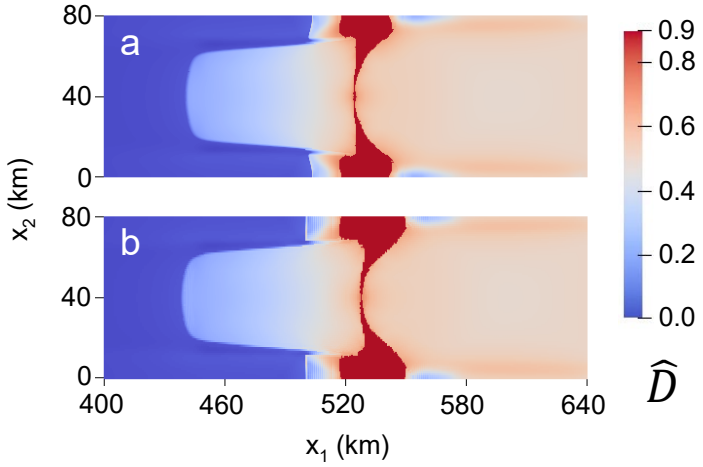

Figure 3-8. Isotropic zero-stress damage with rupture

Isotropic zero-stress damage field at calving when using $\widehat{D}_{\mathrm{cr}} = 0.7$ for a grid resolution of **(a)** 0.5 km versus **(b)** 1 km. Grid dependence is most apparent in the vastly different times to calving of **(a)** 0.553 years versus **(b)** 1.607 years.

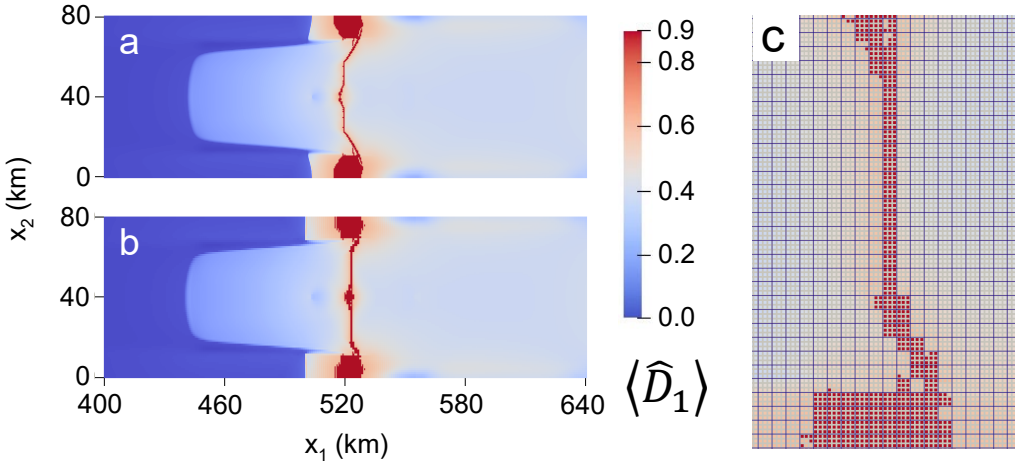

Figure 3-9. Anisotropic zero-stress damage with rupture

Fully anisotropic zero-stress maximum principal damage field at calving when using $\widehat{D}_{\mathrm{cr}} = 0.6$ for a grid resolution of **(a)** 0.5 km versus **(b)** 1 km. The rifts propagate nearly instantly, with times to calving of **(a)** 5.73 hours and **(b)** 5.99 hours. The rift paths show clear grid dependence, as shown in detail **(c)** for the 1 km case.

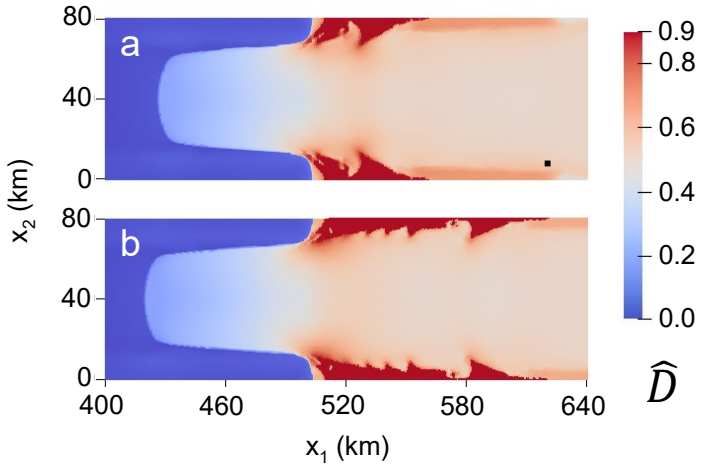

Figure 3-10. Isotropic zero-stress damage accumulation with necking

Isotropic zero-stress damage field, as modified to include necking, at **(a)** 16 years, and **(b)** 30 years. The initial field at 0 years is identical to Figure 3-6a.

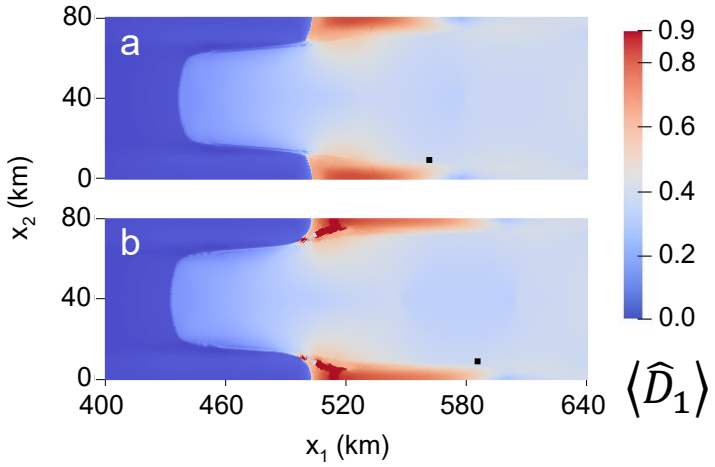

Figure 3-11. Anisotropic zero-stress damage accumulation with necking

Fully anisotropic zero-stress maximum principal damage field, as modified to include necking, at **(a)** 16 years, and **(b)** 30 years. The initial field at 0 years is identical to Figure 3-7a.

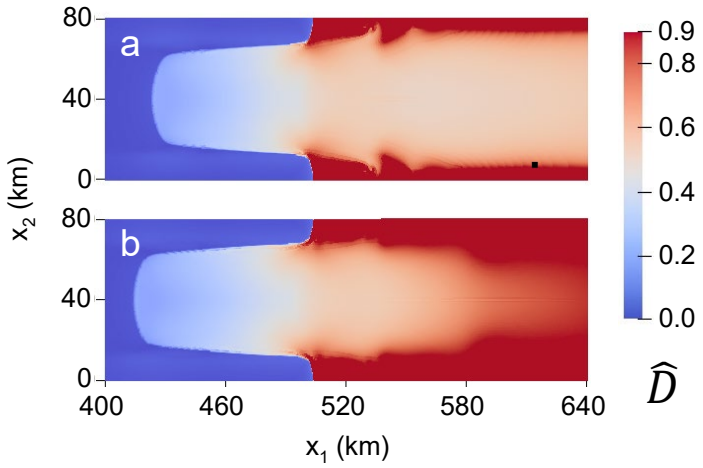

Figure 3-12. Isotropic zero-stress damage accumulation with basal melting

Isotropic zero-stress damage field, as modified to include necking and 5 m a^{-1} basal melting for floating ice, at **(a)** 16 years, and **(b)** 30 years. The initial field at 0 years is identical to Figure 3-6a.

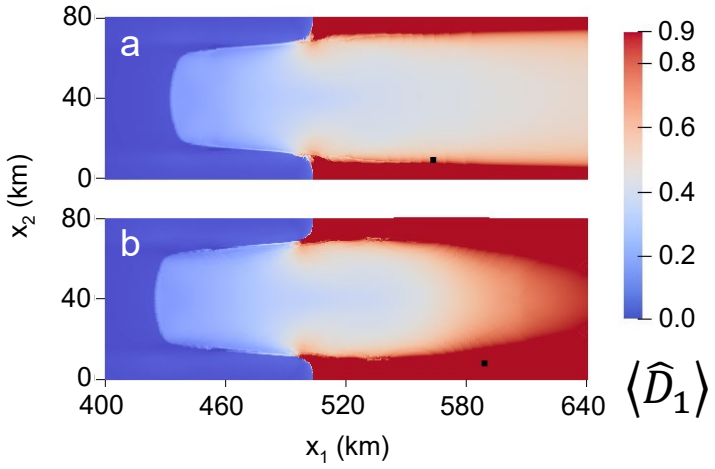

Figure 3-13. Anisotropic zero-stress damage accumulation with basal melting

Fully-anisotropic zero-stress maximum principal damage field, as modified to include necking and 5 m a^{-1} basal melting for floating ice, at **(a)** 16 years, and **(b)** 30 years. The initial field at 0 years is identical to Figure 3-7a.

Chapter 4. Application of shallow shelf creep damage to the 2017 calving of iceberg A-68 on the Larsen C Ice Shelf

Abstract

Ice shelf fracture plays essential roles in controlling Antarctic mass loss through calving and weakening of ice-shelf buttressing, and the combined generalized interpolation material point method (GIMPM) and creep damage framework developed in Chapter 3 offers a promising approach for explicitly including these processes within large-scale shallow-shelf, ice-flow models. However, this framework was only tested within an idealized setting, and had not yet been shown capable of reproducing observed large-scale fracture. Furthermore, the underlying creep damage model relies on parameters that have only been calibrated at the scale of individual crevasses or smaller, and it is unknown whether these parameters are also appropriate for large-scale applications. Here, we investigate the effectiveness of the GIMPM-SSA-damage framework for real applications by simulating the final two years of rifting on the Larsen C Ice Shelf that resulted in the calving of tabular iceberg A-68 in 2017. Through a series of tuning experiments, we determine that most of the damage parameters have little influence on the path of rifting, but do influence the rate of rift propagation. The parameter with the largest influence on the rift path is the maximum level of 2-D damage, which controls the residual strength between rift flanks and rate of rift widening. Consequently, we develop and test a technique to better represent the physical processes encapsulated by this parameter. This scheme allows rifts to be represented as a discontinuity at runtime, and accounts for the external pressures on rift flank walls associated with seawater, ice mélange, and contact between rift flanks, as well as any cohesive strength of the ice mélange.

4.1 Introduction

Crevasses that penetrate the full thickness of ice shelves are known as rifts, which often propagate laterally to produce large tabular icebergs. As described in the previous chapters, calving accounts for roughly half of mass loss in Antarctica, and rifts can cause upstream ice to accelerate as buttressing is reduced. Despite the importance of rift systems, the processes by which rifts propagate remain poorly understood. Observational evidence suggests that rift propagation is primarily controlled by glaciological stresses associated with creep flow (e.g. Joughin & MacAyeal, 2005; Bassis et al., 2005, 2007, 2008). However, rifts also tend to propagate in episodic bursts at rates that can exceed the background flow rate. Therefore, attempts to model rifting (e.g. Larour et al., 2004, Hulbe et al., 2010, Plate et al., 2012) have focused on a linear elastic fracture mechanics (LEFM) approach, where the glaciological stresses are only included as a load near the rift tip. However, these LEFM approaches do not account for the feedback between the flow and fracture processes (e.g., the effect of rift initiation and propagation on the ice shelf stress state), and are not generally suited for widespread application within large-scale models. For example, when using LEFM, rifts must be pre-initialized and remeshing is required whenever the rift propagates. Furthermore, episodic bursts of propagation do not necessarily imply that LEFM models are better suited for capturing rifting. Seismic measurements suggest that rift propagation could be occurring due to time-dependent damage accumulation, where microcracking ahead of the rift tip develops gradually under the action of internal glaciological stress and eventually ruptures episodically into a full-thickness fracture (Bassis et al., 2007). Episodic rift propagation is also likely related to material heterogeneities (de Rydt et al., 2018). For example, rift propagation is often slowed or inhibited at suture zones,

which are areas of soft marine ice that bind together neighboring units of inflowing meteoric ice (e.g. Borstad et al., 2017).

The overarching goal of this chapter is to test the GIMPM-SSA-creep damage model on a real ice shelf to demonstrate that the model is valid for simulating rifting and to determine the appropriate tuning of the damage parameters for large-scale applications. To do so, we simulate the final two years of rifting on the Larsen C Ice Shelf that resulted in the calving of iceberg A-68 in 2017. The Larsen C Ice Shelf (Figure 4-1) is the largest ice shelf on the Antarctic Peninsula. It is anchored in place by two major pinning points at the ice front, the Gipps Ice Rise and the Bawden Ice Rise, and is associated with several suture zones. The suture zone downstream of the Joerg Peninsula (Figure 4-1a; shaded yellow) prohibits the further propagation of a series of rifts that form downstream of the Kenyon Peninsula. The rift we model here is associated with Gipps Ice Rise, and propagated through this suture zone in 2014 (rift tip starred in Figure 4-1a). Subsequent propagation over the next several years resulted in the calving of the 5,800 km^2 iceberg A-68 on July 12, 2017 (Hogg & Gudmundsson, 2017). Figure 4-1b shows the ice shelf and iceberg about four months after calving.

A potential criticism of the creep damage model, when applied at any spatial scale, is the large number of parameters that must be tuned. While most parameter values have been phenomenologically constrained according to laboratory uniaxial tests (Pralong and Funk, 2005; Duddu and Waisman, 2012), it is questionable whether this tuning is broadly applicable to other stress regimes such as shearing, for which laboratory data is generally unavailable. Furthermore, some parameters, such as the brittle-ductile failure weights in the Hayhurst criterion (3.9b), cannot be precisely determined so that a wide range of values may be possible. Nevertheless, use of these parameters was reasonably successful when applied at the scale of individual crevasses

to simulate the spatial pattern and timing of two calving events in the Swiss Alps (Pralong and Funk, 2005). A recent study (Duddu et al., 2020) showed that the creep damage model is consistent with LEFM and zero-stress models for isolated and closely-space crevasses in idealized rectangular glaciers, respectively, and argued that the former is much more appropriate for realistic glacier geometries. However, it is unknown whether the creep damage parameters determined from creep experiments on laboratory-made polycrystalline ice and tuned at the scale of individual crevasses are appropriate for use within the large-scale SSA-creep damage parameterization.

In this chapter, we show that the SSA-creep damage model is capable of reproducing observed fracture with only minimal changes to the damage parameters that were tuned at smaller spatial scales, and that model response is relatively insensitive to the exact specified weighting of the Hayhurst criterion within a certain range. We also use the model to investigate the rift dynamics that appear to impact the likelihood and direction of propagation. To facilitate this analysis, we test a new method for modeling rifts as a discontinuity in real time. All prognostic simulations are initiated from a diagnostic model corresponding to the configuration of the Larsen C system in 2015, and we begin this paper by detailing the development of this diagnostic model in Section 4.2. We then present the prognostic tuning experiments in Section 4.3, and the rift dynamics tests in Section 4.4. In Section 4.5, we discuss the results and potential future developments, and we offer concluding results in Section 4.6.

4.2 Data Assimilation and Diagnostic Model

We incorporate the geometry and velocities of the 2015 Larsen C ice system using data from several satellite sensors, and infer the viscosity and friction parameters that minimize mismatch

between observed and modeled velocities. This inversion scheme largely follows a previous study (Fürst et al., 2015). However, the novelty of our procedure lies in how we separate three vertically-averaged fields that are assumed to contribute to the inferred viscosity (flow-rate) parameter, $\bar{B}$: the ice hardness from temperature, $\hat{B}$; isotropic 2-D damage, $\overline{D}$; and an enhancement factor, E, which we primarily associate with variations in fabric orientation. We can determine $\hat{B}$ from a 3-D temperature solution. However, it is more challenging to separate $\overline{D}$ and E because ideally, spatial variation in $\overline{D}$ should be sharp to represent the jagged fracture morphology while spatial variation in E is likely smoother to describe crystal fabric evolution. For our purposes, a smooth variation in E is also preferable so that it does not bias the damage response during the tuning experiments, where it is treated as a constant background parameter. Here, we are able to separate the a sharp $\overline{D}$ field and smooth E field using a series of two inversions, where $\overline{D}$ is extracted from the first inversion and E from the second. Note that we infer an isotropic 2-D scalar damage variable, owing to the difficulty in inverting for an anisotropic 3-D tensor damage variable; however, the accumulation of new damage during the forward simulations is treated using a fully-anisotropic, 3-D damage tensor.

4.2.1 *Ice Geometry*

The domain of our model includes the entirety of the Larsen C ice sheet-ice shelf system. Modeling the entire domain, included grounded and floating ice, is necessary to accurately determine the 3-D temperature solution. Furthermore, rift propagation during prognostic simulations is expected to cause velocity changes across the entire ice shelf that will likely reach the grounding line, although this impact could be minimal (Borstad et al., 2017). Nevertheless, we restrict our damage solution to floating ice, where the SSA solution, data, and quantities

derived from the inversions are most reliable. We calculate ice shelf thickness from 500 m resolution Cryosat-2 swath-processed surface heights following Smith et al. (2017) under the assumption that floating ice is in hydrostatic equilibrium. These surface heights are taken as the mean of available 2009-2017 data, and we subtract firn air content taken as the mean over 2000-2014 as provided in RACMO2.3 (Van Wessem et al., 2014). Ice thickness from the BEDMAP2 compilation (Fretwell et al., 2013) is used for all grounded ice, as well as for minimal filling of gaps in the Cryosat-2 coverage of floating ice.

4.2.2 *Temperature solution*

Our solution strategy for obtaining the temperature field is based on a published thermomechanical model (Pattyn et al., 2010; Van Liefferinge and Pattyn, 2011). In this model, an iterative procedure is used to simultaneously solve for steady-state temperature and velocity in 3-D. Temperature is determined by solving an advection-diffusion-type equation. To calculate the 3-D velocity solution, vertically-averaged 2-D velocities are first determined according to a mixture of observed surface velocities and balance velocities (LeBroq et al., 2006; Budd & Warner, 1996). From these 2-D velocities, the 3-D solution is derived using the shallow-ice approximation (Hutter, 1983), mass conservation (Hindmarsh, 1999; Hindmarsh et al., 2009), a Weertman sliding law (Hindmarsh & LeMeur, 2001), and a basal melting rate parameterization (Pattyn et al., 2010). For floating ice, the published solution (Pattyn et al., 2010) determines temperature using a simple analytical solution that neglects horizontal advection.

For grounded ice, we implement the thermomechanical model with no modification. We use smoothed surface velocities derived from a compilation of 2015 Landsat-8 data (Pope, 2016)

with minimal infilling of gaps in coverage using the 2015-2016 MEaSUREs data mosaic (Rignot et al., 2017). For surface temperature and mass balance, we use the annual means from 1979-2015 in RACMO2.3 (Van Wessem et al., 2014), and for the basal boundary condition, we assign a geothermal heat flux derived from satellite magnetic measurements (Fox Maule et al., 2005). For floating ice, we do not use the given analytical solution for temperature, as it neglects horizontal advection. Instead, we calculate 3-D velocities and solve for temperature numerically as was done for grounded ice. We set the horizontal velocities ($\boldsymbol{v}_H$) to the observed 2-D surface velocities, and calculate vertical velocity as

$$v_3 = \frac{\rho_\mathrm{w} - \rho}{\rho}\dot{b} - \frac{\rho}{\rho_\mathrm{w}}\dot{a} - z(\nabla \cdot \boldsymbol{v}_H)\,, \tag{4.1}$$

where $\dot{a}$ and $\dot{b}$ correspond to surface and basal mass balance, respectively (Weis, 2001). As written, this expression assumes a constant sea level of 0 m. For both mass balance terms, positive values correspond to accumulation. We determine the basal mass balance, $\dot{b}$, from mass conservation assuming steady-state conditions: $\dot{b} = H(\nabla \cdot \boldsymbol{v}_H) + \boldsymbol{v}_H \cdot \nabla H - \dot{a}$, and set basal ice shelf temperature to -2°C.

Using the finite element routines available in Elmer/Ice (Gagliardini et al., 2013), we first solve for grounded ice temperature only, and then solve for ice shelf temperature using the grounded ice solution as an upstream boundary condition. To construct the 3-D computational mesh, we extrude a 2-D mesh of the footprint of the domain into 41 vertical layers evenly spaced between the ice base and surface. The 2-D mesh is also used for the inversions, and has a horizontal resolution of ~1 km. Given a maximum ice thickness in the domain of 1831 m, the maximum vertical resolution in the 3-D mesh is ~45 m.

4.2.3 *Inversions*

In the first of the two inversions, we simultaneously infer the positive basal friction coefficient, $\hat{\beta}^2$, and the vertically-averaged modified viscosity parameter, $\bar{B}$, which enters the SSA through the vertically-averaged ice viscosity

$$\bar{\eta} = \frac{1}{2}\bar{B}\dot{\varepsilon}_{\mathrm{e}}^{(1-n)/n}, \tag{4.2}$$

Here, we assume $\bar{B}$ is comprised of the combined contributions to viscosity from temperature, isotropic 2-D damage, and the enhancement factor as given by

$$\bar{B} = (1 - \bar{D})E^{-1/n}\hat{B}, \tag{4.3}$$

where $\hat{B} = \frac{1}{H}\int_b^s B(T^*, z)$ is the vertically-averaged temperature-dependent flow rate factor calculated using the standard Arrhenius relation for ice (Cuffey and Paterson, 2010). Here, the basal friction coefficient enters the SSA through the basal shear stress, $\boldsymbol{\tau_b}$, as

$$\boldsymbol{\tau_b} = \hat{\beta}^2 \cdot \boldsymbol{v}_b, \tag{4.4}$$

where both $\boldsymbol{\tau_b}$ and $\boldsymbol{v}_b$, the basal velocity, are vectors tangential to the ice base (Cuffey and Paterson, 2010). For the SSA, the basal ice velocity is identical to the depth-invariant horizontal velocity. The procedure for the dual inversion is detailed in full in Fürst et al., (2015), which like the temperature solution, we implement using the finite element routines available in Elmer/Ice. At the start of the inversion, we use $\hat{B}$ (Figure 4-2a) and the local gravitational driving stress as initial guesses for $\bar{B}$ and $\hat{\beta}^2$, respectively. We solve the inversion several times using different levels of regularization, after which a solution must be selected from the results. To select a solution, Fürst et al., (2015) employed the L-curve method (Hansen, 1992), which determines the

solution that best minimizes the mismatch between observed and modeled velocities without overfitting. However, the purpose of this first inversion in our case is to determine an initial damage field, and therefore, we do not strictly adhere to the L-curve method. Instead, we extract a damage field from each solution for $\bar{B}$, and then choose by hand the smoothest solution for $\bar{B}$ that still captures visible rifting from satellite observations in the extracted damage field. The damage field from the inversion, $\overline{D}_{\mathrm{inv}}$, is extracted wherever the inferred $\bar{B}$ is lower than $\hat{B}$ (Borstad et al., 2013) as

$$\overline{D}_{\mathrm{inv}} = 1 - \frac{\bar{B}}{\hat{B}}, \tag{4.5}$$

and must be adjusted so that $0 \leq \overline{D}_{\mathrm{inv}} \leq 1$. We only allow damage on the shelf, as the results for grounded ice are not reliable due to the uncertainty associated with data errors on mountainous terrain, the use of a dual inversion, and use of the SSA indiscriminately throughout the domain. The results for $\hat{B}$ from this first inversion are given for the ice shelf in Figure 4-2b. The extracted damage field (Figure 4-2d) captures the observed rifting between the Kenyon Peninsula and Gipps Ice Rise. We also see weakening around the margins due to horizontal shear from lateral friction and near the grounding line due to vertical shear as ice adjusts to full-floatation.

From $\bar{B}$, $\hat{B}$, and $\overline{D}_{\mathrm{inv}}$, the enhancement factor can be calculated as

$$E = \left(\frac{\bar{B}}{(1 - \overline{D}_{\mathrm{inv}})\hat{B}} \right)^{-n}. \tag{4.6}$$

Ideally, we intend for E to be a smoothly varying field that represents the gradual transition of fabric orientation from the shear-based regime of grounded ice to the primarily tensile regime of ice shelves. However, extracting E from the first inversion is not conducive to smoothness because E will equal one in damaged regions, but takes smaller values (mostly less than 0.5)

elsewhere. Furthermore, E from the first inversion encapsulates some features that may be associated with overfitting, which we would rather eliminate to facilitate clear interpretation of our parameter-tuning experiments. Thus, the use of a second inversion to determine a smooth enhancement factor is justified, which involves inverting only for the viscosity parameter. The previously inferred $\hat{\beta}^2$ and $\overline{D}_{\mathrm{inv}}$ are included within the SSA solution and a larger regularization term is selected, thereby guaranteeing that a smooth enhancement factor may be extracted from the solution.

The results for the overall viscosity parameter, $\bar{B}$, from this second inversion are given in Figure 4-2c, and the enhancement factor is given in Figure 4-2e. The enhancement factor varies from $E \approx 1$ at the grounding line to $E \approx$ 0.6 as ice flows out of inlets into the main cavity of the ice shelf. Further downstream, E continues to decrease and the minimum values ($E \approx 0.16$) are found under biaxial tension near the ice front. These values appear to be reasonable when compared to previously-published estimates of ice shelf enhancement factors associated with fabric orientation. On ice shelves, values for the enhancement factor should generally be taken as less than one to reflect the stiffer girdle-type fabrics that polycrystal models suggest form under tension (Castelnau et al., 1996). One study using an orthotropic flow law (Ma et al., 2010) estimated that an enhancement factor associated with variations in ice fabric under uniaxial tension varies from approximately 1.0 at the onset of ice streams to between ~0.5-0.7 for ice shelves. Another study (Pollard and DeConto, 2012) assigned an enhancement factor of 0.3 for ice shelves within an ice sheet-ice shelf model mostly used for paleoclimate studies.

While the two-inversion scheme to separate $\hat{B}$, E, and $\overline{D}_{\mathrm{inv}}$ yields reasonable results, the inferred E and $\overline{D}_{\mathrm{inv}}$ will inevitably account for some other processes that impact $\hat{B}$ besides fabric and damage, including the influence of impurities, missing forces such as mélange or sea ice at

the ice front, and errors in data, temperature, and density. Additionally, some damage effects could be captured by the enhancement factor, and vice versa. The damage field extracted from the inversion only identifies the fractures that have a strong impact on current stress, and does not identify some fractures that appear in imagery (Figure 4-1). These unidentified features therefore represent shallow fractures or are shielded by larger surrounding fractures so that they have minimal effect on the stress field. Given some estimate of crevasse depths, these fractures could potentially be accounted for by increasing $\overline{D}_{\mathrm{inv}}$ while decreasing E accordingly so that the resulting viscosity parameter $\bar{B}$ is the same . Furthermore, it would be advantageous in future applications to extend the inversion to anisotropic form, as both damage and fabric orientation are anisotropic processes.

4.3 Tuning Simulations

For reference, we recall from Chapter 3 that for each material point layer, the material derivative of the second-order creep damage tensor is expressed as the Jaumann derivative (Pralong and Funk, 2005)

$$\dot{\mathbf{D}} = \frac{\partial \mathbf{D}}{\partial \mathrm{t}} = \mathbf{f} + \mathbf{W}\mathbf{D} - \mathbf{D}\mathbf{W}, \tag{4.7}$$

where t is time, $\mathbf{W}$ is the spin tensor, and $\mathbf{f}$ is the damage evolution function (Murakami, 1988)

$$\mathbf{f} = B^{*}\langle\langle \chi - \sigma_{th} \rangle\rangle^{r}\left\{\mathrm{Tr}\left[(\mathbf{I} - \mathbf{D})^{-1} \cdot \left(\boldsymbol{\nu}^{(1)} \otimes \boldsymbol{\nu}^{(1)}\right)\right]\right\}^{k}\left[(1-\gamma)\mathbf{I} + \gamma \boldsymbol{\nu}^{(1)} \otimes \boldsymbol{\nu}^{(1)}\right], \tag{4.8}$$

$$\chi = \alpha\langle \tilde{\sigma}_1 \rangle + \beta\sqrt{3\mathbf{II}_{\tilde{\boldsymbol{\sigma}}^{\mathrm{D}}}} + \lambda \mathbf{I}_{\tilde{\boldsymbol{\sigma}}} . \tag{4.9}$$

In (4.8), B^{*} is the damage rate factor, χ is the Hayhurst criterion (4.9), $\boldsymbol{\nu}^{(1)}$ is the eigenvector corresponding to the maximum effective principal stress, and γ is the anisotropy parameter. We

set r and k to constants, although these empirical parameters could be temperature or stress dependent. The weighting in the Hayhurst criterion balances the damage response between the maximum effective principal stress (weighted by α), the Von Mises stress (weighted by β), and the effective hydrostatic stress (weighted by $\lambda = 1 - \alpha - \beta$), where $0 \leq \alpha, \beta, \lambda \leq 1$. The final parameter, σ_{th}, is a stress threshold. As indicated by the Macaulay bracket, $\langle\langle \cdot \rangle\rangle$, damage accumulation will only occur where $\chi > 0$. Finally, recall that within the SSA parameterization, the effective Cauchy stress is parameterized as $\tilde{\sigma}_{ij} = \tilde{\sigma}_{ij}^{D} - p_{\text{eff}}\delta_{ij}$, where p_{eff} is the effective pressure (3.14-3.16), and where the water pressure term in p_{eff} is not a function of damage as defined in the poro-damage approach for hydrofracture (Duddu et al., 2020).

The damage parameters that we focus on tuning are the weights of the Hayhurst criterion and stress threshold, as well as the maximum allowed vertically-averaged damage, $\overline{D}_{\text{max}}$. These parameters have the largest impact on the spatial distribution of damage. The remaining parameters (γ, r, k, and B^*) are largely except from our tuning experiments. We always set $\gamma = 1$ to model damage accumulation in fully-anisotropic form because we concluded in Chapter 3 that strong anisotropy is most consistent with observed rifting. Anisotropic damage is also physically consistent with linear elastic fracture mechanics theory. A study that used the creep damage model to predict 2-D crevasse depths found that the parameters r, k, and B^* largely only affect the rate of damage accumulation, and did not affect the final crevasse depths (Duddu et al., 2020). We are more interested here in damage patterns rather than matching the propagation rate of the rift exactly, so we always set $r = 0.43$ and $k = 4$, which are approximate values derived from laboratory data that we also used in Chapter 3 (Pralong and Funk, 2005; Duddu and Waisman, 2012). We adjust B^* or the stress threshold as needed to keep the simulation time within a range of ~1-3 years for the rift to propagate and result in tabular calving, where the ideal

time to calving would be ~2 years given that we initialize the simulations using data mosaics from 2015 and full calving was observed in mid-2017. However, unless otherwise noted, we adopt the same value for B^* from Chapter 3 of $B^* = 5.23 \times 10^{-7}$ MPa^{-r} s^{-1}.

We implement the SSA-creep damage model using the GIMPM. For all simulations in this chapter, we use a grid resolution of 500 m, where each active grid cell is initialized with 4 material points. Given the short timescale of the simulation, we assume surface and basal mass balance are negligible. Unless otherwise indicated, each material point is associated with 41 vertical layers on which 3-D temperature and damage is defined. The 3-D temperature solution from Section 2 is interpolated to material point layers at the beginning of the simulation, and is held constant on each material point over time. However, values for the enhancement factor and friction parameters defined on the grid are newly interpolated to material points each computational cycle, except for at material points near the ice front that have advected beyond the original domain on which these parameters values were originally determined in Section 2.

Before reporting the results, we address our treatment of the initially-damaged material points during the tuning simulations. The vertical distribution of damage of these material points is unknown, and their damage values from the inversion are isotropic while new damage will be anisotropic. For simplicity, we therefore do not allow further damage accumulation on these material points. Furthermore, we redraw the initial portion of the inferred rift as a sharper crack (~1.5 – 2 km wide) with a vertically-averaged isotropic damage value of $\overline{D} = 0.86$. This modified initial damage field is shown in Figure 4-3a. The sharper initial rift serves the purpose of correcting for the overly diffuse damage field from the inversion, and helps induce further rift propagation across the domain. However, we note that these treatments are not strictly necessary. We have also tested allowing the initially-damaged material points to accumulate further

isotropic damage, with and without initializing a sharper initial rift. For some of these tests, we assigned vertical damage profiles with either the same value at all depths, and for others, we followed an "effective ice thickness" scheme proposed by a previous study (Keller and Hutter, 2014). In either case, very little damage would accumulate further outside of the rifting area of interest. If the diffuse initial rift was not redrawn as a sharper crack, it could still grow to $\overline{D}_{\max}$ and propagate, but the initial rifting area would become unrealistically wide as a result. Redrawing a sharp rift is more consistent with observations, and given that very little damage accumulates in other areas of the domain, we consider our simplified treatment to be justified and better-suited for a clear interpretation of the tuning experiments in this chapter. Of course, the greater goal would be able to stably and accurately initiate simulations directly from an inferred damage field, and we discuss this possibility further in Section 5.

4.3.1 *Tuning of Hayhurst criterion and stress threshold*

We conducted a parameter sweep to calibrate the Hayhurst weights. During this process, we adjusted the stress threshold to a high enough value to prevent spurious damage accumulation, while being low enough to allow rifting. The heuristic estimate to determine the stress threshold proposed previously (Pralong and Funk, 2005) may not applicable to our large-scale and nonlocal damage formulation. All simulations in this section use the same maximum 2-D damage as the initial rift ($\overline{D}_{\max} = 0.86$). All other damage parameters are given in Table 1.

We first present results of a model with the Hayhurst weighting as calibrated at the scale of individual crevasses (Pralong and Funk, 2005), with α=0.21 and β=0.63. We choose a stress threshold of $\sigma_{\text{th}} = 0.2$ MPa. The maximum principal 2-D damage field is plotted in Figure 4-3 at (a) 0 years, (b) 1.75 years, and (c) 2.2 years, which corresponds to the configuration just before

the rift completes the calving event, at which point the rift begins to quickly expand and the simulation is ended. The yellow dotted line in (c) shows the observed rift path, which the simulated rift path reproduces nearly exactly for the first 1.75 years (b). However, the simulated rift veers more gradually towards the ice front during the final ~0.5 years before calving, and also begins to widen more rapidly than earlier in the simulation. In part, this mismatch may be due to inaccuracy in the velocity data or inversion, to modeling only viscous stresses, or to our not accounting for some anisotropic background damage (e.g. observed widespread crevassing that was not initialized in the damage field). In addition, some inaccuracy could be attributed to our modeled front position, which due to masking of our data sources, corresponds to a slightly less advanced front than observed in 2015. Another source of potential error concerns our choice of a constant $\overline{D}_{\max}$, which probably varies spatially and temporally, and which can influence the rift path as shown in Section 4.3.2. Even without these potential errors or over-approximations, the simulation presented here still performs remarkably well, so we conclude that the Hayhurst weights tuned at smaller spatial scales (Pralong and Funk, 2005) also appear to be adequate for large-scale simulations, though a range of other values may also be appropriate. The time to calving of ~2.2 years is accurate. The simulation even reproduces a small amount of radial rifting observed at the center of the ice front, as indicated by the arrow in Figure 4-3c. The corresponding observed radial rifting is indicated by arrows in Figure 4-1. This radial damage occurs because this part of the ice shelf is under biaxial tension, and the lateral stress exceeds the longitudinal stresses.

We next consider the extreme cases where the Hayhurst criterion is represented entirely by one of the three weights. The final rifts paths are given in Figure 4-4, where (a) corresponds to fully-tensile, brittle damage evolution (α=1, β=0, λ=0); (b) corresponds to ductile damage

evolution based solely on Von Mises stress (α=0, β=1, λ=0); and (c) corresponds to damage evolution based on solely on the hydrostatic stress (α=0, β=0, λ=1). The α=1 and β=1 cases show essentially the same response as the recommended weighting in Figure 4-3, while the λ=1 case does not propagate, and instead is characterized by large-scale diffuse damage. Note that in an attempt to induce propagation in the λ=1 case, we reduced the stress threshold to $\sigma_{\text{th}} = 0.075$ MPa, as hydrostatic stress/effective pressure is small at all depths within the SSA damage parameterization. Given that the maximum effective principal tensile Cauchy stress is derived in part from this same effective pressure, we must also decrease the stress threshold for the α=1 case ($\sigma_{\text{th}} = 0.15$ MPa). Because the α=1 and β=1 cases result in similar propagation, any combination of α and β should yield similar results as long as the λ and σ_{th} are small enough to allow propagation.

In Figure 4-5, we report results for a series of weightings close to the values given in Pralong and Funk (2005), where we hold each weight at its given value while varying the other weights $\pm$0.15 of their respective given values. For this experiment, we used 21 vertical layers rather than 41 vertical layers, and also report the 21-layer result with the α=0.21, β=0.63 weighting to show that similar results are obtained as compared to the 41-layer case in Figure 4-3. As expected, varying the Hayhurst weights $\pm$0.15 of their given values has minimal impact on the rift propagation, provided the stress threshold is decreased as λ is increased. However, decreasing the stress threshold in the cases in Figure 4-5 is largely not necessary to induce propagation; instead, it is largely adjusted to better match the time to calving, where smaller stress thresholds result in faster rift propagation. For example, the α=0.36 and β=0.48 calves after ~3.7 years using $\sigma_{\text{th}} = 0.2$ MPa versus ~1.35 years using the lower $\sigma_{th} = 0.175$ MPa reported in Figure 4-5. Both cases yield the same rift path.

The parameteric studies varying the Hayhurst criterion show that for rifting, the exact weighting specified is largely arbitrary, as long as α and β are the dominant parameters. Thus, use of the SSA-creep damage model can proceed with increased confidence in the spatial damage response. In practice, the weighting may as well be chosen within the recommended range derived from laboratory experiments (Pralong and Funk, 2005), though we have shown that values outside of this range (e.g. the α=1, β=0, λ=0 case) are also effective. Our results largely eliminate concerns regarding tuning of the Hayhurst weights, but we note that more ice shelves will need to be modeled to better constrain an appropriate stress threshold. The values chosen above may give an approximate range of appropriate values, but potential dependence on other parameters such as temperature and grid/material point resolution should be investigated. Further complexity is potentially introduced when considering that the brittleness of ice (i.e. weighting of α) is proportional to stress and inversely proportional to temperature (Arakawa and Maeno, 1997). Uncertainty associated the stress threshold is not unique to our creep damage model. Recent studies that have applied a different, von Mises-based calving parameterization to marine-terminating glaciers in Greenland have needed to calibrate the stress threshold for each glacier separately (Morlighem et al., 2016, 2019).Nevertheless, the above experiments have shown that the model in its current form is capable of simulating observed rifting, and therefore, can be used in rift propagation and calving studies.

4.3.2 *Tuning of maximum 2-D damage*

As implemented above, $\overline{D}_{\max}$ accounts for any residual strength between the flanks of a rift, where this residual strength is zero if $\overline{D}_{\max}$ is set to the theoretical maximum value of one. Physically, the presence of residual strength can likely be related to any remaining contact

between rift flanks, the cohesive strength and amount of mélange filling the rift, and a force imbalance similar to at the ice front which acts to close the rift. We investigate and discuss these specific processes further in Section 4.4. Here, we simply show how value of $\overline{D}_{\max}$ controls the rate at which the rift opens and widens, which in turn, can affect the rate and path of propagation.

In Figure 4-6a, we show the rift propagation obtained from setting $\overline{D}_{\max}$ = 0.95, rather than $\overline{D}_{\max}$ = 0.86 as in the previous simulations. We use α=0.21 and β=0.63 for comparison with Figure 4-3. With the greater $\overline{D}_{\max}$, the rift immediately curves towards the ice front rather than propagating further laterally, towards Bawden Ice Rise as in Figure 4-3. This behavior occurs because by raising $\overline{D}_{\max}$, the nascent iceberg is allowed to rotate much faster, roughly around an axis near the rift tip, in accordance with greater velocities downstream of the rift (~3000 m a^{-1} at t = 0 years versus ~1000 m a^{-1} in the $\overline{D}_{\max}$ = 0.86 case). In other words, the rift widens faster towards Gipps Ice Rise than towards the rift tip. The increased curvature in the rift path is not directly related to the greater weakness at the rift tip; if $\overline{D}_{\max}$ = 0.86 is maintained in the area of the initial rift while allowing $\overline{D}_{\max}$ = 0.95 for new propagation, the simulated rift path does not immediately curve towards the ice front, and instead better matches the observed rift path (Figure 4-6b). However, in this case, velocities downstream of the rift are still much greater than the purely $\overline{D}_{\max}$ = 0.86 case. For a rift position similar to Figure 4-3b, the mixed $\overline{D}_{\max}$ = 0.86/0.95 case yields downstream velocities of ~2750 m a^{-1} versus downstream velocities of ~1500 m a^{-1} in the purely $\overline{D}_{\max}$ = 0.86 case. Consequently, the mixed $\overline{D}_{\max}$ = 0.86/0.95 propagates faster, with a time to calving of ~1.15 years versus ~2.2 years in the $\overline{D}_{\max}$ = 0.86 case. Despite the simplistic treatment of rift dynamics using a scalar $\overline{D}_{\max}$, these simulations demonstrate the how the relative widening of a rift along its trajectory and rotation nascent iceberg dictate the rift path and propagation rate.

4.4 A discontinuous representation of rift dynamics using damage

While somewhat sufficient for the Larsen C Ice Shelf, modeling rifts with a constant $\overline{D}_{\max}$ is not a robust parameterization for determining the rate at which a rift opens, or the amount of stress transmitted between rift flanks. A more complete description of rift dynamics should include the force imbalance at the flank boundary, where gravitational ice forces are partially opposed by seawater pressure and backpressure from mélange. Furthermore, the mélange should be able to transmit stresses. In this section, we describe a solution that incorporates this type of discontinuous boundary without leaving the damage framework, and we test it on the Larsen C configuration.

4.4.1 *Discontinuous boundary*

The boundary condition on the flanks of the rift takes a similar form to the ice front boundary condition (Equation 2.8), which gives the depth-integrated form of the seawater pressure opposing ice flow. However, for rifts, we consider two additional sources that induce opposing pressure on rift flank walls: ice mélange within the rift (Figure 4-7a) and contact between rift flank walls (Figure 4-7b). This contact has been observed near the surface of newly-formed rifts (de Rydt et al., 2018), likely due to flexure of the ice shelf closing the top of the rift upon formation (Lipovsky, 2019). To formulate the boundary condition, we first define a thickness variable associated with the mélange, $\widehat{H}$, as well as a corresponding ice mélange draft

$$\hat{b} = \widehat{H}\frac{\rho_i}{\rho_w}, \tag{4.10}$$

which as written, assumes ice mélange is in floatation. Similarly, we define a variable associated with the thickness of contact between flank walls, $\widetilde{H}$, where we assume here that contact only occurs above sea level. For simplicity, we further assume here that contact is not associated with any friction perpendicular to the crack (Mode II/III directions). The depth-integrated expression for pressure on the rift flank walls then takes the form

$$\int_b^s \sigma_{ij}\hat{n}_j \, dz = \frac{1}{2}[-\rho_w g(b^2 - \hat{b}^2) \; - \rho_i g(\widehat{H}^2 + \widetilde{H}^2)] \, . \tag{4.11}$$

Equation (4.11) is identical to a previously proposed function for rift flank boundaries (Larour et al., 2014), except it includes a term for contact between flank walls. Within the weak form for the SSA, this expression can be implemented as a boundary condition specified on a boundary edge element of the mesh (similarly to Equation 2.14 for the ice front)

$$f_{iI} = \int_{\Gamma_{\mathrm{rf}}} \frac{1}{2}\phi_I(\boldsymbol{x})[\rho_i g(H^2 - \widehat{H}^2 - \widetilde{H}^2) - \rho_w g(b^2 - \hat{b}^2)]\hat{n}_i d\Gamma = 0 \, , \tag{4.12}$$

where Γ_{rf} is the domain associated with the edges of the rift flanks. However, here, we evaluate this expression over a diffuse zone defined by fully-damaged material points, so that the boundary condition can be enforced at runtime as the rift propagates. To do so, the boundary condition is mapped from fully-damaged material points within (or overlapping) an element to the element nodes as

$$f_{iI} = \sum_{p=1}^{n_{\mathrm{r}}} -\frac{1}{2} A_p \frac{\partial S_{Ip}}{\partial x_{\mathrm{i}}} \left[\rho_i g(H_I^2 - \widehat{H}_I^2 - \widetilde{H}_I^2) - \rho_{\mathrm{w}} g({b_I}^2 - \hat{b}_I^2)\right], \tag{4.13}$$

where n_{r} is the number of fully-damaged (rift) material points within the element. Because the rift material points have fully failed, we also set the gravitational driving stress in the SSA to zero ($\rho g H \frac{\partial s}{\partial x_i} = 0$). Note that if $\overline{D}_{\max} \approx 1$, no stresses are transmitted between rift flanks, but lower values of $\overline{D}_{\max}$ could be used to account for the cohesive strength of mélange or the

transmission of stresses between flanks that are in contact and under compression. Mélange strength could alternatively be accounted for by introducing a separate rheology model for the rifted material points. In the case that the mélange has no strength, (4.13) can be thought of as the material point equivalent of an element-deletion scheme in FEM, whereby a fully-failed element is removed from the mesh and (4.12) is applied at the new boundaries that appear in its place. Though (4.13) is written with the GIMPM shape functions, S_{Ip}, they may be replaced by ϕ_{Ip} for sMPM or FEM simulations. Specification of a normal, $\hat{n}_i$, as in (4.12) does not appear to be necessary; Equation (4.13) naturally acts to "pull" the flanks of the rift together according to the force imbalance specified in the expression. Note that the width of the rift, as represented by material points, must be at least the width of a grid cell in order to accumulate an equivalent magnitude of force on the grid using (4.13) as would be accumulated by integrating over element edges using (4.12). This requirement is satisfied in the nonlocal damage formulation because the characteristic nonlocal damage length, l_c, should already exceed the width of a grid cell.

Note that the ice thickness in (4.13) is formulated as a nodal quantity, and should correspond the thickness at flank walls. Using nodal (rather than material point) thickness guarantees that orientation and magnitude of the resultant nodal grid force is not biased by local variation in ice thickness at material points. For example, a node that is connected only to elements that are full of rift material points should have a force of zero, because it is fully located within the interior of a rift. A force of zero is guaranteed when (4.13) is formulated in terms of nodal thickness, as all element contributions cancel out. However, a force of zero is not guaranteed if (4.13) is formulated using material point thicknesses, which may vary spatially so that each element may contribute a different force. Nevertheless, the nodal thickness is still ultimately determined from mapping of material point thickness in equation (2.29). This can be

problematic in the case that the rift widens, in which case material point thicknesses within the rift tend to decrease, and consequently (4.13) does not reflect thicknesses at the flank walls. The thickness of rift material points must therefore be adjusted to reflect the thicknesses of the surrounding non-rift material points. To do so, we simply use the Gaussian kernel from the nonlocal damage scheme (3.20)–(3.21) to diffuse the thicknesses of neighboring material points to the fully-damaged material points each time step. Only the thicknesses of fully-damaged material points are allowed to change during this diffusion scheme. We run ten iterations of this scheme for each time step to guarantee that the fully-damaged material points retain thicknesses similar to the surrounding non-rift material points.

4.4.2 *Examples*

We present three simulations that demonstrate the behavior of the rift boundary condition on the Larsen C configuration. In the first simulation, we apply the rift boundary condition without any mélange fill or contact. In the second simulation, we apply additional pressure from mélange only, without rift flank contact. In the third simulation, we apply additional pressure from rift flank contact only, without mélange. In each simulation, the rift boundary condition is only applied for new rift material points, which use $\overline{D}_{\max} = 0.995$. The initialized section of the rift uses $\overline{D}_{\max} = 0.86$ as in the Hayhurst tuning simulations, and the boundary condition is not applied. Treating the initial rift separately from newly-rifting material points in this way is consistent with observations on the Ronne Ice Shelf that older rifts are filled with stronger or cohesive mélange than new rifts (Rignot and MacAyeal, 1999). Note that by setting $\overline{D}_{\max} = 0.995 \approx 1$ for the new rift material points, we essentially are assuming that stresses are not transmitted between the flanks of the rift. Here, the rift is always in tension, so equivalently, we

are assuming that mélange has essentially no tensile strength in the second simulation. All material points are assigned 41 vertical layers, and we set B^* four times larger than its previous value used earlier because the discontinuous boundary treatment tends to slow rift propagation.

During the second and third simulations, we apply the additional pressures from mélange and rift flank contact, respectively, as a function of the rift widening. We assume that mélange fill should increase as the rift widens, and as sea ice, calved ice blocks, and snow accumulate over time; conversely, rift flank contact should decrease as the rift widens, until it is eliminated entirely at full separation of the flanks. As a proxy for rift widening, we track the accumulated strain, ε_{r}, in the direction of rift opening. To determine the direction of rift opening, we save the orientation of the rift at full-thickness rupture by setting maximum principal 2-D damage component to $\overline{D}_{\max} = 0.995$, while the other principal 2-D damage components are set to slightly lower values of 0.99. The rift opens in the direction of maximum principal 2-D damage. At rupture, $\varepsilon_{\mathrm{r}} = 0$, but subsequently grows according to the strain rate in the maximum principal damage direction ($\dot{\varepsilon}_{\mathrm{r}}$) as

$$\varepsilon_r^{m+1} = \max(\varepsilon_r^m + \dot{\varepsilon}_{\mathrm{r}}{}^m \Delta t^m, 0), \tag{4.14}$$

where m is the timestep counter and Δt is the size of the timestep. In the second simulation, we define the thickness of the mélange to grow linearly as a function of ε_r as

$$\widehat{H} = \min\left(\frac{\varepsilon_r}{\varepsilon_r^{max}}, 1\right) \Psi H, \tag{4.15}$$

where ε_r^{max} is a specified maximum accumulated strain parameter and Ψ is a specified maximum fraction of the rift flank ice thickness, H, to which the mélange thickness, $\widehat{H}$, will grow when $\varepsilon_r \geq \varepsilon_r^{max}$. Similarly, in the third experiment, we define the thickness of contact between rift flanks as

$$\widetilde{H} = \left[1 - \min\left(\frac{\varepsilon_r}{\varepsilon_r^{max}}, 1\right)\right] \Psi H. \tag{4.16}$$

We assume that rift flanks are fully in contact above sea level upon full-thickness rupture (ε_r = 0), so that $\Psi = \left(1 - \frac{\rho_i}{\rho_w}\right) \approx 0.1$. We use the same Ψ for the second simulation (mélange pressure experiment), so that the maximum mélange thickness will be 10% of the local ice shelf thickness. We arbitrary set $\varepsilon_r^{max} = 0.08$ for both simulations, and we currently do not associate this value with an actual length of crack opening. We emphasize that this strain-tracking scheme is only a parameterization implemented here for proof of concept. Future research will focus on a more physical representation of mélange growth and strength, and evolution of rift flank contact.

The 2-D principal damage field near calving for the first simulation (no mélange or rift flank contact) is given in Figure 4-8a. Similarly to when using a constant $\overline{D}_{\max}$ = 0.95 (Figure 4-6a), the rift tip deflects towards the ice front at a steep angle as the rift widens faster near Gipps Ice Rise than at the rift tip, and does not propagate as far towards Bawden Ice Rise as observed (yellow dashed line). However, high velocities downstream of the initial rift are not to blame in this case. Instead, it is the boundary force (4.13) opposing rift opening (from the downstream side of the rift, specifically) that appears to divert the rift propagation towards the ice front too steeply. Results from the second simulation (pressure from mélange, but not from rift flank contact) are given in Figure 4-8b for the same point in time as the first simulation (2.175 years). Due to the presence of mélange, the boundary force opposing rift opening is decreased and the rift propagates further towards Bawden Ice Rise. While the rift path still diverts towards the ice front too quickly, this behavior is slightly less apparent that in the first simulation. Results near calving from the third simulation (pressure from rift flank contact, but not from mélange) are given in Figure 4-8c. The rift path better matches the observed path than the first two

simulations. The boundary force opposing rift opening is decreased significantly at the rift tip, so that the rift also propagates faster, reaching its reported location at 1.5 years. In Figure 4-8d, the field for ε_r for the third simulation is given at 1.125 years. The choice of $\varepsilon_r^{max} = 0.08$ results in full separation of the rift flanks approximately 15 km away from the rift tip. The relatively strong match between the observed and modeled rift paths in the third simulation suggests that partial contact of rift flanks ahead of the crack tip may play an important role in dictating spatial patterns of rifting.

The simulations that implemented the rift boundary scheme did not yield a significantly better or worse match to the observed rift path than the simulations that used damage alone. However, the rift boundary scheme always produced sharper rifting. Furthermore, the rift boundary scheme offers a more physical description of rift dynamics. For example, without the boundary scheme, stress will always be transmitted between rift flanks, because $\overline{D}_{\max}$ must be set well below its theoretical value of unity to maintain accurate downstream velocities. Crucially, when implementing the rift boundary condition, we obtain similar downstream velocities to those in Section 4.3.1, but stress is not transmitted between rift flanks because $\overline{D}_{\max} \approx 1$.

4.5 Discussion

The simulations presented in this chapter demonstrate the viability of using creep damage to model rift propagation, and the strong match between observed and modeled rift paths supports the hypothesis that rift propagation is primarily driven by microcracking ahead of the rift tip in response to viscous glaciological stresses (Bassis et al., 2007). Furthermore, we have highlighted how the rate of widening along the rift length, or rotation of the nascent iceberg, dictates the

direction and rate of rift propagation. The thickness and strength of mélange likely plays a large role in controlling rift widening, and therefore merits further attention in future studies. Some ice mélange fill is capable of transmitting stresses between rift flanks to essentially bind the flanks together and prohibit rift propagation (e.g. Rignot and MacAyeal, 1998). However, mélange can also encourage rift opening by decreasing the force imbalance between seawater and the flank walls that would otherwise act to close the rift. For the relatively small portion of the Larsen C rift that is present in 2015, the existence of thick, weak, mélange may have acted to reduce the rift flank boundary condition enough to incite further rift propagation. In Section 4.4.2, we effectively enforced such a criterion by assigning this portion of the rift with $\overline{D}_{\max} = 0.86$, and not treating this portion of the rift with the rift boundary condition (i.e. weak, full mélange fill was assumed). We note that we have also tested treating this portion of the rift with the same mélange and boundary treatment implemented for new rift material points in the second simulation of Section 4.4.2 ($\overline{D}_{\max} = 0.995$ and $\Psi = 0.1$). In this case, the mélange is too thin to significantly decrease the rift boundary forces that oppose rift opening, and the rift does not propagate. Properly calibrating the timing of the rift mélange fill and strength, as well as flank contact ahead of the rift tip, would likely produce a rift path that better matches observations.

With newly available, high resolution surface measurements from sensors like ICESat-2, the thickness of ice mélange within rifts can likely be resolved to study mélange and rift dynamics in more detail. Using the data to determine spatial variation in $\widehat{H}$, the discontinuous rift/mélange boundary scheme could then be implemented within a data assimilation scheme like the one detailed in this paper. From the inversion, it may be possible to infer a rheology for mélange that could be implemented within our model for prognostic rift propagation simulations. Ultimately, such an addition to the model could help determine rifting response to climate,

because atmospheric and ocean temperatures modulate how the mélange grows through sea ice and snow accumulation, and decays through melting. Furthermore, this type of inversion that includes mélange properties could potentially be used to calibrate some additional rift dynamics that are currently missing from the current damage model, such as friction forces for rift flanks that are in contact.

4.6 Conclusion

We performed first-ever validation studies illustrating that the GIMPM-SSA-creep damage framework can be used to model rift propagation by simulating the final two years of rifting associated with the calving of iceberg A-68 on Larsen C Ice Shelf. Tuning experiments of the damage model reveal that a variety of Hayhurst weights can produce similar rifting, and that the weights calibrated at smaller spatial scales appear to be among the most effective for large-scale application within the SSA damage parameterization. Furthermore, we use the damage model to investigate fundamental rift dynamics, and demonstrate how the widening of a rift and rotation of the developing iceberg can influence the direction and rate of continued rift propagation. To better capture the rift widening (or closing) process, we introduce a technique to dynamically introduce boundary conditions on the walls of rift flanks that accounts for the force balance between shelf ice, ice mélange, and seawater, while simultaneously allowing mélange to transmit stresses between flanks. Assuming minimal or no influence from mélange, we show that this technique yields sharper rifting than using a maximum damage value alone to represent rifting; however, additional research is necessary to properly account for the growth, decay, and strength of the mélange, which likely plays an integral role in controlling rift propagation and its relationship to climate forcings. Furthermore, we demonstrate that contact between rift flanks

near the rift tip can influence the path of rift propagation. The SSA-creep damage framework applied here should be applicable to all ice shelves, and we expect additional applications in other study areas will help better determine appropriate values for the damage stress threshold and rate factor, which are difficult to calibrate using a single ice shelf. We conclude that the SSA-creep damage framework shows promise for representing tabular calving in ice flow models, as well as the complex response of calving to changes in climate.

Acknowledgements

Huth was funded by NASA Earth and Space Sciences fellowship under grant no. NNX15AN99H. Duddu gratefully acknowledges the funding support provided by the National Science Foundation's Office of Polar Programs via CAREER grant \#PLR-1847173. Smith was funded under the NASA grant no. NNX13AP69G.

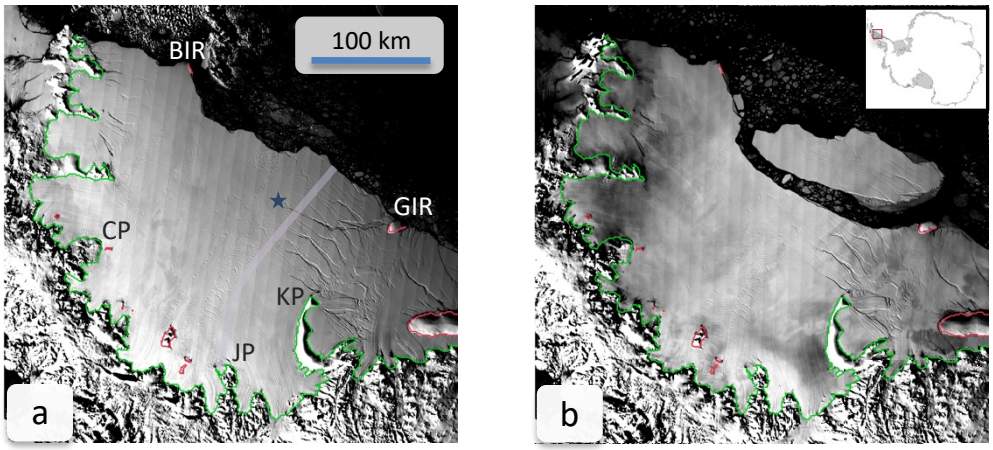

Figure 4-1. The Larsen C ice shelf: before and after calving

NASA MODIS images of the Larsen C ice shelf on **(a)** Dec. 3, 2004 and (**b)** Nov. 11, 2017, showing iceberg A-68 approximately 4 months after calving. Ice rises are outlined in red, and the grounding line is outlined in green. In **(a)**, the Gipps Ice Rise, Bawden Ice Rise, Kenyon Peninsula, Joerg Peninsula, and Cole Peninsula are labeled with their initials. The suture zone downstream of Joerg Peninsula is shaded yellow, and the star indicates the location of the rift tip.

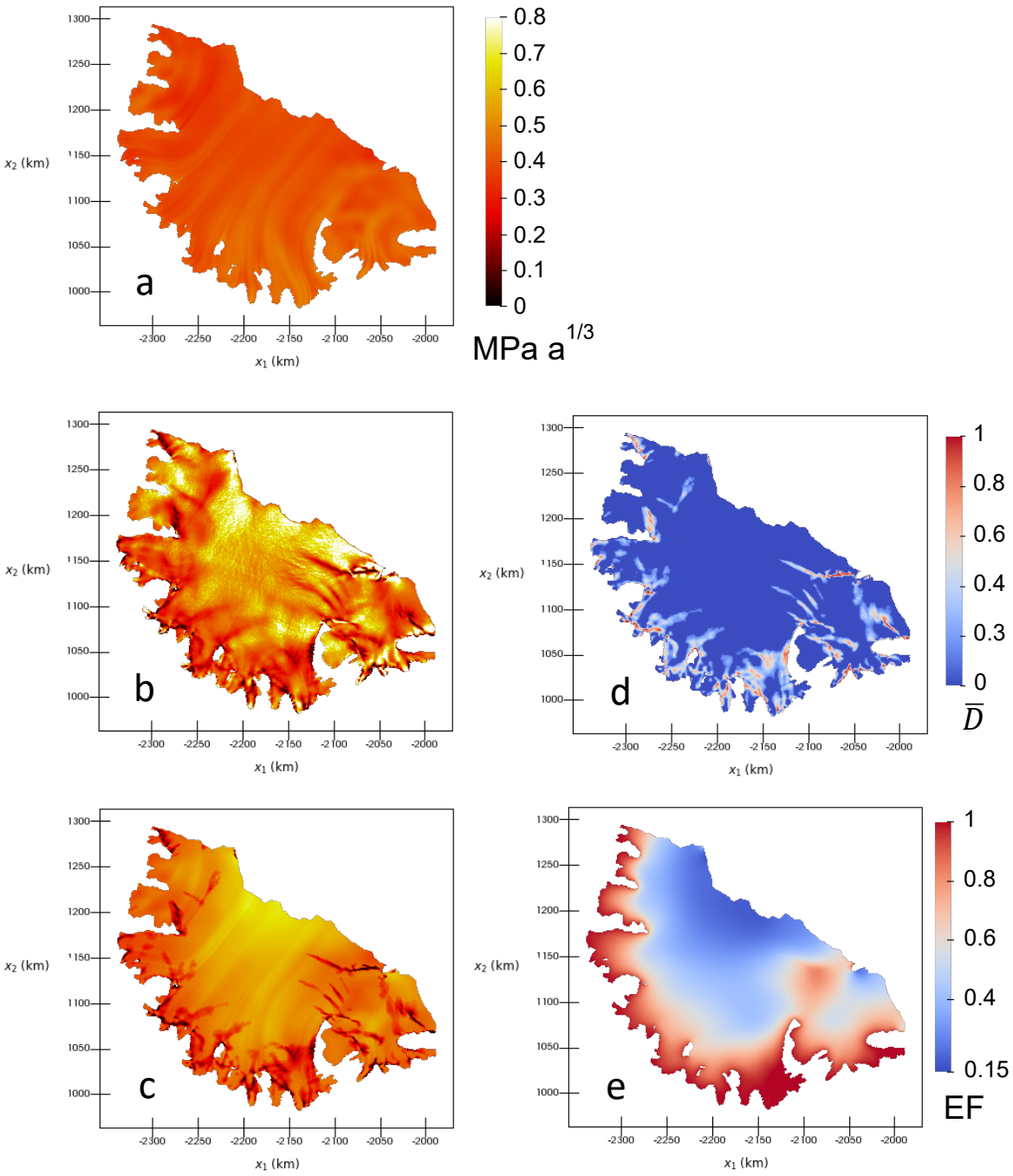

Figure 4-2. Initial fields for the viscosity parameter, damage, and the enhancement factor

The depth-averaged viscosity parameter corresponding to **(a)** temperature only, $\hat{B}$, as used for the initial guess during the first inversion; **(b)** the first inversion; and **(c)** the second inversion. The colorbar for **(a-c)** is given next to **(a)**. Also shown are **(d)** the initial isotropic damage field and **(e)** the smooth enhancement factor field.

Table 4-1. Damage parameters used in the Larsen C experiments

Parameter	Value
r	0.43
k	4
$D_{\max}$	0.99
D_{cr}	0.5
$\overline{D}_{\mathrm{cr}}$	0.8

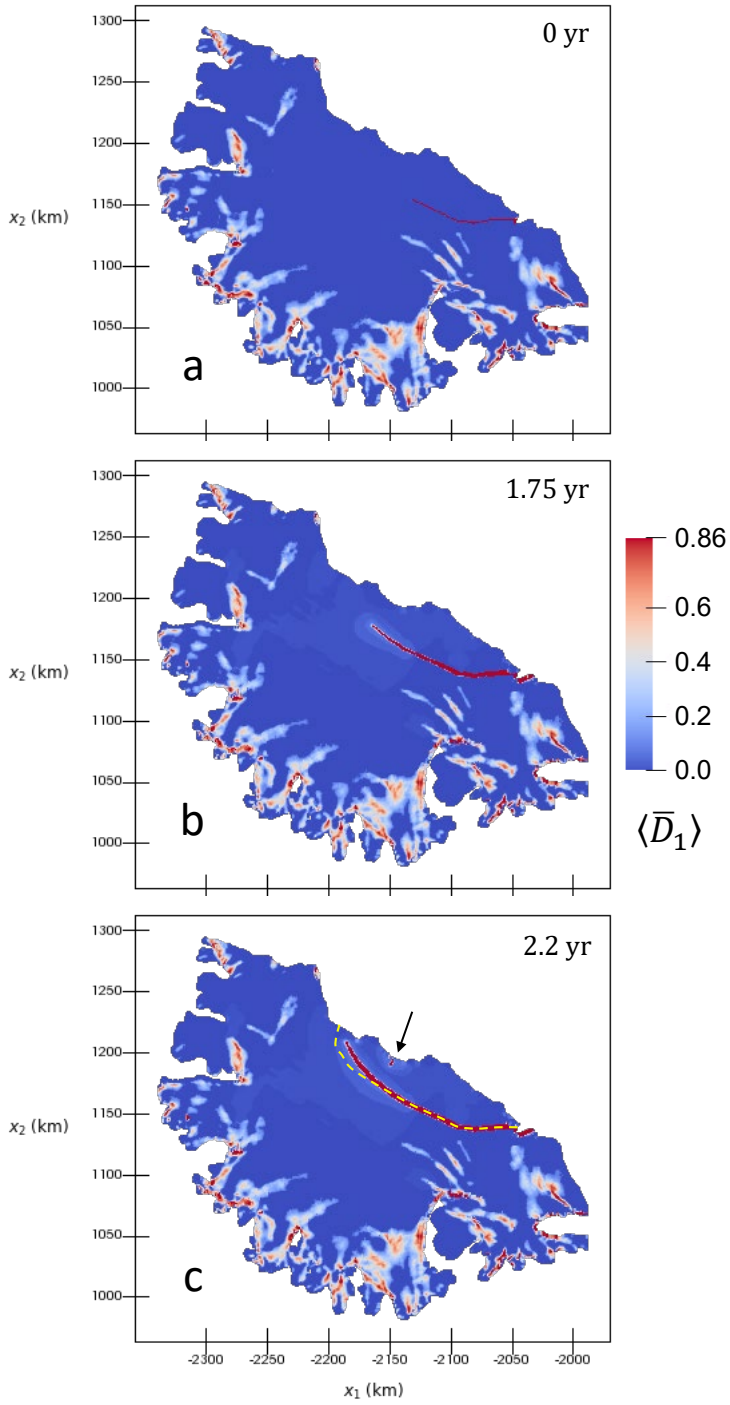

Figure 4-3. Tuning of the Hayhurst parameters: given values

Evolution of the depth-averaged maximum principal damage field, $\langle \overline{D}_1 \rangle$, at **(a)** 0 years, **(b)** 1.75 years, and **(c)** 2.2 years, when using the Hayhurst weighting suggested by Pralong and Funk (2005): α =0.21, β =0.63, λ = 0.16. The yellow dashed line in **(c)** indicates the observed rift path.

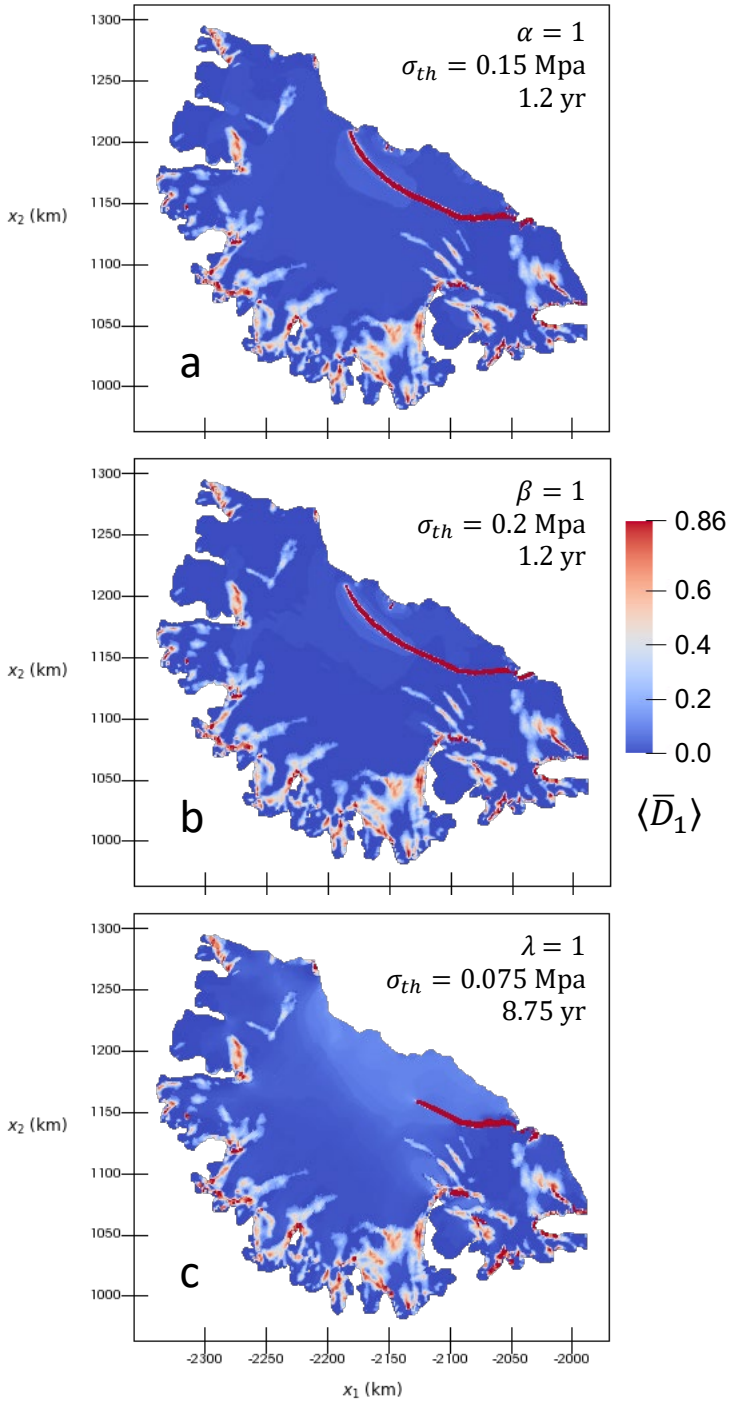

Figure 4-4. Tuning of the Hayhurst parameters: extreme cases

Depth-averaged maximum principal damage, $\langle \overline{D}_1 \rangle$, for the following weightings of the Hayhurst parameters: **(a)** $\alpha = 1$, $\beta = 0$, $\lambda = 0$, **(b)** $\alpha = 0$, $\beta = 1$, $\lambda = 0$, and **(c)** $\alpha = 0$, $\beta = 0$, $\lambda = 1$.

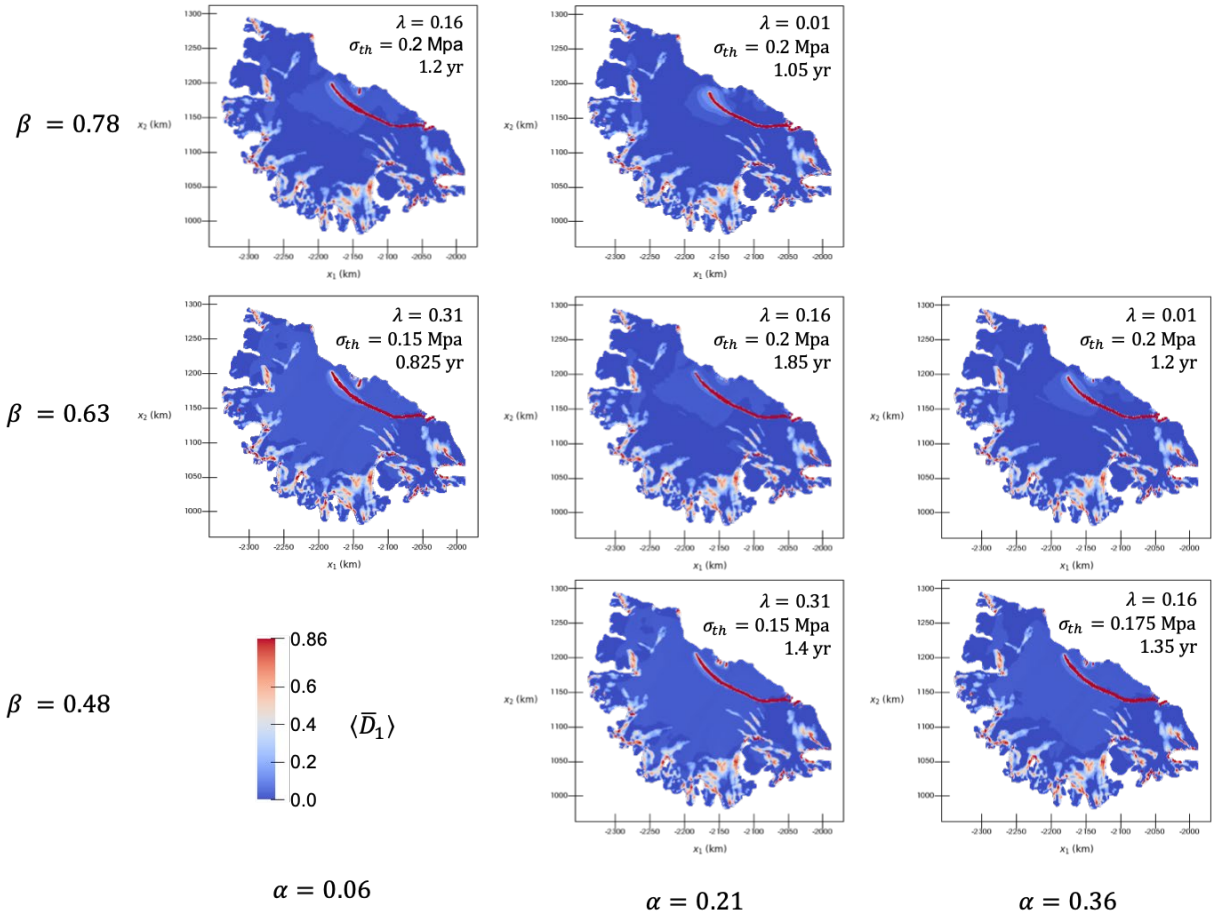

Figure 4-5. Tuning of the Hayhurst parameters: parameter sweep

Depth-averaged maximum principal damage, $\langle \bar{D}_1 \rangle$, for all combination of Hayhurst criterion weightings where one parameter is held at its suggested value from Pralong and Funk (2005), and the other two parameters are varied ±0.15.

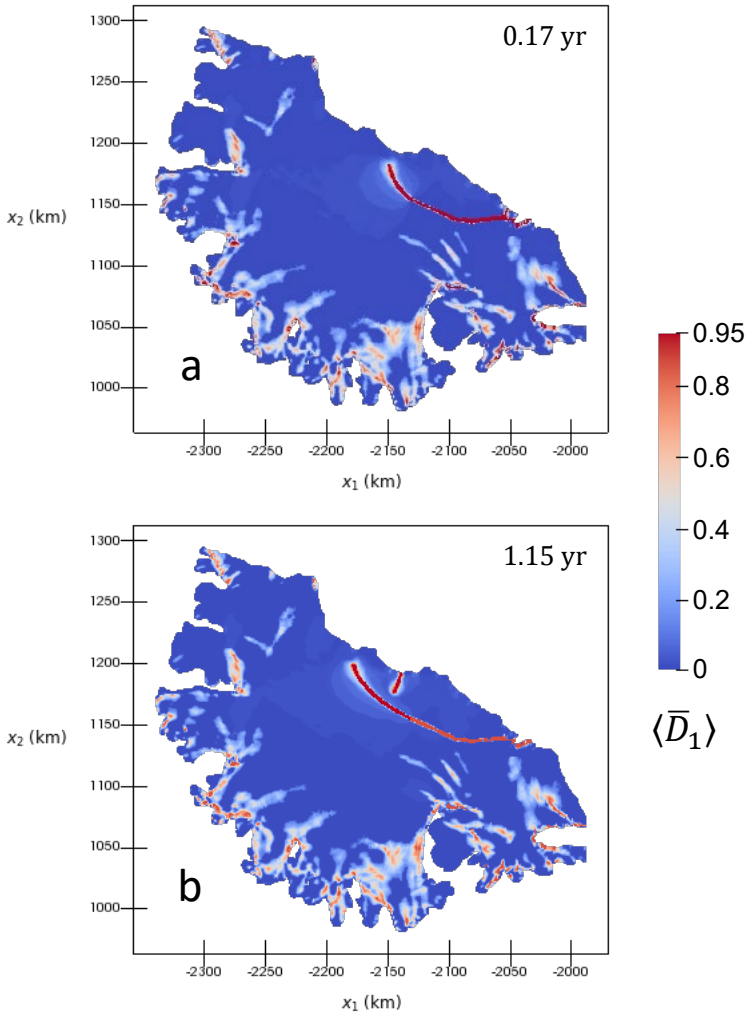

Figure 4-6. Varying maximum 2-D damage

Depth-averaged maximum principal damage, $\langle \overline{D}_1 \rangle$, when setting $\overline{D}_{\max} = 0.95$, rather than $\overline{D}_{\max} = 0.86$. In **(a)** this greater value of $\overline{D}_{\max}$ is enforced everywhere, while in **(b)**, the lesser value of $\overline{D}_{\max}$ is still enforced for the portion of the rift initialized the start of the simulation, and therefore allows less rotation of the nascent iceberg.

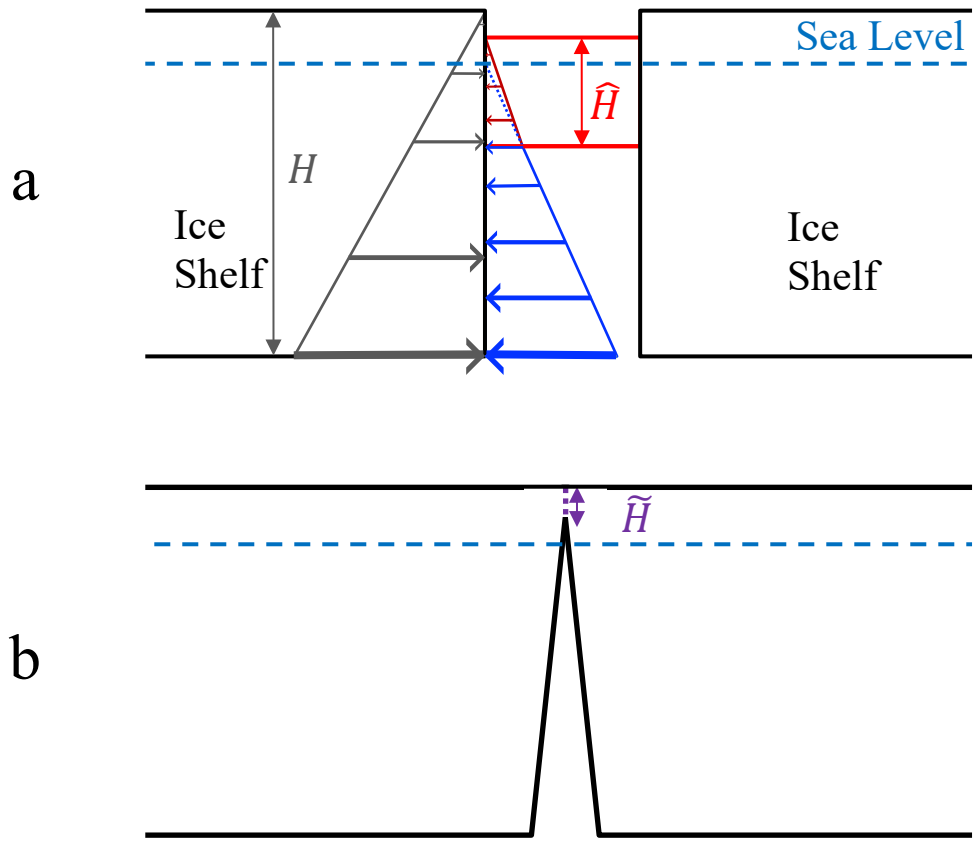

Figure 4-7. Rift boundary scheme

Cross sections of an ice shelf rift. Sea level is marked with the blue dotted line, and the rift flanks have thickness, H. **(a)** The rift is filled with ice mélange (red) of thickness $\widehat{H}$ (reproduced from Larour et al., 2014). Pressure is indicated by the arrows (gray: lithostatic ice pressure; blue: water pressure; red: mélange pressure). **(b)** The rift flanks are in contact near the ice surface over a thickness, $\widetilde{H}$, where the fracture along which contact occurs in indicated by the dotted purple line. This contact induces a similar backpressure on the flank walls as $\widehat{H}$ (not shown). Here, we assume contact only occurs above sea level.

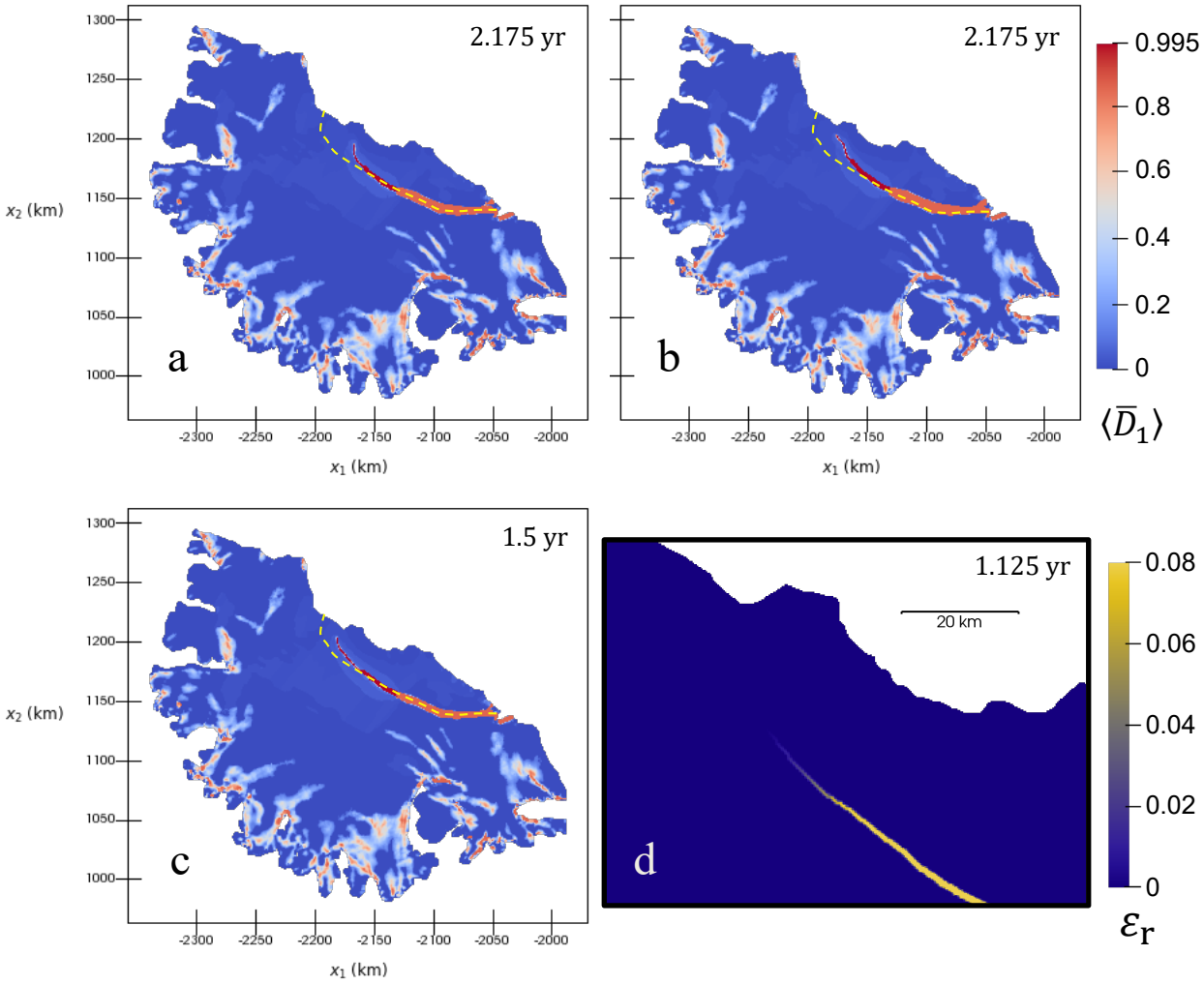

Figure 4-8. Application of the rift boundary scheme

The depth-averaged maximum principal damage, $\langle \bar{D}_1 \rangle$, near calving when using the rift boundary scheme, where **(a)** neither mélange pressure nor pressure from partial contact between rift flanks is applied; **(b)**, mélange is applied, but not partial contact; **(c)** partial contact is applied near the rift tip, but not mélange. **(a-c)** use the same colormap, given in the upper right. The yellow dashed lines indicate the observed rift path. In **(b)**, the mélange fill linearly increases as the rift opens, where no mélange is applied where $\varepsilon_r = 0$ and 10% mélange fill is applied where $\varepsilon_r \geq 0.08$. In **(c)**, contact linearly decreases as the rift opens, where the rift flanks are in contact above sea level where $\varepsilon_r = 0$, and the flanks are fully separated where $\varepsilon_r \geq 0.08$. In **(d)**, detail of ε_r is plotted for the partial contact case at 1.125 years. The colormap for ε_r is truncated at a maximum value of $\varepsilon_r^{\max} = 0.08$.

REFERENCES

Albrecht, T., & Levermann, A. (2014). Fracture-induced softening for large-scale ice dynamics. *Cryosphere, 8*(2), 587-605. doi:10.5194/tc-8-587-2014

Albrecht, T., Martin, M., Haseloff, M., Winkelmann, R., & Levermann, A. (2011). Parameterization for subgrid-scale motion of ice-shelf calving fronts. *Cryosphere, 5*(1), 35-44. doi:10.5194/tc-5-35-2011

Alley, R. B., Horgan, H. J., Joughin, I., Cuffey, K. M., Dupont, T. K., Parizek, B. R., . . . Bassis, J. (2008). A Simple Law for Ice-Shelf Calving. *Science, 322*(5906), 1344-1344. doi:10.1126/science.1162543

Asay-Davis, X. S., Cornford, S. L., Durand, G., Galton-Fenzi, B. K., Gladstone, R. M., Gudmundsson, G. H., . . . Seroussi, H. (2016). Experimental design for three interrelated marine ice sheet and ocean model intercomparison projects: MISMIP v. 3 (MISMIP+), ISOMIP v. 2 (ISOMIP+) and MISOMIP v. 1 (MISOMIP1). *Geoscientific Model Development, 9*(7), 2471-2497. doi:10.5194/gmd-9-2471-2016

Bardenhagen, S. G., & Kober, E. M. (2004). The generalized interpolation material point method. *Cmes-Computer Modeling in Engineering & Sciences, 5*(6), 477-495. doi:10.3970/cmes.2004.005.477

Bassis, J. N., Coleman, R., Fricker, H. A., & Minster, J. B. (2005). Episodic propagation of a rift on the Amery Ice Shelf, East Antarctica. *Geophysical Research Letters, 32*(6). doi:10.1029/2004gl022048

Bassis, J. N., Fricker, H. A., Coleman, R., Bock, Y., Behrens, J., Darnell, D., . . . Minster, J.-B. (2007). Seismicity and deformation associated with ice-shelf rift propagation. *Journal of Glaciology, 53*(183), 523-536. doi:10.3189/002214307784409207

Bassis, J. N., Fricker, H. A., Coleman, R., & Minster, J.-B. (2008). An investigation into the forces that drive ice-shelf rift propagation on the Amery Ice Shelf, East Antarctica. *Journal of Glaciology, 54*(184), 17-27. doi:10.3189/002214308784409116

Bassis, J. N., & Ma, Y. (2015). Evolution of basal crevasses links ice shelf stability to ocean forcing. *Earth and Planetary Science Letters, 409*, 203-211. doi:10.1016/j.epsl.2014.11.003

Bassis, J. N., & Walker, C. (2012). Upper and lower limits on the stability of calving glaciers from the yield strength envelope of ice. *Proceedings of the Royal Society A: Mathematical, Physical and Engineering Sciences, 468*(2140), 913-931. doi:10.1098/rspa.2011.0422

Bazant, Z. P. (1986). Mechanics of distributed cracking. *Appl. Mech. Rev, 39*(5), 675-705. doi:10.1115/1.3143724

Benn, D. I., Warren, C. R., & Mottram, R. H. (2007). Calving processes and the dynamics of calving glaciers. *Earth-Science Reviews, 82*(3), 143-179. doi:10.1016/j.earscirev.2007.02.002

Beuth, L., Wieckowski, Z., & Vermeer, P. A. (2011). Solution of quasi-static large-strain problems by the material point method. *International Journal for Numerical and Analytical Methods in Geomechanics, 35*(13), 1451-1465. doi:10.1002/nag.965

Bing, Y., Cortis, M., Charlton, T. J., Coombs, W. M., & Augarde, C. E. (2019). B-spline based boundary conditions in the material point method. *Computers & Structures, 212*, 257-274. doi:10.1016/j.compstruc.2018.11.003

Bondzio, J. H., Seroussi, H., Morlighem, M., Kleiner, T., Rückamp, M., Humbert, A., & Larour, E. Y. (2016). Modelling calving front dynamics using a level-set method: application to Jakobshavn Isbræ, West Greenland. *The Cryosphere, 10*(2), 497-510. doi:10.5194/tc-10-497-2016

Borstad, C., Khazendar, A., Scheuchl, B., Morlighem, M., Larour, E., & Rignot, E. (2016). A constitutive framework for predicting weakening and reduced buttressing of ice shelves based on observations of the progressive deterioration of the remnant Larsen B Ice Shelf. *Geophysical Research Letters, 43*(5), 2027-2035. doi:10.1002/2015gl067365

Borstad, C., McGrath, D., & Pope, A. (2017). Fracture propagation and stability of ice shelves governed by ice shelf heterogeneity. *Geophysical Research Letters, 44*(9), 4186-4194. doi:10.1002/2017gl072648

Borstad, C. P., Rignot, E., Mouginot, J., & Schodlok, M. P. (2013). Creep deformation and buttressing capacity of damaged ice shelves: theory and application to Larsen C ice shelf. *Cryosphere, 7*(6), 1931-1947. doi:10.5194/tc-7-1931-2013

Brackbill, J. U., Kothe, D. B., & Ruppel, H. M. (1988). Flip: A low-dissipation, particle-in-cell method for fluid flow. *Computer Physics Communications, 48*(1), 25-38. doi:10.1016/0010-4655(88)90020-3

Budd, W. F., & Warner, R. C. (1996). A computer scheme for rapid calculations of balance-flux distributions. *Annals of glaciology, 23*, 21-27. doi:10.3189/S0260305500013215

Bueler, E., & Brown, J. (2009). Shallow shelf approximation as a "sliding law" in a thermomechanically coupled ice sheet model. *Journal of Geophysical Research: Earth Surface, 114*(F3). doi:10.1029/2008jf001179

Castelnau, O., Duval, P., Lebensohn, R. A., & Canova, G. R. (1996). Viscoplastic modeling of texture development in polycrystalline ice with a self-consistent approach: Comparison with bound estimates. *Journal of Geophysical Research: Solid Earth, 101*(B6), 13851-13868. doi:10.1029/96JB00412

Charlton, T. J., Coombs, W. M., & Augarde, C. E. (2017). iGIMP: An implicit generalised interpolation material point method for large deformations. *Computers & Structures, 190*, 108-125. doi:10.1016/j.compstruc.2017.05.004

Clerc, F., Minchew, B. M., & Behn, M. D. (2019). Marine Ice Cliff Instability Mitigated by Slow Removal of Ice Shelves. *Geophysical Research Letters, 46*(21), 12108-12116. doi:10.1029/2019gl084183

Cook, A. J., Holland, P. R., Meredith, M. P., Murray, T., Luckman, A., & Vaughan, D. G. (2016). Ocean forcing of glacier retreat in the western Antarctic Peninsula. *Science, 353*(6296), 283-286. doi:10.1126/science.aae0017

Coombs, W. M., Augarde, C. E., Brennan, A. J., Brown, M. J., Charlton, T. J., Knappett, J. A., . . . Wang, L. (2020). On Lagrangian mechanics and the implicit material point method for large deformation elasto-plasticity. *Computer Methods in Applied Mechanics and Engineering, 358*, 112622. doi:https://doi.org/10.1016/j.cma.2019.112622

Cougnon, E. A., Galton-Fenzi, B. K., Rintoul, S. R., Legrésy, B., Williams, G. D., Fraser, A. D., & Hunter, J. R. (2017). Regional Changes in Icescape Impact Shelf Circulation and Basal Melting. *Geophysical Research Letters, 44*(22), 11,519-511,527. doi:10.1002/2017gl074943

Cuffey, K. M., & Paterson, W. S. B. (2010). *The Physics of Glaciers*: Elsevier Science.

De Rydt, J., Gudmundsson, G. H., Nagler, T., Wuite, J., & King, E. C. (2018). Recent rift formation and impact on the structural integrity of the Brunt Ice Shelf, East Antarctica. *Cryosphere, 12*(2), 505-520. doi:10.5194/tc-12-505-2018

DeConto, R. M., & Pollard, D. (2016). Contribution of Antarctica to past and future sea-level rise. *Nature, 531*(7596), 591-597. doi:10.1038/nature17145

Depoorter, M. A., Bamber, J. L., Griggs, J. A., Lenaerts, J. T. M., Ligtenberg, S. R. M., van den Broeke, M. R., & Moholdt, G. (2013). Calving fluxes and basal melt rates of Antarctic ice shelves. *Nature, 502*(7469), 89-+. doi:10.1038/nature12567

Duddu, R., Bassis, J. N., & Waisman, H. (2013). A numerical investigation of surface crevasse propagation in glaciers using nonlocal continuum damage mechanics. *Geophysical Research Letters, 40*(12), 3064-3068. doi:10.1002/grl.50602

Duddu, R., Jiménez, S., & Bassis, J. (2020). A non-local continuum poro-damage mechanics model for hydrofracturing of surface crevasses in grounded glaciers. *Journal of Glaciology*, 1-15. doi:10.1017/jog.2020.16

Duddu, R., & Waisman, H. (2012). A temperature dependent creep damage model for polycrystalline ice. *Mechanics of Materials, 46*, 23-41. doi:10.1016/j.mechmat.2011.11.007

Duddu, R., & Waisman, H. (2013). A nonlocal continuum damage mechanics approach to simulation of creep fracture in ice sheets. *Computational Mechanics, 51*(6), 961-974. doi:10.1007/s00466-012-0778-7

Dunatunga, S., & Kamrin, K. (2015). Continuum modelling and simulation of granular flows through their many phases. *Journal of Fluid Mechanics, 779*, 483-513. doi:10.1017/jfm.2015.383

Dupont, T. K., & Alley, R. B. (2005). Assessment of the importance of ice-shelf buttressing to ice-sheet flow. *Geophysical Research Letters, 32*(4). doi:10.1029/2004gl022024

Dutton, A., Carlson, A. E., Long, A. J., Milne, G. A., Clark, P. U., DeConto, R., . . . Raymo, M. E. (2015). Sea-level rise due to polar ice-sheet mass loss during past warm periods. *Science, 349*(6244), aaa4019. doi:10.1126/science.aaa4019

Evans, M. W., & Harlow, F. H. (1957). *The particle-in-cell method for hydrodynamic calculations* (Tech. Rep. LA-2139 United States NTIS LANL English).

Fretwell, P., Pritchard, H. D., Vaughan, D. G., Bamber, J. L., Barrand, N. E., Bell, R., . . . Zirizzotti, A. (2013). Bedmap2: improved ice bed, surface and thickness datasets for Antarctica. *The Cryosphere, 7*(1), 375-393. doi:10.5194/tc-7-375-2013

Fürst, J. J., Durand, G., Gillet-Chaulet, F., Tavard, L., Rankl, M., Braun, M., & Gagliardini, O. (2016). The safety band of Antarctic ice shelves. *Nature Climate Change, 6*(5), 479. doi:10.1038/nclimate2912

Gagliardini, O., Cohen, D., Råback, P., & Zwinger, T. (2007). Finite-element modeling of subglacial cavities and related friction law. *Journal of Geophysical Research: Earth Surface, 112*(F2). doi:10.1029/2006JF000576

Gagliardini, O., Zwinger, T., Gillet-Chaulet, F., Durand, G., Favier, L., de Fleurian, B., . . . Thies, J. (2013). Capabilities and performance of Elmer/Ice, a new-generation ice sheet model. *Geoscientific Model Development, 6*(4), 1299-1318. doi:10.5194/gmd-6-1299-2013

Ganczarski, A., & Skrzypek, J. (2001). Application of the Modified Murakami's Anisotropic Creep-Damage Model to 3D Rotationally-Symmetric Problem. *Technische Mechanik. Scientific Journal for Fundamentals and Applications of Engineering Mechanics, 21*(4), 251-260.

Gaume, J., Gast, T., Teran, J., van Herwijnen, A., & Jiang, C. (2018). Dynamic anticrack propagation in snow. *Nature Communications, 9*. doi:10.1038/s41467-018-05181-w

Giry, C., Dufour, F., & Mazars, J. (2011). Stress-based nonlocal damage model. *International Journal of Solids and Structures, 48*(25-26), 3431-3443. doi:10.1016/j.ijsolstr.2011.08.012

Glen, J. W. (1955). The creep of polycrystalline ice. *Proceedings of the Royal Society of London Series a-Mathematical and Physical Sciences, 228*(1175), 519-538. doi:10.1098/rspa.1955.0066

González Acosta, J. L., Vardon, P. J., Remmerswaal, G., & Hicks, M. A. (2019). An investigation of stress inaccuracies and proposed solution in the material point method. *Computational Mechanics*. doi:10.1007/s00466-019-01783-3

Gonzalez Acosta, L., Vardon P, and Hicks M. (2017, 19-23 October 2017). *An evaluation of MPM, GIMP and CMPM in geotechnical problems considering large deformations.* Paper presented at the Proceedings of the 15th International Conference of the International Association for Computer Methods and Advances in Geomechanics, Wuhan, China.

Greve, R., & Blatter, H. (2009). *Dynamics of Ice Sheets and Glaciers*: Springer Berlin Heidelberg.

Hall, F. R., & Hayhurst, D. R. (1991). Modeling of grain-size effects in creep crack-growth using a nonlocal continuum damage approach. *Proceedings of the Royal Society-Mathematical and Physical Sciences, 433*(1888), 405-421. doi:10.1098/rspa.1991.0055

Hammerquist, C. C., & Nairn, J. A. (2017). A new method for material point method particle updates that reduces noise and enhances stability. *Computer Methods in Applied Mechanics and Engineering, 318*, 724-738. doi:10.1016/j.cma.2017.01.035

Hansen, P. C. (1992). Analysis of discrete ill-posed problems by means of the L-curve. *Siam Review, 34*(4), 561-580. doi:10.1137/1034115

Haran, T. J., Bohlander, J., Scambos, T., Painter, T., & Fahnestock, M. (2014). *MODIS Mosaic of Antarctica 2008-2009 (MOA2009) Image Map, Version 1*. Boulder, Colorado USA. NSIDC: National Snow and Ice Data Center. doi: 10.7265/N5KP8037

Hayhurst, D. (1972). Creep rupture under multi-axial states of stress. *Journal of the Mechanics and Physics of Solids, 20*(6), 381-382. doi:10.1016/0022-5096(72)90015-4

Hindmarsh, R. C. A. (1999). On the numerical computation of temperature in an ice sheet. *Journal of Glaciology, 45*(151), 568-574. doi:10.3189/s0022143000001441

Hindmarsh, R. C. A., & Le Meur, E. (2001). Dynamical processes involved in the retreat of marine ice sheets. *Journal of Glaciology, 47*(157), 271-282. doi:10.3189/172756501781832269

Hindmarsh, R. C. A., Vieli, G., & Parrenin, F. (2009). A large-scale numerical model for computing isochrone geometry. *Annals of glaciology, 50*(51), 130-140. doi:10.3189/172756409789097450

Hogg, A. E., & Gudmundsson, G. H. (2017). COMMENTARY: Impacts of the Larsen-C Ice Shelf calving event. *Nature Climate Change, 7*(8), 540-542. doi:10.1038/nclimate3359

Hulbe, C. L., LeDoux, C., & Cruikshank, K. (2010). Propagation of long fractures in the Ronne Ice Shelf, Antarctica, investigated using a numerical model of fracture propagation. *Journal of Glaciology, 56*(197), 459-472. doi:10.3189/002214310792447743

Hutter, K. (1983). *Theoretical Glaciology: Material Science of Ice and the Mechanics of Glaciers and Ice Sheets*: Springer.

IPCC. (2014). Sea Level Change. In *Climate Change 2013 – The Physical Science Basis: Working Group I Contribution to the Fifth Assessment Report of the Intergovernmental Panel on Climate Change* (pp. 1137-1216). Cambridge: Cambridge University Press.

IPCC. (2019). Sea Level Rise and Implications for Low-Lying Islands, Coasts and Communities. In *IPCC Special Report on the Ocean and Cryosphere in a Changing Climate* (pp. 321-445): In Press.

Jeong, S., Howat, I. M., & Bassis, J. N. (2016). Accelerated ice shelf rifting and retreat at Pine Island Glacier, West Antarctica. *Geophysical Research Letters, 43*(22), 11,720-711,725. doi:10.1002/2016gl071360

Jiménez, S., Duddu, R., & Bassis, J. (2017). An updated-Lagrangian damage mechanics formulation for modeling the creeping flow and fracture of ice sheets. *Computer Methods in Applied Mechanics and Engineering, 313*, 406-432. doi:https://doi.org/10.1016/j.cma.2016.09.034

Joughin, I., & MacAyeal, D. R. (2005). Calving of large tabular icebergs from ice shelf rift systems. *Geophysical Research Letters, 32*(2). doi:10.1029/2004gl020978

Joughin, I., Smith, B. E., & Medley, B. (2014). Marine ice sheet collapse potentially under way for the Thwaites Glacier Basin, West Antarctica. *Science, 344*(6185), 735-738.

Jouvet, G., Picasso, M., Rappaz, J., & Blatter, H. (2008). A new algorithm to simulate the dynamics of a glacier: theory and applications. *Journal of Glaciology, 54*(188), 801-811. doi:10.3189/002214308787780049

Keller, A., & Hutter, K. (2014). Conceptual thoughts on continuum damage mechanics for shallow ice shelves. *Journal of Glaciology, 60*(222), 685-693. doi:10.3189/2014JoG14J010

Larour, E., Khazendar, A., Borstad, C., Seroussi, H., Morlighem, M., & Rignot, E. (2014). Representation of sharp rifts and faults mechanics in modeling ice shelf flow dynamics: Application to Brunt/Stancomb-Wills Ice Shelf, Antarctica. *Journal of Geophysical Research: Earth Surface, 119*(9), 1918-1935. doi:10.1002/2014JF003157

Larour, E., Rignot, E., & Aubry, D. (2004). Processes involved in the propagation of rifts near Hemmen ice rise, Ronne ice shelf, Antarctica. *Journal of Glaciology, 50*(170), 329-341. doi:10.3189/172756504781829837

Larour, E., Rignot, E., & Aubry, D. (2004). Processes involved in the propagation of rifts near Hemmen Ice Rise, Ronne Ice Shelf, Antarctica. *Journal of Glaciology, 50*(170), 329-341. doi:10.3189/172756504781829837

Larour, E., Rignot, E., Joughin, I., & Aubry, D. (2005). Rheology of the Ronne Ice Shelf, Antarctica, inferred from satellite radar interferometry data using an inverse control method. *Geophysical Research Letters, 32*(5).

Le Brocq, A. M., Payne, A. J., & Siegert, M. J. (2006). West Antarctic balance calculations: Impact of flux-routing algorithm, smoothing algorithm and topography. *Computers & Geosciences, 32*(10), 1780-1795. doi:10.1016/j.cageo.2006.05.003

Leguy, G. R., Asay-Davis, X. S., & Lipscomb, W. H. (2014). Parameterization of basal friction near grounding lines in a one-dimensional ice sheet model. *The Cryosphere, 8*(4), 1239-1259. doi:10.5194/tc-8-1239-2014

Lemaitre, J. (1971). *Evaluation of dissipation and damage in metals.* Paper presented at the Proc. ICM Kyoto.

Lemaitre, J. (2012). *A course on damage mechanics*: Springer Science & Business Media.

Lemaitre, J., & Chaboche, J. L. (1978). Phenomenological approach of damage rupture. *Journal De Mecanique Appliquee, 2*(3), 317-365.

Levermann, A., Albrecht, T., Winkelmann, R., Martin, M. A., Haseloff, M., & Joughin, I. (2012). Kinematic first-order calving law implies potential for abrupt ice-shelf retreat. *The Cryosphere, 6*, 273. doi:10.5194/tc-6-273-2012

Ling, X., Tu, S. T., & Gong, J. M. (2000). Application of Runge-Kutta-Merson algorithm for creep damage analysis. *International Journal of Pressure Vessels and Piping, 77*(5), 243-248. doi:10.1016/s0308-0161(00)00010-7

Lipovsky, B. P. (2020). Ice shelf rift propagation: stability, three-dimensional effects, and the role of marginal weakening. *The Cryosphere, 14*(5), 1673-1683. doi:10.5194/tc-14-1673-2020

Lipscomb, W. H., Price, S. F., Hoffman, M. J., Leguy, G. R., Bennett, A. R., Bradley, S. L., . . . Worley, P. H. (2019). Description and evaluation of the Community Ice Sheet Model (CISM) v2.1. *Geoscientific Model Development, 12*(1), 387-424. doi:10.5194/gmd-12-387-2019

Liu, Y., Moore, J. C., Cheng, X., Gladstone, R. M., Bassis, J. N., Liu, H., . . . Hui, F. (2015). Ocean-driven thinning enhances iceberg calving and retreat of Antarctic ice shelves. *Proceedings of the National Academy of Sciences, 112*(11), 3263-3268. doi:10.1073/pnas.1415137112

Logan, L., Catania, G., Lavier, L., & Choi, E. (2013). A novel method for predicting fracture in floating ice. *Journal of Glaciology, 59*(216), 750-758. doi:10.3189/2013JoG12J210

Londono, Juan G., Berger-Vergiat, L., & Waisman, H. (2017). An equivalent stress-gradient regularization model for coupled damage-viscoelasticity. *Computer Methods in Applied Mechanics and Engineering, 322*, 137-166. doi:10.1016/j.cma.2017.04.010

Luckman, A., Jansen, D., Kulessa, B., King, E., Sammonds, P., & Benn, D. (2012). Basal crevasses in Larsen C Ice Shelf and implications for their global abundance. *The Cryosphere, 6*(1), 113-123. doi:10.5194/tc-6-113-2012

Ma, S., Zhang, X., Lian, Y., & Zhou, X. (2009). Simulation of high explosive explosion using adaptive material point method. *Computer Modeling in Engineering & Sciences, 39*(2), 101-124. doi:doi:10.3970/cmes.2009.039.101

Ma, Y., Gagliardini, O., Ritz, C., Gillet-Chaulet, F., Durand, G., & Montagnat, M. (2010). Enhancement factors for grounded ice and ice shelves inferred from an anisotropic ice-flow model. *Journal of Glaciology, 56*(199), 805-812. doi:10.3189/002214310794457209

Macayeal, D. R. (1989). Large-scale ice flow over a viscous basal sediment - Theory and application to Ice Stream-B, Antarctica. *Journal of Geophysical Research-Solid Earth and Planets, 94*(B4), 4071-4087. doi:10.1029/JB094iB04p04071

MacGregor, J. A., Catania, G. A., Markowski, M. S., & Andrews, A. G. (2012). Widespread rifting and retreat of ice-shelf margins in the eastern Amundsen Sea Embayment between 1972 and 2011. *Journal of Glaciology, 58*(209), 458-466. doi:10.3189/2012JoG11J262

Maule, C. F., Purucker, M. E., Olsen, N., & Mosegaard, K. (2005). Heat flux anomalies in Antarctica revealed by satellite magnetic data. *Science, 309*(5733), 464-467. doi:10.1126/science.1106888

McGrath, D., Steffen, K., Scambos, T., Rajaram, H., Casassa, G., & Lagos, J. L. R. (2012). Basal crevasses and associated surface crevassing on the Larsen C ice shelf, Antarctica, and their role in ice-shelf instability. *Annals of glaciology, 53*(60), 10-18. doi:10.3189/2012AoG60A005

Mobasher, M. E., Duddu, R., Bassis, J. N., & Waisman, H. (2016). Modeling hydraulic fracture of glaciers using continuum damage mechanics. *Journal of Glaciology, 62*(234), 794-804. doi:10.1017/jog.2016.68

Morland, L. W. (1987). *Unconfined Ice-Shelf Flow.* Paper presented at A Workshop on the Dynamics of the West Antarctic Ice Sheet, Dordrecht.

Morland, L. W., & Zainuddin, R. (1987). *Plane and Radial Ice-Shelf Flow with Prescribed Temperature Profile.* Paper presented at A Workshop on the Dynamics of the West Antarctic Ice Sheet, Dordrecht.

Morlighem, M., Bondzio, J., Seroussi, H., Rignot, E., Larour, E., Humbert, A., & Rebuffi, S. (2016). Modeling of Store Gletscher's calving dynamics, West Greenland, in response to ocean thermal forcing. *Geophysical Research Letters, 43*(6), 2659-2666. doi:10.1002/2016gl067695

Morlighem, M., Wood, M., Seroussi, H., Choi, Y., & Rignot, E. (2019). Modeling the response of northwest Greenland to enhanced ocean thermal forcing and subglacial discharge. *The Cryosphere, 13*(2), 723-734. doi:10.5194/tc-13-723-2019

Murakami, S., Ohno, N. (1980). *A continuum theory of creep and creep damage*. Paper presented at the 3rd Symposium Creep in Structures. International Union of Theoretical and Applied Mechanics, Leicaster, UK.

Murakami, S. (1983). Notion of Continuum Damage Mechanics and its Application to Anisotropic Creep Damage Theory. *Journal of Engineering Materials and Technology, 105*(2), 99-105. doi:10.1115/1.3225633

Murakami, S., Kawai, M., & Rong, H. (1988). Finite element analysis of creep crack growth by a local approach. *International Journal of Mechanical Sciences, 30*(7), 491-502. doi:10.1016/0020-7403(88)90003-3

Nairn, J. A. (2003). Material point method calculations with explicit cracks. *Computer Modeling in Engineering and Sciences, 4*(6), 649-664.

Nairn, J. A., Hammerquist, C. C., & Aimene, Y. E. (2017). Numerical implementation of anisotropic damage mechanics. *International Journal for Numerical Methods in Engineering, 112*(12), 1848-1868. doi:10.1002/nme.5585

Nick, F. M., Van Der Veen, C. J., Vieli, A., & Benn, D. I. (2010). A physically based calving model applied to marine outlet glaciers and implications for the glacier dynamics. *Journal of Glaciology, 56*(199), 781-794. doi:10.3189/002214310794457344

Nick, F. M., Vieli, A., Andersen, M. L., Joughin, I., Payne, A., Edwards, T. L., . . . van de Wal, R. S. W. (2013). Future sea-level rise from Greenland's main outlet glaciers in a warming climate. *Nature, 497*(7448), 235-238. doi:10.1038/nature12068

Nye, J. F., & Perutz, M. F. (1957). The distribution of stress and velocity in glaciers and ice-sheets. *Proceedings of the Royal Society of London. Series A. Mathematical and Physical Sciences, 239*(1216), 113-133. doi:10.1098/rspa.1957.0026

Paolo, F. S., Fricker, H. A., & Padman, L. (2015). Volume loss from Antarctic ice shelves is accelerating. *Science, 348*(6232), 327-331. doi:10.1126/science.aaa0940

Pattyn, F. (2010). Antarctic subglacial conditions inferred from a hybrid ice sheet/ice stream model. *Earth and Planetary Science Letters, 295*(3), 451-461. doi:10.1016/j.epsl.2010.04.025

Pattyn, F., & Morlighem, M. (2020). The uncertain future of the Antarctic Ice Sheet. *Science, 367*(6484), 1331-1335. doi:10.1126/science.aaz5487

Pegler, S. S., & Worster, M. G. (2012). Dynamics of a viscous layer flowing radially over an inviscid ocean. *Journal of Fluid Mechanics, 696*, 152-174. doi:10.1017/jfm.2012.21

Pegler, S. S., & Worster, M. G. (2013). An experimental and theoretical study of the dynamics of grounding lines. *Journal of Fluid Mechanics, 728*, 5-28. doi:10.1017/jfm.2013.269

Plate, C., Müller, R., Humbert, A., & Gross, D. (2012). Evaluation of the criticality of cracks in ice shelves using finite element simulations. *The Cryosphere, 6*(5), 973-984. doi:10.5194/tc-6-973-2012

Pollard, D., & DeConto, R. M. (2012). Description of a hybrid ice sheet-shelf model, and application to Antarctica. *Geosci. Model Dev., 5*(5), 1273-1295. doi:10.5194/gmd-5-1273-2012

Pollard, D., DeConto, R. M., & Alley, R. B. (2015). Potential Antarctic Ice Sheet retreat driven by hydrofracturing and ice cliff failure. *Earth and Planetary Science Letters, 412*, 112-121. doi:10.1016/j.epsl.2014.12.035

Pope, A. (2016). allenpope/Landsat8_Velocity_LarsenC: Processing Landsat 8 Velocities for Larsen C [Data Set]. Zenodo, [Available at http://doi.org/10.5281/zenodo.185651.]

Pralong, A., & Funk, M. (2005). Dynamic damage model of crevasse opening and application to glacier calving. *Journal of Geophysical Research: Solid Earth, 110*(B1). doi:10.1029/2004jb003104

Pralong, A., Hutter, K., & Funk, M. (2006). Anisotropic damage mechanics for viscoelastic ice. *Continuum Mechanics and Thermodynamics, 17*(5), 387-408. doi:10.1007/s00161-005-0002-5

Pritchard, H. D., Ligtenberg, S. R. M., Fricker, H. A., Vaughan, D. G., van den Broeke, M. R., & Padman, L. (2012). Antarctic ice-sheet loss driven by basal melting of ice shelves. *Nature, 484*(7395), 502-505. doi:10.1038/nature10968

Qi, W. D., & Bertram, A. (1999). Anisotropic continuum damage modeling for single crystals at high temperatures. *International Journal of Plasticity, 15*(11), 1197-1215. doi:10.1016/s0749-6419(99)00035-2

Rignot, E., Jacobs, S., Mouginot, J., & Scheuchl, B. (2013). Ice-Shelf Melting Around Antarctica. *Science, 341*(6143), 266-270. doi:10.1126/science.1235798

Rignot, E., & MacAyeal, D. R. (1998). Ice-shelf dynamics near the front of the Filchner—Ronne Ice Shelf, Antarctica, revealed by SAR interferometry. *Journal of Glaciology, 44*(147), 405-418. doi:10.3189/S0022143000002732

Rignot, E., Mouginot, J., Morlighem, M., Seroussi, H., & Scheuchl, B. (2014). Widespread, rapid grounding line retreat of Pine Island, Thwaites, Smith, and Kohler glaciers, West Antarctica, from 1992 to 2011. *Geophysical Research Letters, 41*(10), 3502-3509.

Rignot, E., Mouginot, J., & Scheuchl, B. (2017). *MEaSUREs InSAR-Based Antarctica Ice Velocity Map, Version 2*. Boulder, Colorado USA. NASA National Snow and Ice Data Center Distributed Active Archive Center. doi: 10.5067/D7GK8F5J8M8R

Rist, M. A., Sammonds, P. R., Murrell, S. A. F., Meredith, P. G., Doake, C. S. M., Oerter, H., & Matsuki, K. (1999). Experimental and theoretical fracture mechanics applied to Antarctic ice fracture and surface crevassing. *Journal of Geophysical Research: Solid Earth, 104*(B2), 2973-2987. doi:10.1029/1998jb900026

Robinson, N. J., Williams, M. J. M., Barrett, P. J., & Pyne, A. R. (2010). Observations of flow and ice-ocean interaction beneath the McMurdo Ice Shelf, Antarctica. *Journal of Geophysical Research: Oceans, 115*(C3). doi:10.1029/2008jc005255

Sadeghirad, A., Brannon, R. M., & Burghardt, J. (2011). A convected particle domain interpolation technique to extend applicability of the material point method for problems involving massive deformations. *International Journal for Numerical Methods in Engineering, 86*(12), 1435-1456. doi:10.1002/nme.3110

Sadeghirad, A., Brannon, R. M., & Guilkey, J. E. (2013). Second-order convected particle domain interpolation (CPDI2) with enrichment for weak discontinuities at material interfaces. *International Journal for Numerical Methods in Engineering, 95*(11), 928-952. doi:10.1002/nme.4526

Scambos, T. A., Bohlander, J. A., Shuman, C. A., & Skvarca, P. (2004). Glacier acceleration and thinning after ice shelf collapse in the Larsen B embayment, Antarctica. *Geophysical Research Letters, 31*(18). doi:10.1029/2004gl020670

Scherer, R. P., Aldahan, A., Tulaczyk, S., Possnert, G., Engelhardt, H., & Kamb, B. (1998). Pleistocene Collapse of the West Antarctic Ice Sheet. *Science, 281*(5373), 82-85. doi:10.1126/science.281.5373.82

Schoof, C. (2005). The effect of cavitation on glacier sliding. *Proceedings of the Royal Society A: Mathematical, Physical and Engineering Sciences, 461*(2055), 609-627. doi:10.1098/rspa.2004.1350

Schoof, C. (2007). Ice sheet grounding line dynamics: Steady states, stability, and hysteresis. *Journal of Geophysical Research: Earth Surface, 112*(F3).

Seroussi, H., Morlighem, M., Larour, E., Rignot, E., & Khazendar, A. (2014). Hydrostatic grounding line parameterization in ice sheet models. *Cryosphere, 8*(6), 2075-2087. doi:10.5194/tc-8-2075-2014

Shepherd, A., Wingham, D., Payne, T., & Skvarca, P. (2003). Larsen ice shelf has progressively thinned. *Science, 302*(5646), 856-859. doi:10.1126/science.1089768

Shumskiy, P. A., & Krass, M. S. (1976). Mathematical Models of Ice Shelves. *Journal of Glaciology, 17*(77), 419-432. doi:10.3189/S002214300001371X

Smith, B. E., Gourmelen, N., Huth, A., & Joughin, I. (2017). Connected subglacial lake drainage beneath Thwaites Glacier, West Antarctica. *The Cryosphere, 11*(1), 451-467. doi:10.5194/tc-11-451-2017

Stern, A. A., Adcroft, A., & Sergienko, O. (2016). The effects of Antarctic iceberg calving-size distribution in a global climate model. *Journal of Geophysical Research: Oceans, 121*(8), 5773-5788. doi:10.1002/2016jc011835

Stern, A. A., Johnson, E., Holland, D. M., Wagner, T. J. W., Wadhams, P., Bates, R., . . . Tremblay, J.-E. (2015). Wind-driven upwelling around grounded tabular icebergs. *Journal of Geophysical Research: Oceans, 120*(8), 5820-5835. doi:10.1002/2015jc010805

Stomakhin, A., Schroeder, C., Chai, L., Teran, J., & Selle, A. (2013). A material point method for snow simulation. *Acm Transactions on Graphics, 32*(4). doi:10.1145/2461912.2461948

Sulsky, D., Chen, Z., & Schreyer, H. L. (1994). A particle method for history-dependent materials. *Computer Methods in Applied Mechanics and Engineering, 118*(1-2), 179-196. doi:10.1016/0045-7825(94)00033-6

Sulsky, D., Schreyer, H., Peterson, K., Kwok, R., & Coon, M. (2007). Using the material-point method to model sea ice dynamics. *Journal of Geophysical Research: Oceans, 112*(C2). doi:10.1029/2005jc003329

Sulsky, D., Zhou, S.-J., & Schreyer, H. L. (1995). Application of a particle-in-cell method to solid mechanics. *Computer Physics Communications, 87*(1), 236-252. doi:10.1016/0010-4655(94)00170-7

Sun, S., Cornford, S. L., Moore, J. C., Gladstone, R., & Zhao, L. (2017). Ice shelf fracture parameterization in an ice sheet model. *The Cryosphere, 11*(6), 2543-2554. doi:10.5194/tc-11-2543-2017

Todd, J., & Christoffersen, P. (2014). Are seasonal calving dynamics forced by buttressing from ice mélange or undercutting by melting? Outcomes from full-Stokes simulations of Store Gletscher, West Greenland. doi:10.5194/tc-8-2353-2014

van der Veen, C. J. (2002). Calving glaciers. *Progress in Physical Geography: Earth and Environment, 26*(1), 96-122. doi:10.1191/0309133302pp327ra

Van der Veen, C. J. (2013). *Fundamentals of glacier dynamics* (2 ed.). Boca Raton, FL: CRC Press.

Van Liefferinge, B., & Pattyn, F. (2013). Using ice-flow models to evaluate potential sites of million year-old ice in Antarctica. *Clim. Past, 9*(5), 2335-2345. doi:10.5194/cp-9-2335-2013

Van Wessem, J. M., Reijmer, C. H., Morlighem, M., Mouginot, J., Rignot, E., Medley, B., . . . Van Meijgaard, E. (2014). Improved representation of East Antarctic surface mass balance in a regional atmospheric climate model. *Journal of Glaciology, 60*(222), 761-770. doi:10.3189/2014JoG14J051

Wang, L., Coombs, W. M., Augarde, C. E., Cortis, M., Charlton, T. J., Brown, M. J., . . . Blake, A. (2019). On the use of domain-based material point methods for problems involving large distortion. *Computer Methods in Applied Mechanics and Engineering, 355*, 1003-1025. doi:10.1016/j.cma.2019.07.011

Wearing, M. G., Kingslake, J., & Worster, M. G. (2020). Can unconfined ice shelves provide buttressing via hoop stresses? *Journal of Glaciology*, 1-13. doi:10.1017/jog.2019.101

Weertman, J. (1957). Deformation of Floating Ice Shelves. *Journal of Glaciology, 3*(21), 38-42. doi:10.3189/S0022143000024710

Weertman, J. (1974). Stability of the junction of an ice sheet and an ice shelf. *Journal of Glaciology, 13*(67), 3-11.

Weertman, J. (1977). Penetration Depth of Closely Spaced Water-free Crevasses. *Journal of Glaciology, 18*(78), 37-46. doi:10.3189/S0022143000021493

Weis, M. (2001). *Theory and Finite Element Analysis of Shallow Ice Shelves.* (PhD). Technische Universität Darmstadt, Retrieved from http://tuprints.ulb.tu-darmstadt.de/171/

Yu, H., Rignot, E., Morlighem, M., & Seroussi, H. (2017). Iceberg calving of Thwaites Glacier, West Antarctica: full-Stokes modeling combined with linear elastic fracture mechanics. *The Cryosphere, 11*(3), 1283. doi:10.5194/tc-11-1283-2017

Yue, Y. H., Smith, B., Batty, C., Zheng, C. X., & Grinspun, E. (2015). Continuum Foam: A Material Point Method for Shear-Dependent Flows. *Acm Transactions on Graphics, 34*(5). doi:10.1145/2751541

Zhang, D. Z., Ma, X., & Giguere, P. T. (2011). Material point method enhanced by modified gradient of shape function. *Journal of Computational Physics, 230*(16), 6379-6398. doi:10.1016/j.jcp.2011.04.032

Zhao, X. Y., Bolognin, M., Liang, D. F., Rohe, A., & Vardon, P. J. (2019). Development of in/outflow boundary conditions for MPM simulation of uniform and non-uniform open channel flows. *Computers & Fluids, 179*, 27-33. doi:10.1016/j.compfluid.2018.10.007

Zolochevsky, A., Sklepus, S., Hyde, T. H., Becker, A. A., & Peravali, S. (2009). Numerical modeling of creep and creep damage in thin plates of arbitrary shape from materials with different behavior in tension and compression under plane stress conditions. *International Journal for Numerical Methods in Engineering, 80*(11), 1406-1436. doi:10.1002/nme.2663

Appendix A. Supplementary materials to Chapter 2

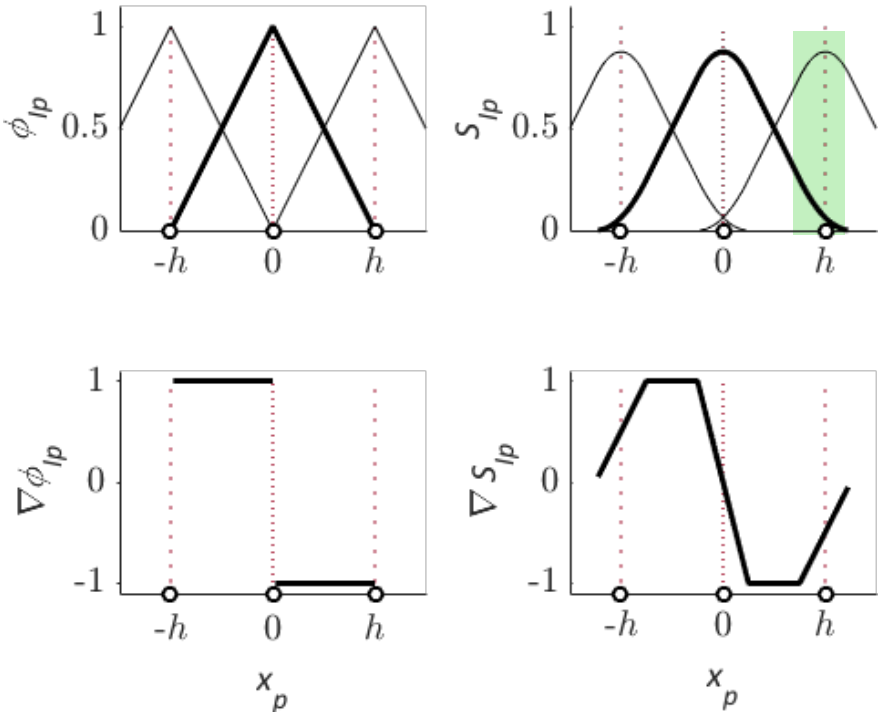

Figure A-1. sMPM and GIMPM shape functions

The 1-D sMPM (left) and GIMPM (right) shape functions for a node positioned at $x_i = 0$ with the length of an element given by *h*. The length of the material point used in the GIMPM convolution is *h*/2 (green shading)

Appendix B. Supplementary materials to Chapter 3

B.1 Supplementary Figures

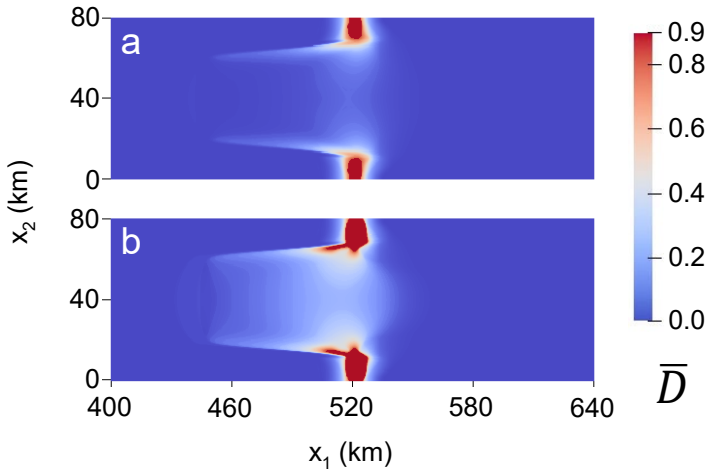

Figure B-1. Initial damage accumulation for isotropic creep damage

Damage field for the isotropic ($\gamma = 0$) creep damage simulation at **(a)** 0.06 years and **(b)** 0.12 years.

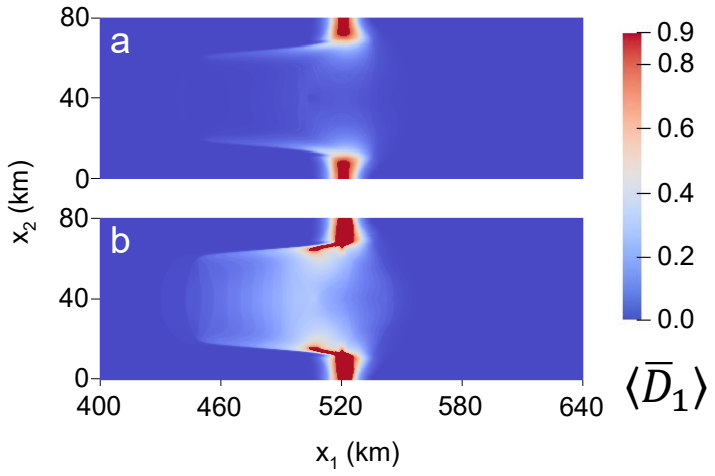

Figure B-2. Initial damage accumulation for mixed isotropic/anisotropic creep damage

Maximum principal damage field for the mixed isotropic/anisotropic ($\gamma = 0.5$) creep damage simulation at **(a)** 0.06 years and **(b)** 0.18 years.

B.2 Description of zero-stress damage model

In the zero-stress criterion, closely-spaced crevasses are assumed to propagate to the depth at which the net longitudinal maximum principal Cauchy stress is zero (Nye, 1957). The net Cauchy stress at depth is parameterized as

$$\sigma_{ij}(z) = \sigma_{ij}^{\mathrm{D}}(z) - p_{\mathrm{eff}}(z)\delta_{ij}, \tag{B.1}$$

where $p_{\mathrm{eff}}(z)$ takes the same form as within the creep damage model from Equations (3.14)-(3.16). We disregard the water pressure term for surface crevasses and assume dry surface conditions. A zero-stress isotropic damage variable was previously defined for SSA models as the ratio of the combined depths of surface and basal crevasses to the ice thickness (Sun et al., 2017), and here, we extend this damage variable to anisotropic form as a 2nd order tensor, $\widehat{\boldsymbol{D}}$. To our knowledge, all other SSA applications of the zero-stress model have solely focused on obtaining plausible estimates of crevasse depths (Pollard et al., 2015; Bassis & Walker, 2012; Bassis & Ma, 2015), rather than also applying the crevasse depths as a damage variable that influences the stress solution. Zero-stress crevasse depths are assumed to be in equilibrium with the stress field, and given the interdependence between damage and stress, the zero-stress damage solution must therefore be computed simultaneously with the SSA solution. This coupled solution is facilitated by assuming deviatoric stresses are depth-invariant, which allows an analytical solution for crevasse depths (Nick et al., 2010). We adopt this assumption for simplicity, as did the previous SSA zero-stress damage study (Sun et al., 2017). However, assuming depth-invariant deviatoric stresses is only justified only if crevasses are closely-spaced so that the stress singularity at crevasse tips is dissipated (Weertman, 1977), and if vertical ice columns are isothermal.

We emphasize that the zero-stress approximation is likely more accurate when applied to outlet glaciers in Greenland (e.g. Nick et al., 2010; Todd & Christofferson, 2014) than when applied to ice shelves, where the assumptions of closely-spaced crevasses in equilibrium with the stress field and crevasse evolution based on only tensile stresses are less valid. Ice shelf basal crevasses tend to be widely-spaced and may experience mixed-mode fracture (McGrath et al., 2012; Luckman et al., 2012). Furthermore, assuming an isothermal ice shelf may not be an accurate approximation, as seawater temperatures at the ice shelf base greatly exceed surface air temperatures. However, a vertically-varying temperature profile would induce vertically-varying deviatoric stresses, so that a more complex iterative scheme would be required here solve the coupled SSA/zero-stress damage problem.

We restrict our zero-stress damage tests to the fully-isotropic and fully-anisotropic cases. For full-anisotropy, the initial damage accumulation for the zero stress model occurs on a single plane aligned normal to the maximum principal stress of the undamaged configuration, as in the creep damage model. This plane subsequently rotates over time according to spin, as in Equation (3.8). However, unlike creep damage, anisotropic zero-stress damage accumulation must be restricted to this plane at subsequent time steps, and evolves according to the stresses normal to the plane because the zero-stress criterion assumes crevasses open in accordance with tensile (Mode I) fracture. Rifting is incorporated with the same 2-D critical damage rupture scheme from the creep damage model. To facilitate comparison between the zero-stress and creep damage models, we adopt the same adaptive time-stepping scheme used for the creep damage simulations, but defining $\overline{\mathrm{dD}}_{\max} = \max\left(\widehat{D}^{m+1} - \widehat{D}^{m}\right)$ and eliminating the condition to restart the damage solution if $\overline{\mathrm{dD}}_{\max} > 0.075$ because damage is solved implicitly.

B.3 Description of damage modification for necking and mass balance

Necking describes the process in which basal crevasses widen under tension and the resulting feedback on crevasse evolution, where depending on strain-rates and crevasse-geometry, the ratio of crevasse penetration to ice thickness (i.e. damage) will either increase or decrease over time (Bassis & Ma, 2015). The ratio can increase due to greater thinning rates associated with the presence of crevasses. However, as crevasses grow, the local ice geometry simultaneously adjusts to hydrostatic equilibrium, and depressions fill with surrounding ice due to "gravitational restoring forces". If the system is dominated by these gravitational forces rather than thinning, the ratio of crevasse penetration to ice thickness will decrease (i.e. healing). The ratio is further modulated by mass balance processes, such as melting and accumulation of snow or marine ice in crevasses. A previous study investigated this complex coupling of various processes, and an expression for large-scale ice flow was proposed using perturbation analysis that defines the rate at which damage is modulated according to necking and mass balance processes (Bassis & Ma, 2015). This model can be employed in conjunction with a mechanical damage model that tracks crevasse depths, but has not yet been tested to our knowledge.

When used in conjunction with the zero-stress model, this large-scale damage modification takes the form:

$$\frac{d\widehat{\boldsymbol{D}}}{dt} = \left(n^*(1 - S_0)\langle\dot{\varepsilon}_1\rangle + \frac{\dot{m}}{H}\right)\widehat{\boldsymbol{D}}\,, \tag{B.2}$$

where the first term in the parentheses describes the influence of necking on damage and the second term describes the influence of the melt rate, $\dot{m}$. Within the necking term, parameter n^* is an effective flow law exponent and S_0 describes the ratio of gravitational restoring force to

tensile stress. Derivation of these terms is non-trivial, and we direct the reader to the original publication for a detailed explanation. The expression is only valid in the long wavelength limit, which corresponds to the following assumptions: crevasses are wide compared to the ice thickness, perturbations are assumed to relax immediately to hydrostatic equilibrium, and the melt rate in crevasses is equivalent to the large scale melt rate. We solve (B.2) immediately after completion of the SSA solution, and add the damage increment to the zero-stress damage calculated during the SSA.